UNIVERSITÀ DI ROMA SAPIENZA

Scuola di Dottorato in Ingegneria Civile ed Architettura

Dottorato di Ricerca in Ingegneria Ambientale e Idraulica
XXX CICLO

MODELING AND INVERSION OF SELF-POTENTIAL FOR HYDROGEOLOGICAL AND ENVIRONMENTAL APPLICATIONS

Candidate:
Ing. Ilaria Oliveti

Thesis advisor:
Prof. E. Cardarelli

Coordinator:
Prof.ssa M.R.Boni

Thesis submitted in October 2017

Abstract

The self-potential method responds to chemical potential gradients of charges carriers creating polarization in the porous media. Of specific interest are the streaming potential due to fluid flow and the "electro-redox" effect associated with redox potential gradients.

To evaluate the self-potential distribution resulting from all these charge polarisation mechanisms and enable the study of variably saturated flow problems of complicated geometry, a two-dimensional finite element algorithm is implemented in Matlab. This forward algorithm explicitly calculates the distribution of electric current sources and solves for the self-potential given a model of pressure and/or redox potential and prescribed values of electrical resistivity. The numerical procedure is verified to be accurate and stable through a comparison with synthetic simulations. The capacity for producing 2-D reconstruction of transient or steady state flow models in anisotropic, heterogeneous and water-saturated porous materials is illustrated throught the model of a leak in a dam, the case of a pumping test in an unconfined aquifer and the problem of coupled hydroelectric problem associated with the presence of a cavity.

A new laboratory apparatus is presented to explain the physical and chemical mechanisms that generate self-potential anomalies in the vicinity of buried metallic objects and to validate a linear inversion algorithm. The controlled laboratory experiment involves a metallic body buried with vertical orientation and centered through and in the capillary fringe within a sandbox. Preliminary tests were performed to choose a right sand through a performance comparison among different materials and to evaluate approaches to remove electrode effects and provide adequate corrections. Large dipolar self-potential anomalies developed in association with the progressive corrosion of the vertical body. The inverse problem is solved by accounting for the electrical conductivity distribution and the self-potential data in order to recover the source current density vector field using a 2-D LSQR finite-element modeling approach. This experiment indicates that passively recorded electrical signals can be used to nonintrusively monitor

corrosion processes, lending support to the geobattery model over organic contaminant plumes. Furthermore, synthetic and real simulations, performed on heterogeneous models with anomalies included, provide low-error inverted models whereas anomalies are well-detected both for shape and position. In particular the inversion algorithm was applied to a field data set collected in the San Vittorino Plain, located in Central Italy, in order to identify the location of sinkholes and investigate the effects of different resistivity structure assumptions on the SP inversion results.

The whole geophysical process (data processing, forward modelling and inversion) has been included through an interactive Matlab algorithm divided in sections, where the operator can act to change. The algorithm is suitable for laboratory and field investigations, because of its high flexibility and reliability now reached by forward and inversion routines, with the primary aim of extending the approach to engineering and environmental applications.

Riassunto

I potenziali spontanei sono potenziali elettrici quasi-statici di origine naturale generati da sorgenti distribuite nel sottosuolo. Le componenti principali sono il potenziale elettrochimico legato alla presenza del gradiente del potenziale redox e il potenziale elettrocinetico prodotto dal flusso dell'acqua che circola nei mezzi porosi.

Al fine di riprodurre tali segnali di potenziale spontaneo in mezzi saturi eterogenei e anisotropi caratterizzati da geometrie complesse, l'attività di ricerca è stata incentrata sull'implementazione di un algoritmo in Matlab. La soluzione del problema diretto 2-D è stata ottenuta a partire da un modello di pressione o potenziale redox e dalla distribuzione di resistività elettrica tramite la formulazione numerica dell'equazione di Poisson. L'algoritmo agli elementi finiti sviluppato si è dimostrato essere stabile e accurato mediante procedure di simulazione rispetto a casi di studio sintetici e reali riportati in letteratura. Nel dettaglio, si è verificato che questo approccio può essere utilizzato per produrre modelli 2-D per l'individuazione e caratterizzazione dei flussi di infiltrazione d'acqua (seepage) attraverso i corpi-diga, per l'interpretazione di prove di emungimento e per l'identificazione e localizzazione di cavità isolate/forme carsiche superficiali esistenti, le quali costituiscono naturali vie di convogliamento delle acque meteoriche incidenti e corrivanti sulla superficie topografica nel sottosuolo.

Per approfondire lo studio del potenziale elettrico generato dalla presenza di corpi metallici sepolti e validare l'algoritmo presentato per l'inversione dei dati di potenziale spontaneo, è stato effettuata una prova sperimentale. Sono state eseguite misure 2-D di potenziale e resistività elettrica su un modello fisico di laboratorio capace di simulare un acquifero, favorire le reazioni di ossido-riduzione e lo sviluppo progressivo dell'anomalia negativa in corrispondenza di un elemento in ferro a seguito del processo di corrosione. Test preliminari di laboratorio hanno messo in luce i principali problemi della campagna di misura provocati dalla tipologia di sabbia utilizzata e dagli errori di misura sugli elettrodi. L'apparato sperimentale, dopo opportune modifiche e la minimizzazione dei suddetti errori,

ha fornito misure stabili e ripetibili. I valori di potenziale spontaneo acquisiti in profondità e quelli di conducibilità elettrica sono stati forniti all'algoritmo di inversione basato sul metodo LSQR e utilizzati per ricostruire fedelmente la distribuzione della densità di corrente esterna, nonchè per riprodurre il modello di "geo-batteria". Inoltre, simulazioni numeriche eseguite su un sintetico di laboratorio e su dati di campagna acquisiti nell'ambito di un'indagine condotta per la localizzazione di sinkhole incipienti nella piana di San Vittorino (RI), hanno fornito dei modelli finali con valori limitati di errore e una buona ricostruzione delle anomalie sia in termini di forma che posizione.

L'intero processing geofisico (elaborazione dei dati, modellazione e inversione) è stato incluso all'interno di un codice in Matlab interattivo, il quale consente di lavorare sia su dati ricavati da indagini di campagna che su quelli ottenuti da sperimentazioni in laboratorio grazie alla flessibilità e affidabilità raggiunta dalla modellazione e dall'inversione, con l'obiettivo primario di estendere tale approccio risolutivo alla più ampia casistica di applicazioni del metodo del potenziale spontaneo dal punto di vista geologico, in ambito idrogeologico, in campo ambientale e ingegneristico.

Contents

Abstract **1**

Riassunto **3**

Contents **6**

List of Tables **7**

List of Figures **12**

1 Introduction **13**

1.1 Environmental Geophysics 13

1.2 An overview of the self-potential method 15

1.3 Thesis objective and outline 17

2 Self-potential method **19**

2.1 The origin of self-potentials 19

2.2 Electrical double layer 22

2.3 Streaming potential 24

2.4 Electrochemical potential 28

2.5 Field procedures 31

2.6 Sources of noise 36

3 Forward problem **39**

3.1 Governing equation 39

3.2 Finite element formulation 42

3.3 Assembling the stiffness matrix 45

3.4 Assembling the right-hand side 46

3.5 Incorporating Dirichlet conditions 46

3.6 Mesh geometry 47

3.7 Synthetic tests 49

3.7.1 Pumping test 49
3.7.2 Leakages in dams 53
3.7.3 Localization of cavities 55

4 Inversion of SP data **59**
4.1 Methodology 60
4.2 Tikhonov regularization 63
4.3 LSQR method 64
4.4 Generalized cross-validation 66
4.5 Proposed algorithm 69

5 Application to laboratory and field investigations **74**
5.1 Laboratory experiment 74
5.1.1 Material and methods 75
5.1.2 Preliminary tests 78
5.1.3 Synthetic example 83
5.1.4 Data acquisition and inversion 83
5.2 Field survey: the San Vittorino Sinkhole Plain 91
5.2.1 Hydrogeological background 91
5.2.2 Data acquistion 94
5.2.3 Inversion of field data 94

6 Conclusions **99**

Bibliography **102**

List of Tables

2.1 Coupled forces and fluxes (after [74], modified). 20

3.1 Model parameters for the synthetic case study. 50
3.2 Model parameters for the synthetic case study. 54
3.3 Material properties used in the numerical simulation. 57

4.1 Structual index of different sources. 62

5.1 Properties of the two sands used in the experiment. 80

List of Figures

2.1 Sketch of the electrical double layer at the pore water–mineral interface coating a spherical grain (after [104], modified). In the present case (negatively charged mineral surface), M^+ denotes the counterions while A^- denotes the coions. The pore water is characterized by a volumetric charge density Q_v corresponding to the (total) charge of the diffuse layer per unit pore volume (Cm^{-3}). . 23

2.2 Convection and conduction currents in a saturated pore channel (after[74]). 26

2.3 Quasi-static charge density Q_v (excess pore charge moveable by the quasi-static pore water flow) versus the hydraulic conductivity K for a broad collection of core samples and porous materials (after [122]). 27

2.4 The Sato and Mooney (1960) geobattery model whereby the redox gradient is attributed to the gradient of dissolved oxygen in groundwater and the ore body serves as the electron conductor (after [7]). 30

2.5 Typical recording system to monitor the self-potential response. Picture showing the non-polarizing electrodes and the recording multielectrode voltmeter. 32

2.6 Schematic representation of the reference correction on a closed SP-profile. The orange arrows represent the shift of the data, section by section (after [8]). 34

2.7 Example of the closure correction of SP data in a closed profile composed of 10 datapoints. Point 0 and point 10 are geographically the same (after [8]). 35

2.8 Self-potential and self-potential gradient along a profile across bodies with varying depth to the top (z_1) (after [14], modified). 36

2.9 Example of self-potential data during a dipole pumping/injection test. (a) Raw data. (b) Detrended data. We can recognize five phases in the pumping test: I corresponds to the data obtained prior to the start of the pumping test; II is the transient phase during pumping; III is the steady-state phase; IV is the rapidly changing portion of the recovery phase; and V corresponds to the slowly changing to steady-state portion(s) of the recovery phase (after [59]). 38

3.1 Flowchart for the forward modeling of the self-potential data associated with groundwater flow and redox gradient. 42

3.2 Three different 2D adaptive meshes (with their quality histograms) built by Netgen. Triangular meshes are used to discretize the domain for the finite element simulations of the ground water flow problem and the resolution of the semi-coupled SP problem of a dam model with the presence of a leak (a, b), a volcano with permeable conduits (c, d) and a sinkhole (e, f). 48

3.3 Sketch of the pumping test. Petrophysical parameters (T and S are the aquifer transmissivity and storativity, respectively, σ is the electrical conductivity) as well as the initial head distribution $h_o = 48$ m, and the pumping rate $Q = 2.7$ ls^{-1} are involved into the numerical computations. 50

3.4 Modelled hydraulic head at the end of the pumping phase using MaxSym (red circles) and synthetic data from [135] (black triangles). 51

3.5 Cross-section of the synthetic SP radial distribution around the pumping well (only one side is modeled, because of the symmetry of the problem with an axis of symmetry corresponding to the well). (a) Streaming potentials obtained by adopting the finite element algorithm. (b) Computed SP signal from [135]. 52

3.6 Leakage in a dam. (a) 2-D geometry used for the simulation showing a preferential flow pathway crossing the dam and Darcy velocity map obtained by solving the groundwater flow problem. (b) Triangular meshes used to discretize the domain for the finite element simulation. 53

3.7 Self-potential values from the forward model showing the position of the anomalous flow path through the core of the embankment dam. (a) Simulation of the self-potential signals using the finite element numerical algorithm with reference at infinity. (b) Numerical modeling of the synthetic case reported by [54]. 55
3.8 Geometrical model used for the finite element calculation. The boundary conditions are discussed in the main text. 57
3.9 Comparison between the self-potential signals calculated by the forward algorithm presented in this thesis (a) and the distribution of the SP determined numerically by [58] using the finite element numerical model Femlab (b). 58

4.1 Scheme of the subspace preconditioned LSQR (after [57]). 67
4.2 Flowchart of the inverse algorithm for searching the best source current density model. 70

5.1 Sketch of the experimental setup showing the location of depth SP data points (upper right) and the position of surface data points (lower right) for the actual experiment, the iron bar installed during placement of sand (upper left) and patterns of ferric staining of pore fluid and sand below the phreatic surface at the conclusion of the study (lower left). 76
5.2 Cross section of the cylinder showing the elevation of the established phreatic surface and the metallic body buried in the capillary fringe. 77
5.3 Photos showing the Ag/AgCl nonpolarizing electrodes and the high-impedance voltmeter during the SP data acquisition along the cross section. 77
5.4 Photos showing the gold electrodes and the Syscal-Pro resistivimeter during the resistivity data acquisition along the central profile of the measuring grid. 78
5.5 Evolution of self-potential data at the surface of the tank in presence of river sand. Black crosses indicate positions of the self-potential stations. 79
5.6 Comparison between the self-potential profiles at four different times. Raw data collected over 5 days on (a) river sand and (b) silica sand. (c) Configuration of the tank used in the preliminary test with the position of the electrodes. 81

5.7 Surface self-potential maps after replacing the river sand with the finer particles of the silica sand. 82
5.8 Self-potential data processing. (a) Three steps to obtain correction of raw SP data. (b) Configuration of the sandbox used in the preliminary test with the position of the electrodes. 84
5.9 Synthetic example.(a) True source current density.(b) Result of the inversion using LSQR algorithm.(c) Distribution of the electrical conductivity. 85
5.10 The self-potential signal calculated at the surface of the model (z=20 cm). 86
5.11 Sequence of 2D SP data (plan-view) collected on the surface of the sand in experiment. Redox processes resulted in the development of a -45 mV anomaly in two months (*Figure continues on page 81*). 87
5.11 -*Continued*. 88
5.12 2D vertical cross section of SP data collected on day 60 of experiment. A relatively large dipolar perturbation in the electrical potential field can be seen to have developed along the vertical iron bar. 88
5.13 Picture showing the almost totally clean surface of the bar after a week (upper) and the presence of lepidocrocite at the end of the experiment (lower). 89
5.14 2D resistivity tomography. The resistivity ranges from 200 ohm-m in the saturated portion of the tank (and in the capillary fringe) to nearly 3500 ohm m close to the top surface of the tank. 90
5.15 Inversion results showing color contour plots of the (a) observed and (c) recovered SP depth data, and (b) magnitude of the current density distribution $\mathbf{J_s}$. 92
5.16 Simplified geological map of the sinkhole-prone area in the S. Vittorino Valley (Latium) with a borehole data stratigraphic column (after [81]). 93
5.17 Aerial plan of the surveyed area and position of the ERT and SP line. 95
5.18 (a) Inverted model of ERT line. (b) Inverted model of STR line (after[23], modified). Black arrow indicates the sinkhole marked as A. Black dashed lines indicate the shape of the anomalous zones. 96

5.19 Inversion results. (a) Magnitude of the inverted two-dimensional streaming current source density accounting for the resistivity distribution shown on Figure 5.18. (b) Distribution of the reconstructed self-potential signals. 97
5.20 Determination of the regularization parameter using the GCV method. 98
5.21 Comparison between the self-potential signals determined at the ground surface using the inversion algorithm (empty circles) and the self-potential measurements performed along profile (filled circles). 98

Chapter 1

Introduction

1.1 Environmental Geophysics

Geophysics applies the knowledge and methods of physics, mathematics and chemistry to understand the structure of Earth and its environment. Detailed characterization of the subsurface is critical in environmental, groundwater, and geotechnical investigations, as well as tectonics, mining, and petroleum reserve studies.

As the range of applications of geophysical methods has increased, particularly with respect to contaminated land investigations, the discipline of "environmental geophysics" has developed in the last decades. This is due to several reasons: (i) the increasing awareness of environmental problems (ii) the continuing improvement in survey equipment performance, automation and information resolution of sensors and devices; (iii) the advances in processing and imaging software. In particular, two sub-disciplines have been introduced: hydrogeophysics (geophysics in groundwater investigations; [90, 110, 138]) and bio-geophysics (geophysical manifestation of microbial activity within geological materials; [7]).

Hydrogeophysics has grown since 1990s as a multi-disciplinary subject that focuses on the use of geophysical methods for characterising subsurface features, determining hydrogeological properties and monitoring processes relevant to soil and groundwater processes.

The subdiscipline of bio-geophysics has emerged over the last decade or so and examines the geophysical signatures of microbial cells in the Earth, the interaction of microorganisms and subsurface geological materials, and alteration of the physical and chemical properties of geological materials as a result of microbial activity.

Environmental geophysics is used to characterize subsurface conditions for

geologic, hydrogeologic and engineering investigations, as well as to assess the occurrence and potential for impact of hazardous materials and chemical contamination [47, 106, 125, 139].

Electromagnetic (EM) methods in general are highly sensitive to water content and are therefore most suitable for addressing the problems related to subsurface physical properties and processes. Furthermore, the reason for the success of the application of EM methods to environmental problems lies in the variation of conductivity caused by different geometry of pore fluids and clay contents in rocks, and by the presence of organic and inorganic contaminants [113, 132]. Among these geophysical techniques, ground penetrating radar (GPR) technology is of particular interest for providing high-resolution subsurface images and specifically addressing water-related questions, including GPR applications in environmental studies, such as the characterization of abandoned landfills: thickness of the deposit, location of metal and non-metal objects (barrels, voids, etc.), soil profiles, groundwater level and contaminant plume [64, 85, 97].

During the last two decades, various seismic methods have been developed and widely used to study the shallow subsurface to engineering, environmental and groundwater-related investigations. For example, the shallow-reflection technique has recently been used in mapping bedrock beneath alluvium in the vicinity of hazardous waste sites, detecting abandoned coal mines, following the top of the saturated zone during pump tests in alluvial aquifers, and in mapping shallow faults [118, 126].

Geoelectrical methods, commonly used in hydrogeological, mining and geotechnical investigations, have also been widely and successfully utilized for environmental surveys in the past twenty years [34, 67, 145]. The resistivity data can be used to identify, delineate and map the subsurface defining such things as electrical conductor contamination plumes, lithologic units with clay, the salt water/fresh water interface and the vadose zone. Besides the resistivity, in last decade, the Induced Polarization (IP) technique have been affirmed as one of the most important methods for detection of contamination plumes [20, 25], investigation of waste dumps [22, 141] and monitoring of in-field bio-remediation [30].

The self-potential (SP) method has been a breakthrough method in the past few decades for a broad range of applications, including hydrology [17, 130], geothermal and volcanic systems [33, 77], geotechnical and environmental engineering [32, 116], mineral exploration [53, 111], and petrophysics [55, 68].

1.2 An overview of the self-potential method

The self-potential method involves the passive measurement of the electrical potential distribution at the ground surface of the Earth with non-polarizable electrodes. SP anomalies are associated with charge polarisation mechanisms occurring at depth. The two main mechanisms are (1) the streaming potential due to electrokinetic coupling [13, 45] and (2) the "electro-redox" effect associated with redox potential gradients [31, 79, 80]. All these mechanisms are related to chemical potential gradients of charges carriers creating polarization in the porous media.

Since the first measurements of self-potential by Fox [44], the method has been applied to mineral exploration, oil well logging and geothermal exploration. Early research for explaining all driving forces that give rise an SP response can be attributed to Marshall and Madden [69], Sato and Mooney [111] and Nourbehecht [82]. Historically, the self-potential method has been mainly used in qualitative analysis of the measured data. However, in the last decades, many researches have given a more quantitative interpretation of SP anomalies for hydrogeological, environmental and engineering applications. Many methods of interpretation were developed for self-potential data.

Geometric source techniques, originally employed to infer the locations of SP anomalies associated with ore bodies, are based on the assumption that the sources may be approximated by a polarized model of simple geometry. Curve-matching [39, 72] and parametric curve [11, 87] have been used to recover source parameters such as the surface location, depth, geometry and dip or polarization angle of the body.

In this context, source image methods have been applied to reconstruct the most probable location and shape of discrete SP buried sources, by estimating the position of their centres and critical points of their boundaries, as corners, wedges and vertices. These methods assume that measured SP data result from the aggregation of poles, dipoles, quadrupoles and octopoles in the subsurface, and consequently they must employ normalized cross-correlation to enable a comparison of sources at different depths. These approaches aim to locate self-potential sources in terms of a charge occurrence probability (COP) function [40] and a dipole occurrence probability (DOP) function [56, 100]. Within the framework of numerical approaches, the conventional and extended Euler deconvolution has been used to determine location, depth and geometry of the causative source [4]. Shape factor, depth and polarization angle for simple geometries of source models have been also estimated by sophisticated optimization methods, such as genetic

algorithms [2], particle swarm optimization [89], very fast simulated annealing [14] and ant colony optimization [124]. Source parameters have been also retrieved through automatic imaging methods, aiming at improving the interpretation of potential field anomalies related to mining and environmental studies [1].

Other methods are based on the continuous wavelet transform, which allows the characterization of discontinuities or abrupt changes in the measured signal and a quick analysis of potential field data [41, 78].

Forward modeling methods have been developed to predict the self-potential response to a primary fluid flow field. Sill [119] was the first to introduce a physics-based approach to simulate numerically the occurrence of SP anomalies associated with ground water flow. He used the finite-difference method. Later, the streaming potential problem has been solved with the finite element approach [58, 99, 142] and the finite volume approach [116].

The inversion of SP data provides a more rigorous means of interpreting a subsurface distribution of current sources. Shi [117] implemented an inversion method for 3D self-potential which requires a priori information to improve the robustness of the solution. Minsley et al. [74] further developed this inverse procedure by introducing sensitivity scaling and constraints. They performed an inversion of SP data to define the shape and extension of a contaminant plume where redox processes are occurring [75]. Linde and Revil [66] solved the Poisson equation to determine the distribution of the redox potential versus depth over a contaminant plume associated with the presence of a municipal landfill. Mendonca [73] proposed an algorithm to invert self-potential signals to delineate the position of ore bodies at depth using the geobattery model developed by [128]. Soueid Ahmed et al. [121] introduced a finite element algorithm for localizing the causative source of self-potential signals associated with ground water flow. All these models generally include the distribution of the electrical resistivity as prior information in the inversion process.

Most recent applications of the SP method have been hydrologic investigations aimed at mapping fluid flow patterns [18, 54], reconstructing the geometry of the water table [13, 59], and determining hydraulic parameters of porous media and aquifers [19, 70]. Several other recent efforts have included the detection and imaging of groundwater infiltration into subsurface voids and sinkholes [60], investigating geothermal system and volcanic vent characteristics [107], and the localization of hydromechanical disturbances associated with hydraulic fracturing activities and other natural or manmade seismic sources [48, 84].

1.3 Thesis objective and outline

The purpose of the research presented in this thesis is to develop numerical algorithms for modeling and inversion of self-potential signals generated by both electrokinetic and electrochemical mechanisms. The idea is to accomplish this approach by focusing the problem into the following four primary objectives:

1. Present a new 2-D forward solver for predicting the SP response and validate the finite element numerical solution through comparison with approaches and synthetic examples reported by other authors;

2. Conduct a laboratory experiment to test the geobattery model associated with the corrosion of a metallic body and to investigate the physical properties that govern the occurence of the self-potential signals;

3. Develop an inversion algorithm to evaluate the spatial distribution of the source current density within the near-field regiojnns of electrical charge carriers in the subsurface;

4. Validate the numerical algorithms through laboratory experiments and field surveys.

Chapter 2 provides background information regarding the general behavior of the coupled phenomena and the origin of self-potential signals generated by hydraulic and chemical forcing mechanisms. The chapter illustrates a conceptual pore-scale model of streaming potential and a theoretical basis for the geobattery model used to localize ore bodies and, more recently, to explain some strong self-potential anomalies observed, under some specific circumstances, over contaminant plumes.

Chapter 3 introduces a 2D finite element algorithm for calculating the self-potential distribution. The algorithm was developed to enable the study of problems of complex geometry for application to engineering, environmental and hydrogeological investigations. The chapter outlines the development of the forward modeling scheme, which involves discretization of the domain and coupled flow equations, and application of the boundary conditions. A serie of examples comparing predicted and measured self-potential data are presented with the application of the numerical procedure to studies in the literature. The discussion of the numerical solution technique includes the application of MaxSym, a Matlab tool which is designed specifically to simulate axisymmetric flow (Louwyck et al., 2012), for a pumping test analysis, and the utilization of the coded algorithm in Matlab for a comprehensive solution of the other SP problems.

Chapter 4 describes the inversion algorithm for recovering a two-dimensional source current density distribution from measured self-potential data. This approach enables to extract pertinent information about the underlying hydraulic or chemical regime from the geophysical data, and permits to include the effect of heterogeneous conductivity distributions. The inverse problem is solved by minimizing a model objective function to recover the simplest source current density model that leads to an acceptable fit with the observed self-potential data.

Chapter 5 shows inversion results from 2-D laboratory investigations and field surveys. The chapter introduces a laboratory apparatus designed to measure electro-redox potentials generated by a metallic iron bar inserted in a cylinder Plexiglas sandbox filled with a calibrated sand partially infiltrated by water. In addition to this, also a real example is reported to understand potential and limits of the of the inversion reconstruction where streaming potential is the dominant mechanism. These examples also serves to demonstrate how prior information about the hydraulic, chemical and electrical flow systems can be used to help constrain the solution. Finally Chapter 6 summarized the key finding of the research, discusses the practical contributions and comments on area of future challenges.

Chapter 2

Self-potential method

The self-potential or spontaneous polarization method is a passive geophysical technique based on the measurement of the electric potential resulting from various electrochemical processes occurring in the subsurface.

This Chapter provides background information regarding the origin of self-potential signals generated by hydraulic and chemical forcing mechanisms and discusses the principle of the measurements, strategies to map or monitor the self-potential field and the sources of noise. It also gives a short overview of the electrical double layer coating the surface of the minerals. Indeed, a good understanding of the electrical double layer is of paramount importance in the study of self-potential signals.

2.1 The origin of self-potentials

Self-potentials are the result of coupling between electric and non-electric flows and forces in the earth. On the macroscopic scale, coupled transport phenomena are typically discussed in the context of non-equilibrium thermodynamics (e.g. [38]), and it is assumed that fluxes are linearly related to driving forces. This results in a linear system of coupled equations (2.1), where L_{ij} are phenomenological coupling coefficients that link the forces F_i to fluxes Γ_i:

$$\begin{bmatrix} \Gamma_1 \\ \Gamma_2 \\ \Gamma_3 \\ \Gamma_4 \end{bmatrix} = \begin{bmatrix} L_{11} & L_{12} & L_{13} & L_{14} \\ L_{21} & L_{22} & L_{23} & L_{24} \\ L_{31} & L_{32} & L_{33} & L_{34} \\ L_{41} & L_{42} & L_{43} & L_{44} \end{bmatrix} \begin{bmatrix} F_1 \\ F_2 \\ F_3 \\ F_4 \end{bmatrix} \tag{2.1}$$

Onsager [83] showed that, for small flows, the matrix of coupling coefficients is symmetric (i.e. $L_{ij} = L_{ji}$). Because of the coupling described by Equations in

(2.1), it is also possible to have contributions to any of the fluxes from any other non-conjugated forcing, i.e:

$$\mathbf{\Gamma}_i = \sum_j L_{ij}\mathbf{F}_j \tag{2.2}$$

All sixteen possible phenomena are summarized in Table 2.1. The table lists primary and coupled flow phenomena and illustrates the interdependence of fluid, temperature, electrical and ionic system. Primary flow laws are listed as diagonal terms and coupled flow phenomena are listed as off-diagonal terms.

Table 2.1: Coupled forces and fluxes (after [74], modified).

	Electric gradient	**Hydraulic gradient**	**Chemical gradient**	**Temperature gradient**
Electric	*Ohm's Law*	Electrokinetic effect	Electro-diffusion	Seebeck effect
Fluid	Electro-osmosis	*Darcy's Law*	Chemico-osmosis	Thermo-osmosis
Solute	Electrophoresis	Ultrafiltration	*Fick's Law*	Soret effect
Heat	Peltier effect	Therma filtration	Dufour effect	*Fourier's Law*

When more than one flow exists in a system, each flow could be represented as a combination of all other forces. As a result, the total electric current density, i.e. $\mathbf{J}$ (Am^{-2}) could be expressed as:

$$\mathbf{J} = \mathbf{J}_c + \mathbf{J}_K + \mathbf{J}_D + \mathbf{J}_T, \tag{2.3}$$

where $\mathbf{J}_c, \mathbf{J}_K, \mathbf{J}_D$ and $\mathbf{J}_T$ are conduction current, streaming current, diffusion current and current due to temperature gradient, respectively [74]. The conduction current can be written as:

$$\mathbf{J}_c = \sigma\mathbf{E}, \tag{2.4}$$

where σ is the electrical conductivity (Sm^{-1}) and $\mathbf{E}$ the electric field (V).

The self-potential problem, by definition, is concerned only with currents that vary on the time scale of the forcing mechanism, which is generally very slow for processes in the earth [74]. Therefore, the quasi-static form of Maxwell's equations can be applied:

$$\nabla \times \mathbf{E} = -\frac{\partial \mu \mathbf{H}}{\partial t} \simeq 0 \tag{2.5}$$

$$\nabla \times \mathbf{H} = \frac{\partial \varepsilon \mathbf{E}}{\partial t} + \mathbf{J} \tag{2.6}$$

$$\nabla \cdot \varepsilon \mathbf{E} = \rho \tag{2.7}$$

$$\nabla \cdot \mu \mathbf{H} = 0, \tag{2.8}$$

where $\mathbf{H}$ is the magnetic field (Am^{-1}), μ the magnetic permeability (Hm^{-1}), ε the electric permittivity (Fm^{-1}) and ρ the charge density (Cm^{-3}),

By neglecting the magnetic induction in Faraday's Law (Equation (2.5)) the electrical field is conservative and it consequently can be derived from the gradient of a scalar potential Ψ, expressed in V:

$$\mathbf{E} = -\nabla \Psi. \tag{2.9}$$

Taking the divergence of Ampère's Law (Equation(2.6)):

$$\nabla \cdot (\nabla \times \mathbf{H}) = \nabla \cdot \left(\frac{\partial \varepsilon \mathbf{E}}{\partial t} + \mathbf{J} \right) = 0, \tag{2.10}$$

and substituting Gauss' Law (Equation(2.7)) yields the equation for the conservation of charge:

$$\nabla \cdot \mathbf{J} = -\frac{\partial \rho}{\partial t}. \tag{2.11}$$

For the quasi-static case, the time derivative of the charge density is neglected, resulting in the familiar equation for the conservation of current:

$$\nabla \cdot \mathbf{J} = 0. \tag{2.12}$$

This means that the total current density is conservative (all the current entering a control volume must also exit in the absence of sources and sinks; there is no storage of electrical charges inside the control volume).

Substituting Equation (2.3) into Equation (2.12), and separating the forcing from the electrical response, the self-potential field Ψ is the solution of the following elliptic (Poisson-type) equation:

$$\nabla \cdot (\sigma \nabla \Psi) = \nabla \cdot \mathbf{J}_s = s, \tag{2.13}$$

where the source current density s (Am^{-3}) equals the divergence of the sum of

the current densities due to the forcing mechanism(s), i.e.:

$$\mathbf{J}_s = \mathbf{J}_K + \mathbf{J}_D + \mathbf{J}_T = \sum_{j \neq 1} L_{1j} \mathbf{F}_j. \tag{2.14}$$

Equation (2.13) is the fundamental field equation in the interpretation of (quasi-static) self-potential signals. It states that an electrical potential distribution is created by a source term, corresponding to the divergence of a source current density. The coupling coefficients, L_{ij} , found in the source term clearly play an important role in determining the self-potential response. A significant amount of research has therefore gone into understanding the coupling coefficients for various forcing mechanisms (e.g. [29], [98]). While the coupling coefficient is not a focus of this thesis, a brief review of the coupling for electrokinetic and electrochemical processes is presented in Sections 2.3 and 2.4 as the concepts are relevant to subsequent discussions.

2.2 Electrical double layer

Before proceeding with the description of the self-potential signals, it is worth describing the concept of the electrical double layer (often described as a triple layer) at the pore water–mineral interface, because of its importance in all that follows.

The innermost layer is the solid surface having a net electrical charge, either positive or negative, which is controlled by surface chemistry. Factors influencing the polarity of this charge include for example mineralogy or chemical composition of the solid particles, pH of the pore fluid or imperfections in the molecular or lattice structure of the solid [129]. For instance, clay particles are negatively charged due to isomorphous substitution, incomplete occupation of the positions available for metal ions and release of protons from hydroxides. At near-neutral pH values, the negative surface charge of the mineral attracts the ions of positive sign (counterions) in the fluid and repels the ions of the same sign (coions). The positively-charged region of sorbed ions adjacent to the mineral surface constitutes the second layer, called the Stern (or fixed) layer [127]. The Stern layer is located between the o-plane (mineral surface) and the d-plane, which is the inner plane of the more loosely bound electrical diffuse or Gouy layer [102] (Figure 2.1). This third layer is made of free ions that move in the fluid under the influence of electric attraction and thermal motion rather than being firmly anchored. Because of this, the relative movement between solid and liquid tends to cause the

transport of some of the charges, creating an electric current (see Section 2.3).

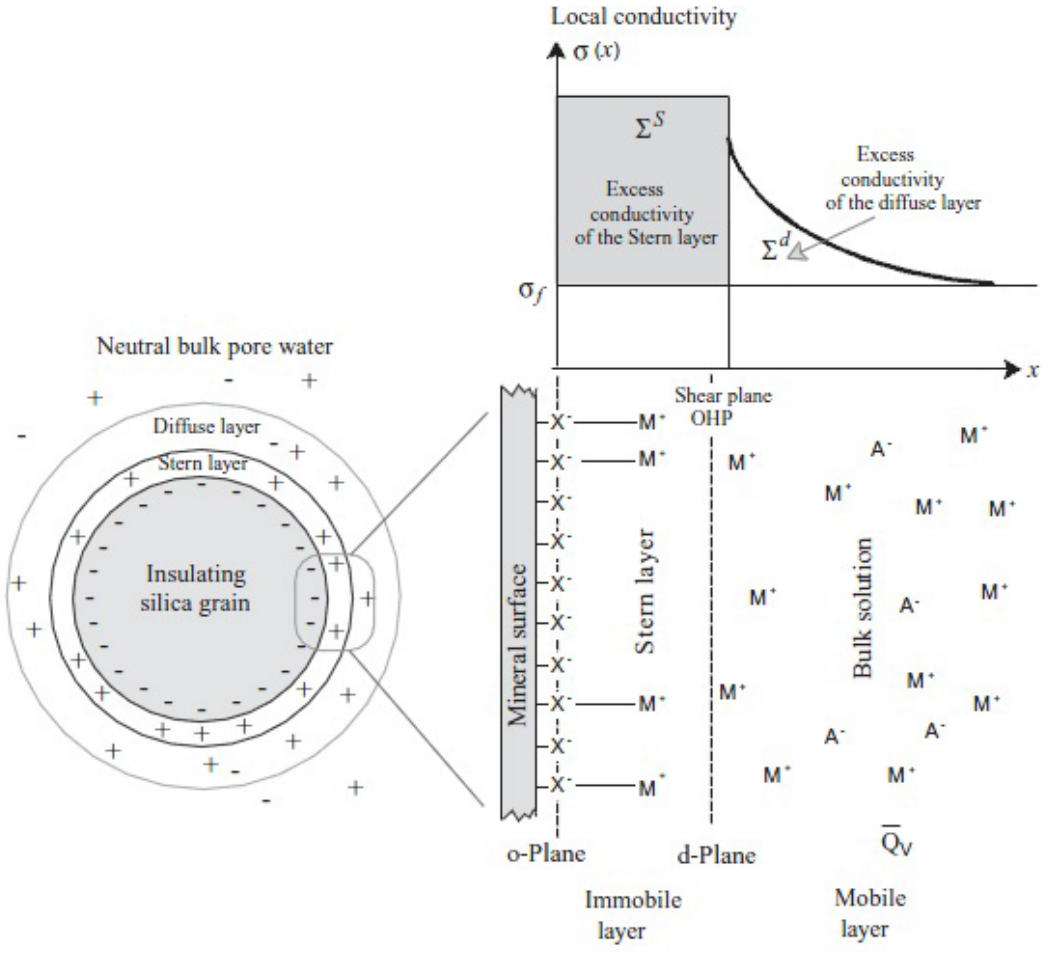

Figure 2.1: Sketch of the electrical double layer at the pore water–mineral interface coating a spherical grain (after [104], modified). In the present case (negatively charged mineral surface), M^+ denotes the counterions while A^- denotes the coions. The pore water is characterized by a volumetric charge density Q_v corresponding to the (total) charge of the diffuse layer per unit pore volume (Cm^{-3}).

There are three fundamental consequences associated with the existence of the electrical double layer [104]:

1. The pore water is never neutral;
2. There is an excess of electrical conductivity in the vicinity of the pore water–mineral interface responsible for the so-called surface conductivity;
3. The double layer is responsible for the (non-dielectric) polarization of the porous material.

The first consequence is fundamental to understanding the nature of electrical

currents associated with the flow of the pore water (see Section 2.3); therefore, the occurrence of self-potential signals associated with ground water flow.

The second consequence is crucial to the understanding of electrical conductivity in porous materials, and to the interpretation of resistivity data. The local conductivity $\sigma(\mathrm{x})$ depends on the local distance x from the charged surface of the mineral. The Stern layer is responsible for the excess surface conductivity Σ^S (S) with respect to the conductivity of the pore water σ_f while the diffuse layer is responsible for the excess surface conductivity Σ^d (Figure 2.1). These surface conductivities are sometimes called specific surface conductance because of their dimension but they are true surface conductivities.

The third consequence is important to the understanding of induced polarization, which translates into the frequency dependence of the electrical conductivity.

2.3 Streaming potential

Streaming potentials result from the coupling between fluid flow and electric conduction in porous media, a phenomenon known as the electrokinetic effect [55]. This generates a macroscopic electrical field due to the movement of pore water through the capillary or porous medium.

In the absence of significant chemical concentration or temperature gradients the coupled flow equations that describes electrokinetic processes in a water-saturated medium heterogeneous are [119]:

$$\mathbf{u} = -\frac{k}{\mu}\nabla P - k_e \nabla \Psi, \tag{2.15}$$

$$\mathbf{J} = -L_{\nabla P}\nabla P - \sigma \nabla \Psi, \tag{2.16}$$

where k is the intrinsic permeability of the porous medium (m^2), μ the dynamic shear viscosity of the pore water (Pa s) and P the pressure (Pa). The hydraulic gradient is expressed in terms of $\nabla P = \rho_w g \nabla h$, where ρ_w denotes the mass density of the pore water (Kgm^{-3}), g the acceleration of the gravity (ms^{-2}) and h the hydraulic head (m). Using this convention, the phenomenological coupling coefficients take the form of the pressure gradient $L_{\nabla P} = \frac{L_{ji}}{\rho_w}$ ($\mathrm{A}^2\mathrm{Kg}^{-1}$), the coefficient of electro-osmotic permeability $k_e = \frac{L_{ij}}{\rho_w}$ $(\mathrm{m}^2(\mathrm{sV})^{-1})$, the electrical conductivity σ (Sm^{-1}) and $\frac{k}{\mu}.-k_e\nabla\Psi$ describes electro-osmotic fluid flow due to the viscous drag of the pore water associated with the displacement of the excess of electrical charge in an electrical field while $-L_{\nabla P}\nabla P$ describes streaming

current flow due to the drag of the electrical excess charge contained in the electrical diffuse layer.

In the study of the streaming potential phenomenon, Mitchell [76] reported negligible contribution of the electro-osmotic flow term in materials with $K > 10^{-9}$ ms^{-1}. Hence, fluid flow in cohesionless soils and most broadly graded glacial tills is governed by the primary hydraulic gradient, and Equation (2.15) is reduced to Darcy's law. For most geologic materials, the quantity $\frac{\frac{k}{\mu}\sigma}{k_e}$ are order 10^3 to 10^7 [42]. Therefore, the contribution of the primary flow term to the overall fluid flow will be much greater than that of the coupled flow term, regardless of the hydraulic conductivity of the material [115].

According to the convection current model proposed by [119], coupled electrical current flow can be described by a convection current or streaming current $\mathbf{J}_{conv}$, induced by the hydraulic gradient, and a conduction current $\mathbf{J}_{cond}$, induced by the resultant separation of charge within the porous medium. Equation (2.16) can be expressed in terms of these two current densities:

$$\mathbf{J} = \mathbf{J}_{conv} + \mathbf{J}_{cond}, \tag{2.17}$$

where:

$$\mathbf{J}_{conv} = -L_{\nabla P}\nabla P, \tag{2.18}$$

$$\mathbf{J}_{cond} = -\sigma\nabla\Psi. \tag{2.19}$$

Figure 2.2 presents this conceptual pore-scale model of streaming potential. Under static no-flow conditions, the saturated medium is electrically neutral with adsorbed ions from the fluid completely balancing the negative surface charge of the solid particles. The onset of fluid flow pulls positive ions from the diffuse outer layer in the direction of flow, which generates the electrical current $\mathbf{J}_{conv}$ while a charge imbalance results from the movement of ions in the direction of flow, which induces the opposing conduction current, $\mathbf{J}_{cond}$. The convection and conduction currents balance each other under steady-state fluid flow conditions, and create a closed current loop. Although the streaming current is strictly limited to the saturated pore channels, the conduction current permeates the entire medium and may be quantified with self-potential measurements [115].

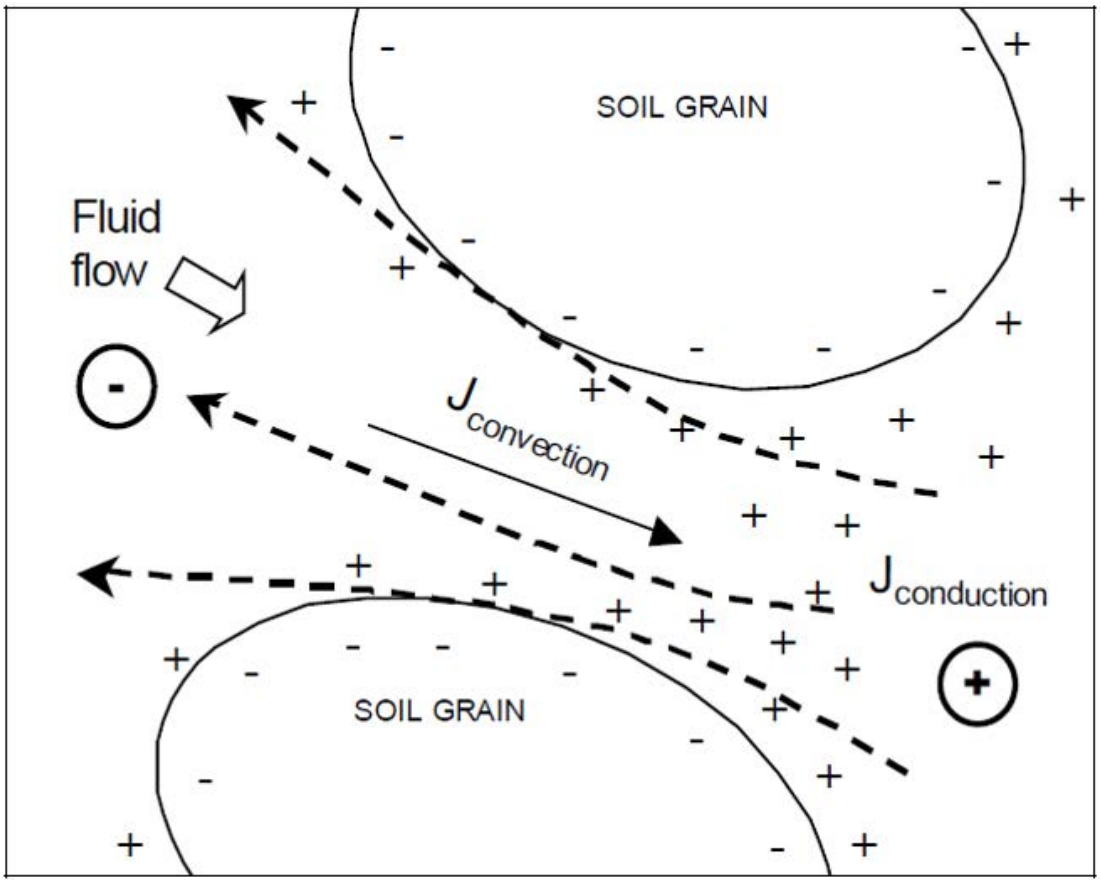

Figure 2.2: Convection and conduction currents in a saturated pore channel (after[74]).

The alternative formulation to Equation (2.16) is [103]:

$$\mathbf{J} = -Q_v \mathbf{u} - \sigma \nabla \Psi, \tag{2.20}$$

where Q_v is the excess of charge (of the diffuse layer) per unit pore volume (Cm^{-3}). It can be predicted from the hydraulic conductivity K according to $log_{10}Q_v = -3.49 - 0.82 log_{10}K$. The validity of this empirical expression is shown in Figure 2.3 for a broad variety of rocks and sediments [61]. These measurements were performed at various salinities and pH values (pH between 5 and 7 except for the limestones).

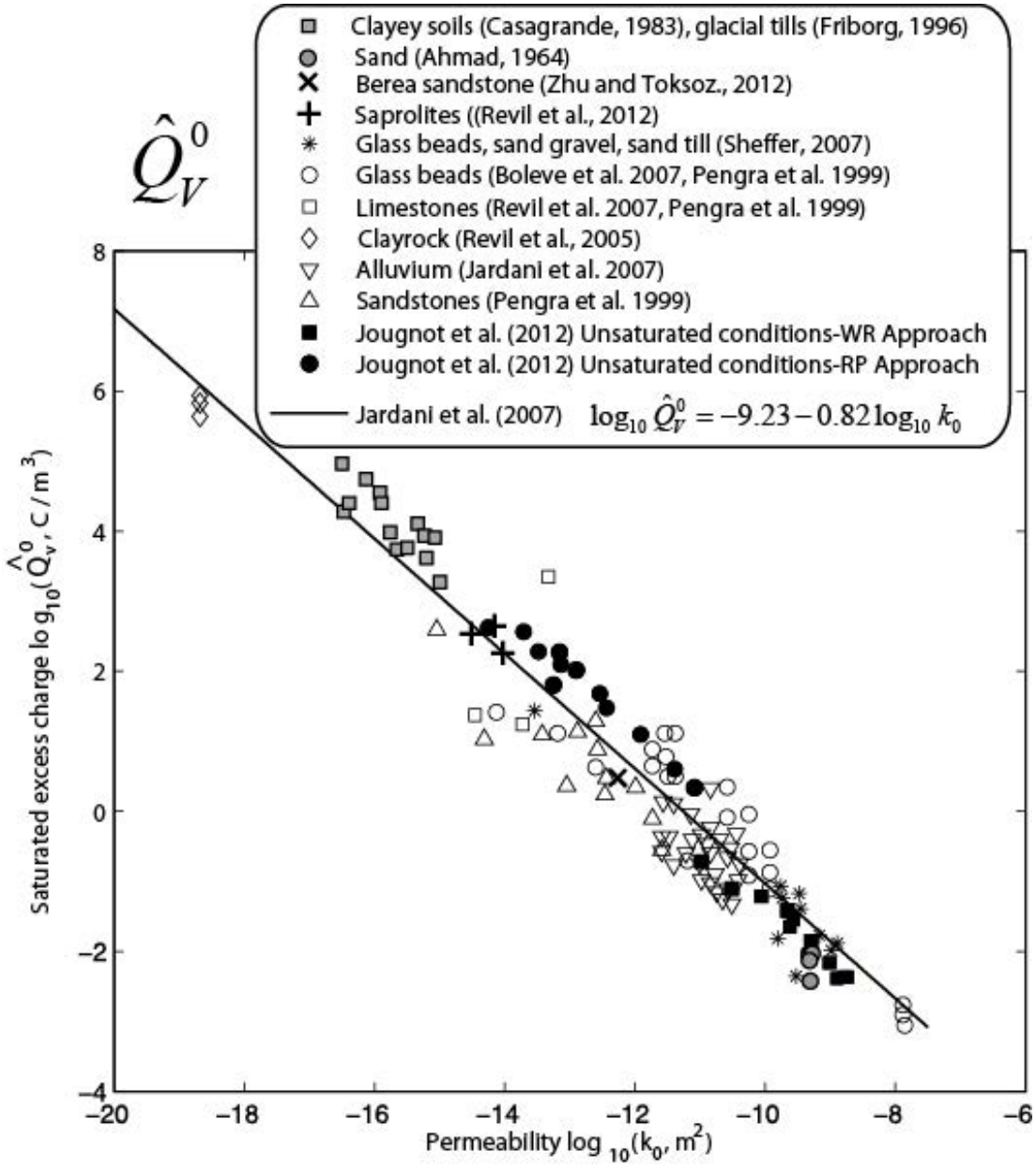

Figure 2.3: Quasi-static charge density Q_v (excess pore charge moveable by the quasi-static pore water flow) versus the hydraulic conductivity K for a broad collection of core samples and porous materials (after [122]).

The constitutive equations (2.15) and (2.20) are combined with two continuity equations for the mass of the pore water and the electrical charge, respectively. The groundwater flow is governed by the diffusion equation [10]:

$$\frac{\partial P}{\partial t} = \nabla \cdot (D \nabla P), \tag{2.21}$$

where $D = \frac{k}{\mu \beta_s}$ denotes the hydraulic diffusivity ($m^2 s^{-1}$) and β_s is the specific storage (Pa^{-1}). It is subjected to the following Dirichlet and Neumann boundary

conditions:

$$P = P_D \quad \text{at } \Gamma_D; \quad -\mathbf{n} \cdot \frac{k}{\mu} \nabla P = 0 \quad \text{at} \quad \Gamma_N. \tag{2.22}$$

The pressure P_D denotes the pressure fixed at the boundary Γ_D and $\mathbf{n}$ is the unit vector normal to the boundary Γ_N.

Combining Equations (2.12) and (2.20) gives a Poisson equation with a source term that depends only on the seepage velocity in the ground:

$$\nabla \cdot (\sigma \nabla \Psi) = \nabla \cdot (Q_v \mathbf{u}). \tag{2.23}$$

Generally, a Neumann-type boundary condition Γ_N is imposed at the insulating air–ground interface while a Dirichlet condition Γ_D is established at the others boundaries:

$$\Psi = 0 \quad \text{at} \quad \Gamma_D; \quad -\mathbf{n}(\sigma \nabla \Psi - Q_v \mathbf{u}) = 0 \quad \text{at } \Gamma_N. \tag{2.24}$$

The physical model described above indicates that the source current density responsible for the occurrence of the self-potential signals is strongly related to the ground water flow pathways [105].

2.4 Electrochemical potential

Electrochemical or diffusion potential is the result of coupling between the chemical gradient (force) and the electric current density (flux). The potential is generated because of the difference in the ion's mobilities in different solutions' concentration [114, 74]. The occurrence of a significant amount of this type of self-potential anomalies is associated with redox half-reactions involving electron donors and electron acceptors and working together with an electronic conductor allowing the long-range transport of electrons. In order to explain qualitatively these self-potential signals, a geobattery model was introduced by Sato and Mooney [111] (Figure 2.4). This model, later revisited by Sivenas and Beales [120], Stoll et al. [128] and Bigalke and Grabner [12], consider both the distribution of the redox potential and the kinetics of the chemical reactions at the surface of the metallic particles. The metallic body participates directly in the two half-cell reactions of the electrochemical cell, which consists of anodic (oxidizing) and cathodic (reducing) reactions. These reactions are located at the bottom and the top of the ore body, respectively Figure 2.4. Stoll et al. [128] and Bigalke and Grabner [12] derived an inert electrode model, which is based on the

classical electrochemical model for metallic electrodes of Bockris and Reddy [16]. This model is based on the non-linear Butler–Volmer equation between the electrical potential and the current density generated at the surface of the metallic body. Once linearized, this equation yields:

$$\mathbf{J}_s = \mathbf{J}_0 \frac{nF}{RT}(-E_H + E_m - \Psi), \tag{2.25}$$

where $\mathbf{J_0}$ is the exchange current density at the surface of the metallic body, n is the number of molar equivalents transferred for the given exchange reaction between the electronic conductor and the surrounding medium, $F = N_e$ is the Faraday constant (9.65×104 C mol^{-1}), R is the gas constant (8.31 J K^{-1} mol^{-1}), T is the temperature (K), E_H is the redox potential (V), and E_m is the redox potential of the metallic conductor (V). The redox potential of the metallic conductor corresponds to the chemical potential of the electrons inside this body. Because the resistivity of the metallic conductor is very small, E_m has approximately a constant value. The current density $\mathbf{J}_s$ equals zero everywhere except at the surface of the iron bar. Mendonca [73] presented an inverse procedure to determine the causative distribution of source currents in the ground, responsible for the observed distribution of the self-potential at the ground surface, where a known electrical conductivity model is assumed.

An alternative model is considering a linear relationship between the source current density and the redox potential [6, 66]:

$$\mathbf{J}_s = -\sigma \nabla E_H. \tag{2.26}$$

For the two models described above, in the quasi-static limit of the Maxwell equations, we have:

$$\frac{1}{R_e}(-E_H + E_m - \Psi) = \nabla \cdot \mathbf{J}_s, \tag{2.27}$$

$$-\nabla \cdot (\sigma \nabla E_H) = \nabla \cdot \mathbf{J}_s, \tag{2.28}$$

where $R_e = RT/(g\boldsymbol{J}_0 nF)$ is the electrode resistance (Ω) in the inert electrode model and g the specific surface area of the surface of the metallic body.

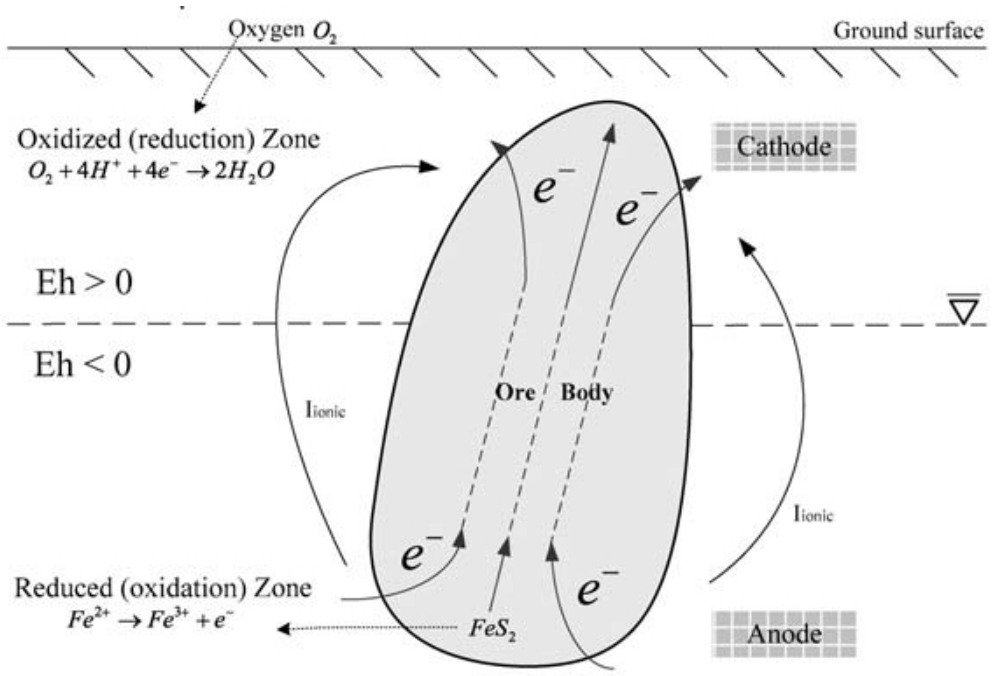

Figure 2.4: The Sato and Mooney (1960) geobattery model whereby the redox gradient is attributed to the gradient of dissolved oxygen in groundwater and the ore body serves as the electron conductor (after [7]).

Sandbox experiments have been widely used to test these conceptual models at an intermediate scale, between the core sample and field scales. In detail the physical and chemical mechanisms that generate such electrical signals have been studied through the insertion of buried metallic bodies centered through the capillary fringe [26, 108]. In this case, the process results in an electrochemical cell, where iron serves as the electron donor at the anode and oxygen gas serves as the terminal electron aceptor at the cathode.

The first step in corroding iron consists in its oxidation to ferrous ions according to $F_e \rightarrow F_e^{+2} + 2e^-$ in the lower part of the metallic body. Then, $F_e(II)$ ions are further oxized to form ferric ions ($F_e(III)$) according to $F_e^{+2} \rightarrow F_e^{+3} + 1e^-$. The formation of a green rust called fougerite, which may occur away from the erosion, is an intermediate step.

Therefore, the elctrons flow in the iron piece providing the source current density $\mathbf{J}_s$. These electrons are used to reduce oxygen according to $1/4O_2 + 1/2H_2O + e^- \rightarrow OH^-$ at the bottom of the iron bar. Consequently the redox reaction for iron is $F_e + 3/4O_2 + 1/2H_2O \rightarrow F_eOOH$.

This sequence of redox reactions is responsable for:

- a perturbation of the distribution of the redox potential in the vicinity of the iron bar: the redox potential can reach hundreds of millivolts close to

the top surface of the tank (because of the effect of the oxygen) and is close to 0 mV or strongly negative around the metallic object as it corrode . This indicates reduced conditions close to the iron object;

- a vertical gradient in the redox potential at distance from the iron bar: the far field contribution can vary mainly with depth and range from hundreds of mV at the top surface of the tank to -50 mV at the bottom. This feature implies an abrupt change from oxidizing to reducing conditions. It is likely that the chemical reactions at the surface of the iron bar consumed the dissolved oxygen of the pore solution and make its diffusion slower;
- a depletion in the concentration of oxygen inside the tank;
- a dipolar anomaly in the vicinity of the metallic object, negative above the metallic pipe and positive below it;
- a basic pH front diffusing inside the tank. The positive or basic pH anomaly developed near the top of the vertical pipe suggests that the reduction processes at the surface of the upper half of the vertical pipe helps to produce OH^- ions in solution above the phreatic surface. As the metallic body corrode, the pH increases above it;
- the formation of a crust on the surface of the bar, probably responsible for an increase of the resistivity at the surface of the iron bar.

2.5 Field procedures

Self-potential measurements are generally perfomed using a pair of non-polarizing electrodes connected, by means of a long wire, to the terminals of a calibrated high impedance voltmeter. The impedance of the voltmeter has to be at least ten times higher than the impedance of the ground between the two electrodes, in order to avoid leakage of current in the voltmeter. A voltmeter with an internal impedance greater than or equal to 10 MΩ would be high enough for most applications. The spacing between two successive measurement-stations depends on the size of the anomalies we expect. At each station, a small hole ($\sim$ 10 cm deep) is dug to improve the electrical contact between the electrode and the ground (Figure 2.5). The approach in self-potential is to establish a map of the distribution of the electrical potential at the ground surface.

Figure 2.5: Typical recording system to monitor the self-potential response. Picture showing the non-polarizing electrodes and the recording multielectrode voltmeter.

In this case, one electrode (reference) is kept fixed at a base station while the other electrode (scanning) is carried to different points. Both prior to and after the measurements, the difference of voltage between the reference electrode and the scanning electrode has to be checked by putting the electrodes one against the other and measuring the difference in electrical potential. The drift of the voltage between the electrodes should be kept as small as possible over time (e.g., ≤ 2 mV per day is an acceptable drift for self-potential mapping) [104]. Values of electrical potential are given with respect to the arbitrary reference station that is conventionally a zero-potential reference point.

When surveys span large areas, measurements are made with respect to a single reference until the maximum amount of wire is deployed. This last survey location then becomes the new reference, and measurements are generally perfomed forming loops (closed profiles or profiles connected at both extremities to othe profiles) in order to evaluate and correct the drift undergone during the acquisition of the data as a result of environmental pertubation (e.g. soil mosture, soil temperature, instrumental errors, etc...). This process requires two corrections of the raw SP data:

- reference correction;
- closure correction (or loop correction).

The reference correction consists in shifting section by section in the direction in which the measurements were acquired while the first section remains unchanged because the first base station is used as a global base station for the entire loop (Figure 2.6).

The closure correction is applied on all the datapoints of the profile to ensure that the sum of the drop potentials along a closed loop is zero, increasing the correction factor from the first to the last point (Figure 2.7). The initial point is the reference of the profile so that no correction is applied to it. The first point (after the reference) is corrected for $1/n^{th}$ of the total drift (where n is the nhumber of data points without counting the reference). The second point is corrected for $2/n^{th}$ of the total drift, etc... until the last point which will be corrected for n/n^{th} of the drift (i.e. the total drift) because it must reach the same value than the reference point [8].

In a completely different, and less frequently used, approach, first the difference of potential between a set of base stations (separated from each other by several hundred meters) is determined. These points of reference are arranged to form a network composed of radial profiles. Thus all the reference points and all the points linked to each of them have been attributed an SP value with respect to one of the base stations [45].

A third strategy, which has almost not employed for practical purposes, is to directly measure the electrical field (not the electrical potential) at a set of station. The electrical field, which is locally tangential to the ground surface, can be measured at a station P by measuring the potential difference in two normal directions. This method is reference free, does not require long wires and is easy to carry out [104].

Another limiting case is called the gradient configuration, where the two electrodes have a constant mutual separation x and they are advanced together along the line of measurements in steps equal to the mutual separation, so that the rear electrode each time occupies the position previously occupied by the front electrode.

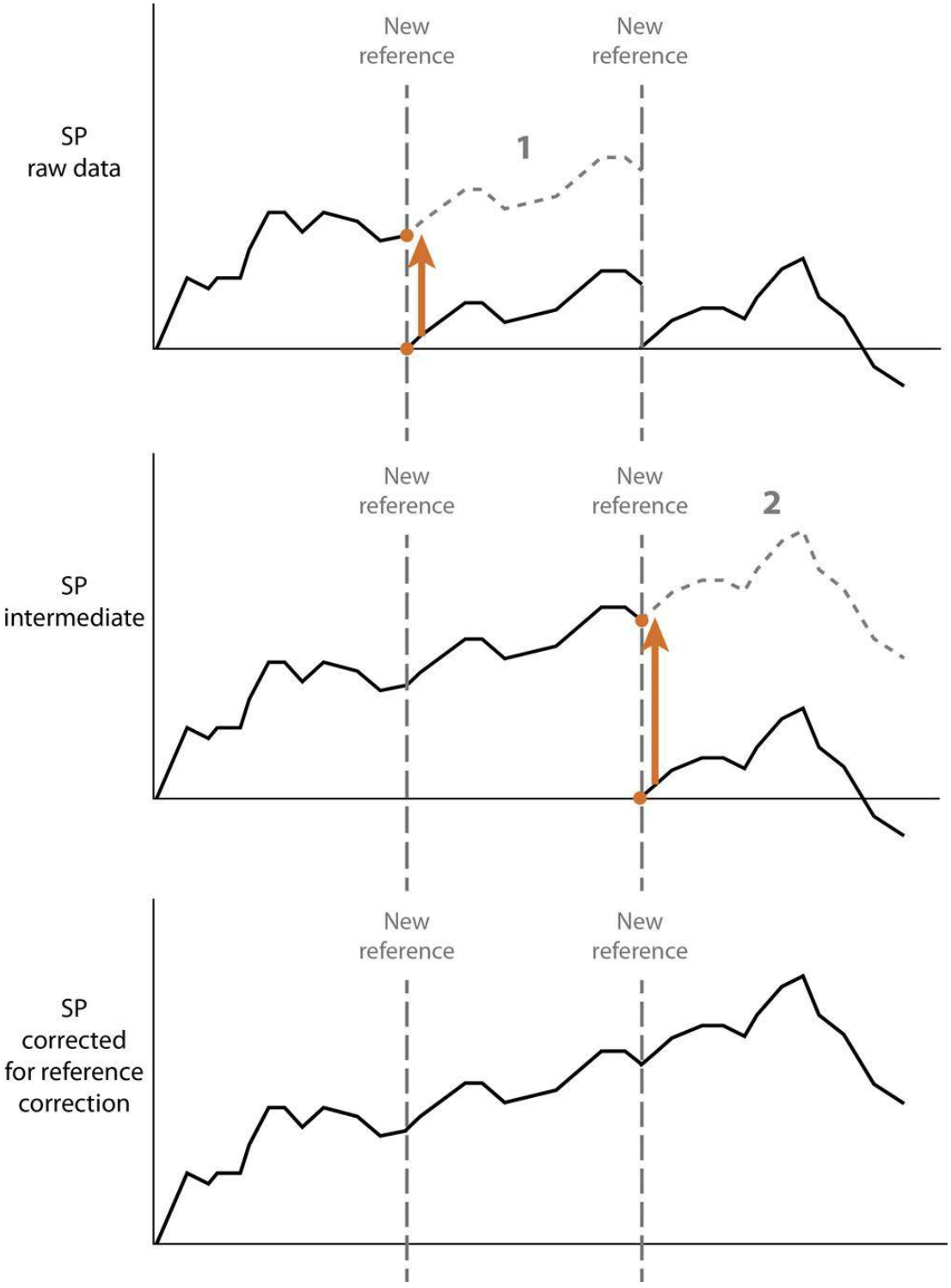

Figure 2.6: Schematic representation of the reference correction on a closed SP-profile. The orange arrows represent the shift of the data, section by section (after [8]).

If the potential difference between the electrodes is $V_2 - V_1$, then $(V_2 - V_1)/x$ is approximately the gradient of the potential or the electric field (mVm^{-1}) at the point midway between the electrodes. Gradient measurements have the advantage that their operational range is unlimited.

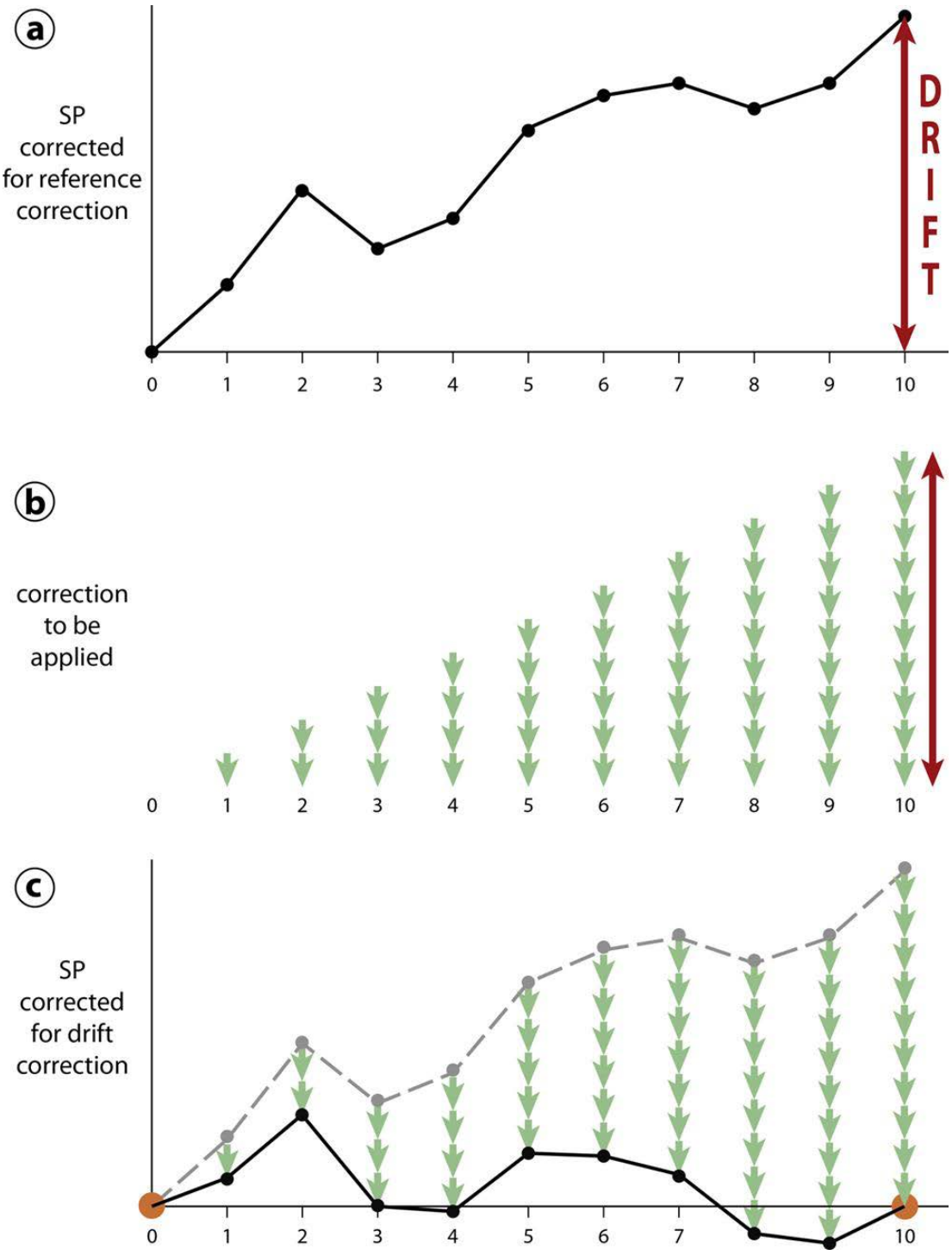

Figure 2.7: Example of the closure correction of SP data in a closed profile composed of 10 datapoints. Point 0 and point 10 are geographically the same (after [8]).

On the other hand, the chances of discovering a weak SP anomaly which varies slowly with distance are greater if the potentials are observed directly (Figure 2.8).

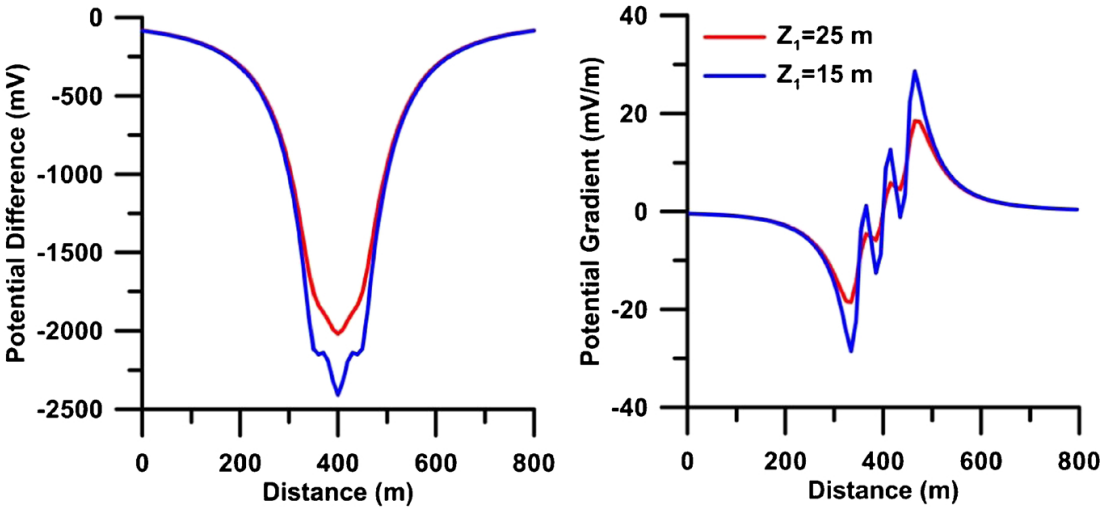

Figure 2.8: Self-potential and self-potential gradient along a profile across bodies with varying depth to the top (z_1) (after [14], modified).

2.6 Sources of noise

As with all geophysical techniques, data errors degrade the ability to interpret the measured signal. Common sources of self-potential measurement error can be associated with the degradation or drift of the measuring electrodes, poor contact between the electrode and soil, topographic effects associated with streaming potentials, photovoltaic potentials, and changes in soil composition, moisture and vegetative cover.

Numerous authors have investigated electrode designs that reduce measurement errors and are stable over long periods of time [91, 94]. Measurement errors on the order of several ($\sim$5) millivolts should be expected with modern surveying equipment, and this can be significantly reduced by installing the electrodes (semi) permanently [92].

Also the influence of cultural noise (e.g. power lines, cathodic protection, grounding systems) can be significant [33], and should be accounted for when surveys are conducted near developed areas. Of course, the level of noise should be considered with respect to the magnitude of the measured signal; large anomalies that register hundreds of millivolts should not be significantly influenced by relatively small errors.

More in details, the most common sources of noise in SP measurements are:

- transient sources: include induction of telluric currents occurring inside the conductive Earth, due to transient current flow in the ionosphere, lightning,

the presence of large cumulus clouds, and induction in the ground associated with power lines, as well as direct current injection associated with cathodic mise-à-la-masse (grounding) used to prevent corrosion of metallic pipes. These signals can be filtered if a fixed dipole is used to record the electrical signals during mapping (or, in the case of telluric noise, a magnetometer to record correlated magnetic signals, see any texbook on the magnetotelluric method);

- spatial noise: associated with strong heterogeneity of the resistivity distribution in the shallow subsurface, due to dry conditions and/or the presence of resistive bodies (like stones) embedded in a more conductive (clayey) matrix, like a fine-grained soil with higher moisture. It can be filtered out if measurements are made with a high spatial density (e.g., five measurements over a square meter at a given station). Generally, Fourier or wavelet-based filters can be used to remove such a noise in a self potential map;

- electrode drift: due to temperature differences between the sensing and the reference electrodes and diurnal variations in environmental temperature. It can be filtered out if raw data are detrended to suppress an assumed linear signal attributed to temperature variations during a short time period. Figure 2.9 shows an example of electrode drift correction performed by [59] on the measured self-potentials (raw data) during a pumping/injection test. This potential measurement was divided into five time intervals denoted I to V. The data were considered to be the sum of the time variation due to the pumping/injection test and its recovery plus a drift. The drift itself was believed to be generated by the variation of the temperature over time and was adjusted by a polynomial of the third order with the coefficients of this polynomial fitted in time intervals I, III, and V. This trend was removed from the raw data, which gives the data shown in Figure 2.9b.

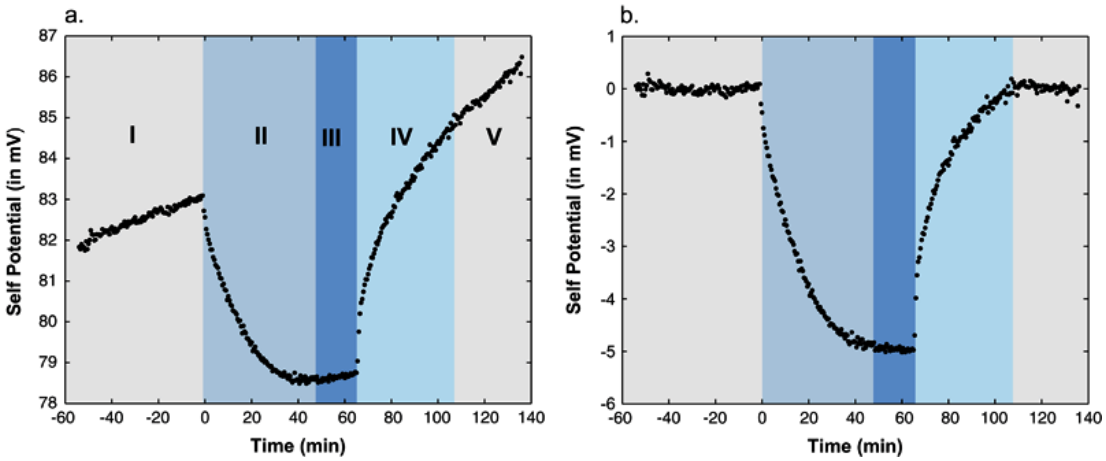

Figure 2.9: Example of self-potential data during a dipole pumping/injection test. (a) Raw data. (b) Detrended data. We can recognize five phases in the pumping test: I corresponds to the data obtained prior to the start of the pumping test; II is the transient phase during pumping; III is the steady-state phase; IV is the rapidly changing portion of the recovery phase; and V corresponds to the slowly changing to steady-state portion(s) of the recovery phase (after [59]).

Chapter 3

Forward problem

The so-called forward solution consists in the derivation of a model that predicts SP measurements on a certain domain, given the conductivity distribution and the physical parameters.

In this Chapter a forward algorithm implemented in Matlab to simulate the occurrence of SP signals is presented. The algorithm was developed to enable the study of self-potential problems for application to engineering, hydrogeological and evironmental investigations.

At the beginning of the Chapter, the elliptic partial differential equation that governs all these problems is illustrated. The Finite Element Method (FEM) is employed because of its flexibility and widespread use for many engineering applications. For the discretization, the Galerkin method is adopted on linear triangular elements.

In the second half of the Chapter, the reliability of the algorithm is tested by comparison of the results with those obtained by other authors on synthetic models. The algorithm was applied to simulate both the electric field resulting from the existence of a leak in the dam and SP signals associated with a pumping test in an unconfined aquifer. In addition, the case of the localization of subsurface cavities is discussed.

3.1 Governing equation

As illustrated in Chapter 2, the forward problem for the self-potential involves solving a Poisson equation. This field equation that governs the electrical response due to a source in a conductive medium is expressed by Equation (2.13) where the volumetric current density can be written as:

$$s = Q_v \nabla \cdot \mathbf{u} + \nabla Q_v \cdot \mathbf{u}, \tag{3.1a}$$

$$s = \nabla \sigma \cdot \nabla E_H + \sigma \nabla^2 E_H, \tag{3.1b}$$

where Equation (3.1a) is valid if self-potential signals are associated with groundwater flow (see Section 2.3) and Equation (3.1b) for electro-redox potentials (see Section 2.4).

Hence, the self-potential forward problem consists of calculating Ψ from Equation (2.13), given s and σ. Using the Green method of integration, the electrical potential distribution is written as [88]:

$$\Psi(P) = \frac{1}{2\pi} \int_\Omega \rho(M) \frac{s(M)}{MP} dV + \frac{1}{2\pi} \int_\Omega \frac{\nabla \rho(M)}{\rho(M)} \cdot \frac{\mathbf{E}(M)}{MP} dV, \tag{3.2}$$

where $x = MP$ is the distance from the source, located at position M, to the self-potential station placed at position P where the electrical signal is measured and Ω represents the conducting subsurface. dV is the infinitesimal volume element of the conductive medium and ρ is the resistivity function that characterizes the inhomogeneous, isotropic subsurface volume Ω. The first term of the right-hand side of Equation (3.2) corresponds to the primary source term while the second term corresponds to secondary sources associated with heterogeneities in the distribution of the electrical resistivity in the medium [63].

It is also possible to rewrite Equation (3.2) as the following convolution product, according to [123, 137]:

$$\Psi(P) = \int_\Omega \mathbf{K}(P, M) \mathbf{J_s}(M) dA, \tag{3.3}$$

where $\mathbf{K}(P, M)$ denotes a linear mapping function referred to as the Kernel (see Chapter 4). The elements of the Kernel are the Green functions connecting the self-potential data at a set of measurement stations P located at the ground surface (possibly in boreholes) and the sources of current density at a set of source points M located in the conducting ground. The Kernel $\mathbf{K}$ depends on the number of measurement stations at the ground surface, the number of discretized elements in which the source current density is going to be determined, and the resistivity distribution. For example, the resistivity distribution can be characterized from a number of geological strata with distinct resistivity values. Generally, the subsurface is discretized. Mixed boundary conditions are used in conjunction with Equation (3.1). A Neumann boundary condition is usually specified at the air-earth interface, such that $\mathbf{n} \cdot \sigma \nabla \Psi = 0$. Whitin the earth, a Dirichlet bound-

ary condition requires that $\Psi \to 0$ as the distance from the sources becomes large ($r \to \infty$).

The calculation of Ψ, given s and σ, is a well-posed forward problem and can be accomplished with a variety of numerical algorithms. A finite element algorithm was developed in Matlab to solve Equation (3.1). There are two significant benefits of this code: (1) the flexibility for incorporating complicated model geometries and (2) the multiphysics approach that allows the physics of the source mechanism to be coupled directly into the problem. The forward algorithm mainly concerns to the determination of the Kernel $\mathbf{K}$ in Equation (3.3). The computation of the Green functions entering $\mathbf{K}$ incorporates the resistivity distribution of the model by solving the Poisson equation numerically for 2M elementary dipoles using the Galerkin method.

The modeling method is a three-step process (Figure 3.1). First, Equation (2.21) is solved with appropriate (Neuman or Dirichlet) boundary conditions for the pressure or groundwater flow. Then, the current source density is calculated on the basis of previously obtained hydraulic and/or redox gradient distribution ($\mathbf{J_s} = Q_v\mathbf{u}$ and/or $\mathbf{J_s} = -\sigma\nabla E_H$). Finally, the SP signals are computed by solving Equation (2.13) with appropriate boundary conditions on the electrical potential. An interactive interface was developed to call all the functions in order to add geometry, mesh, physics settings, boundary conditions, solvers, post-processing and visualizations. During code execution, the procedure first loads the mesh, which is created in Netgen, an adaptive mesh generator able to retain an accurate forward solution without drastically increase the number of elements, a huge problem using standard machines with limited local memories (for further details sourceforge.net/projects/netgen-mesher). Next, the designed algorithm requires a priori information in terms of hydraulic and electrical conductivities. Then, the solver is executed for the hydraulic and the electrical problem. Furthermore, it permits to arbitrarily include equations that may describe a material property, boundary, source or sink term, or even a unique set of partial differential equations.

The main steps are the assembling procedures of the stiffness matrix (Section 3.3), the implementation of the right-hand side (Section 3.4) and the incorporation of the Dirichlet boundary conditions (Section 3.5).

Efficiency of the forward algorithm was tested before solving the inverse problem. In our case, the 2D inversion corresponds to the determination of the two components of the current density for each discretized element of the medium.

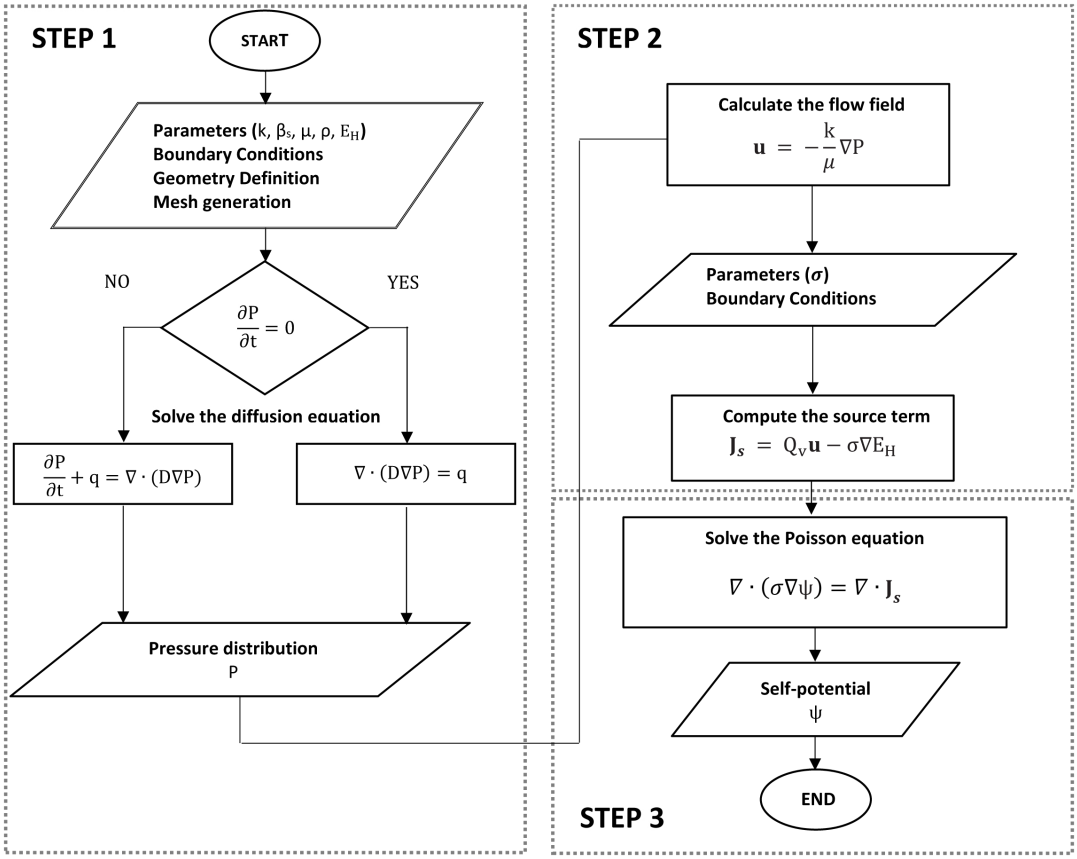

Figure 3.1: Flowchart for the forward modeling of the self-potential data associated with groundwater flow and redox gradient.

3.2 Finite element formulation

The problem under consideration is the one described by the set of Equations (2.15) - (2.24) which is solved by means of the Galerkin formulation of the finite element method. In order to apply the Galerkin approach, the so-called weak variational form of the problem must be derived first. The unknown fields are the pressure P (Pa) associated with the streaming potential and the electrical potential Ψ (V) associated with both the streaming potential and the electro-redox contribution. Multiply Equation (2.21) by an arbitrary weight function, w(x, y), integrate over an arbitrary domain, Ω, whose boundary is Γ:

$$\int_\Omega \beta_s \frac{\partial P}{\partial t} w dxdy \; + \; \int_\Omega \nabla \cdot \left(-\frac{k}{\mu} \nabla P \right) w dxdy \; = \; 0. \tag{3.4}$$

By applying Green theorem [9]:

$$\begin{aligned} \int_\Omega \nabla \cdot \left(-\frac{k}{\mu} \nabla P \right) w \; &= \; + \int_\Omega \frac{k}{\mu} \frac{\partial P}{\partial x} \frac{\partial w}{\partial x} dxdy \; + \; \int_\Omega \frac{k}{\mu} \frac{\partial P}{\partial y} \frac{\partial w}{\partial y} dxdy \\ &\quad - \int_{\partial\Omega} \frac{k}{\mu} \frac{\partial P}{\partial x} w n_x ds \; - \; \int_{\partial\Omega} \frac{k}{\mu} \frac{\partial P}{\partial y} w n_y ds \\ &= \; + \int_\Omega \frac{k}{\mu} \nabla P \nabla w dxdy \; - \; \int_{\partial\Omega} \frac{k}{\mu} \nabla P \boldsymbol{n} w ds. \end{aligned} \tag{3.5}$$

Finally, Equation (3.4) is equivalent to the following variational formulation:

$$\int_\Omega \beta_s \frac{\partial P}{\partial t} w dxdy \; = \; - \int_\Omega \frac{k}{\mu} \nabla P \nabla w dxdy \; + \; \int_\Gamma \frac{k}{\mu} \nabla P \boldsymbol{n} w ds \tag{3.6}$$

The assumed solution of Equation (3.6) for an arbitrary, $n - node$ element is defined by:

$$P^e(x, y) \; = \; \sum_{j=1}^{n} P_j^e \varphi_j^e, \tag{3.7}$$

where P_j^e is the nodal value for $P(x, y)$ at node j for the element, and φ_j^e is the interpolation function at node j within the element. The interpolation functions must satisfy the conditions:

$$\begin{cases} \varphi_j^e(x_k, y_k) \; = \; \delta_{jk} & \text{at all nodes } (j, k) \; = \; 1, 2, ..., n, \\ \sum_{j=1}^{n} \varphi_j^e(x, y) \; = \; 1 & \forall (x, y) \in \Omega. \end{cases}$$

where the Kronecker's delta is defined as:

$$\begin{cases} \delta_{jk} \; = \; 1 & \text{for } j \; = \; k, \\ \delta_{jk} \; = \; 0 & \text{for } j \; \neq \; k. \end{cases}$$

Because the weight functions represent a variation of the primary variable $P(x, y)$ on the nodes, they are equal to $w_i = \varphi_i^e, i = 1, 2, ..., n$. On substituting Equation (3.7) into Equation (3.6), exchanging the order of integration and summation, for stationarity conditions we obtain the generalized matrix equation:

$$\sum_{\mathbf{j=1}}^{\mathbf{n}} \mathbf{A_{ij}^e}\ \mathbf{P_j^e} \ = \ \boldsymbol{Q_j^e} \quad i \ = \ 1, 2, ..., n$$

where:

$$\begin{aligned} \mathbf{A_{ij}^e} \ &= \ \int_\Omega c\left(\frac{\partial \varphi_i^e}{\partial x}\frac{\partial \varphi_j^e}{\partial x} \ + \ \frac{\partial \varphi_i^e}{\partial y}\frac{\partial \varphi_j^e}{\partial y}\right) dxdy, \\ \mathbf{Q_j^e} \ &= \ \int_\Gamma q_n \varphi_j^e ds \ + \ \int_\Omega f \varphi_j^e dxdy, \\ \text{with} \quad c \ &= \ \frac{k}{\mu}, \quad q_n \ = \ \frac{k}{\mu}\nabla\left(\sum_{j=1}^{n} P_i^e \varphi_i^e\right)\mathbf{n} \qquad \text{and} \quad f \ = \ 0. \end{aligned} \tag{3.8}$$

Computing the electrical potential requires the determination of the external source term $s = \nabla \cdot \mathbf{J_s}$ by Equation (3.1), which will be used as source term of Poisson equation after rewriting its variational formulation, following the same method used above for the hydraulic problem:

$$\int_\Omega \sigma \nabla\left(\sum_{j=1}^{n} \Psi_i^e \varphi_i^e\right)\nabla \varphi_j^e dxdy \ = \ \int_\Omega s\varphi_j^e dxdy \ + \ \int_\Gamma \underbrace{\sigma \nabla\left(\sum_{j=1}^{n} \Psi_i^e \varphi_i^e\right)\mathbf{n}}_{=J_n} \varphi_j^e ds, \tag{3.9}$$

$$\sum_{j=1}^{n} \Psi_i^e \int_\Omega \sigma \nabla \varphi_i^e \nabla \varphi_j^e dxdy \ = \ \int_\Omega s\varphi_j^e dxdy \ + \ \int_\Gamma J_n \varphi_j^e ds. \tag{3.10}$$

In terms of matrices, we write:

$$\sum_{\mathbf{j=1}}^{\mathbf{n}} \mathbf{A_{ij}^e \Psi_j^e} \ = \ \boldsymbol{Q_i^e} \quad i \ = \ 1, 2, ..., n$$

where:

$$\begin{aligned} \mathbf{A_{ij}^e} \ &= \ \int_\Omega \sigma\left(\frac{\partial \varphi_i^e}{\partial x}\frac{\partial \varphi_j^e}{\partial x} \ + \ \frac{\partial \varphi_i^e}{\partial y}\frac{\partial \varphi_j^e}{\partial y}\right) dxdy, \\ \mathbf{Q_i^e} \ &= \ \int_\Omega s\varphi_j^e dxdy \ + \ \int_\Gamma J_n \varphi_j^e ds. \end{aligned} \tag{3.11}$$

Equations (3.8) and (3.11) are solved using a Gaussian elimination with partial pivoting. In the first solution, we start from hydraulic boundary conditions and hydraulic conductivity values to obtain the water pressure distribution. In the

second solution, we start from the calculated source, the electrical conductivity and electrical boundary conditions to obtain the self-potential.

3.3 Assembling the stiffness matrix

The local stiffness matrix $\mathbf{A}$ is determined by the coordinates of the vertices of the corresponding element. For a triangular element T let (x_1, y_1), (x_2, y_2) and (x_3, y_3) be the vertices and η_1, η_2 and η_3 the corresponding basis functions [5]:

$$\eta_j(x_k, y_k) \;=\; \delta_{jk} \qquad j,k \;=\; 1,2,3.$$

A moment's reflection reveals:

$$\eta_j(x,y) \;=\; det \begin{pmatrix} 1 & x & y \\ 1 & x_{j+1} & y_{j+1} \\ 1 & x_{j+2} & y_{j+2} \end{pmatrix} / det \begin{pmatrix} 1 & x_j & y_j \\ 1 & x_{j+1} & y_{j+1} \\ 1 & x_{j+2} & y_{j+2} \end{pmatrix}, \tag{3.12}$$

whence:

$$\nabla\eta_j(x,y) \;=\; \frac{1}{2|T|} \begin{pmatrix} y_{j+1} - y_{j+2} \\ x_{j+2} - x_{j+1} \end{pmatrix}.$$

Here, the indices are to be understood modulo 3, and $|T|$ is the area of T, i.e.:

$$2|T| \;=\; det \begin{pmatrix} x_2 - x_1 & x_3 - x_1 \\ y_2 - y_1 & y_3 - y_1 \end{pmatrix}.$$

The resulting entry of the stiffness matrix is:

$$A_{jk} \;=\; \int_T \nabla\eta_j (\nabla\eta_k)^T dx \;=\; \frac{|T|}{(2|T|)^2} \begin{pmatrix} y_{j+1} - y_{j+2}, & x_{j+2} - x_{j+1} \end{pmatrix} \begin{pmatrix} y_{k+1} - y_{k+2} \\ x_{k+2} - x_{k+1} \end{pmatrix},$$

with indices modulo 3. This is written simultaneously for all indices as:

$$\mathbf{A} \;=\; \frac{|T|}{2} \cdot \mathbf{G}\mathbf{G}^T \quad \text{with} \quad G \;=\; \begin{pmatrix} 1 & 1 & 1 \\ x_1 & x_2 & x_3 \\ y_1 & y_2 & y_3 \end{pmatrix}^{-1} \begin{pmatrix} 0 & 0 \\ 1 & 0 \\ 0 & 1 \end{pmatrix}. \tag{3.13}$$

3.4 Assembling the right-hand side

The volume forces are used for assembling the right-hand side [5]. For the electrical problem, using the value of s in Equation (3.1) in the centre of gravity (x_s, y_s) of T the right-hand side is approximated by:

$$\int_T s\eta_j dx \;\approx\; \frac{1}{k_T} det \begin{pmatrix} x_2 - x_1 & x_3 - x_1 \\ y_2 - y_1 & y_3 - y_1 \end{pmatrix} s(x_s, y_s), \tag{3.14}$$

where $k_T = 6$.

Likewise, the Neumann conditions contribute to the right-hand side. The integrals on Γ, in Equations (3.8) and (3.11) are approximated using the value of g (q_n for the hydraulic problem and J_n for the electrical problem, respectively) in the centre (x_M, y_M) of E with length $|E|$ by:

$$\int_E g\eta_j ds \;\approx\; \frac{|T|}{2} g(x_M, y_M), \tag{3.15}$$

where E represents each edge of an element T.

3.5 Incorporating Dirichlet conditions

With a suitable numbering of the nodes, the system of linear equations $\mathbf{AU} = \mathbf{b}$ without incorporating Dirichlet conditions can be written as follows [5]:

$$\begin{pmatrix} \mathbf{A}_{11} & \mathbf{A}_{12} \\ \mathbf{A}_{12}^T & \mathbf{A}_{22} \end{pmatrix} \cdot \begin{pmatrix} \mathbf{U} \\ \mathbf{U}_D \end{pmatrix} \;=\; \begin{pmatrix} \mathbf{b} \\ \mathbf{b}_D \end{pmatrix}, \tag{3.16}$$

where $\mathbf{A}$ is the coefficient matrix and $\mathbf{b}$ indicates the right-hand side resulting from the construction described in the previous sections, $\mathbf{U}$ are the values at the free nodes which are to be determined, $\mathbf{U}_D$ are the values at the nodes which are on the boundary and thus are known a priori. Hence, the first block of equations can be rewritten as:

$$\mathbf{A}_{11} \cdot \mathbf{U} \;=\; \mathbf{b} \;-\; \mathbf{A}_{12} \cdot \mathbf{U}_D. \tag{3.17}$$

In the second block of equations in (3.16) the unknown is $\mathbf{b}_D$ but since it is not of interest to us it is omitted in the calculation.

3.6 Mesh geometry

In choosing mesh geometry it is important to consider the geometry (polygonal, curved, polyhedral etc.) of the domain where the solution is searched, the type of physical problem under consideration, the type of application (structural, geotechnical, geophysical, geological, archaeological etc.), any specific target and the computational time.

Certainly for many applications, a mesh made by triangular elements is the most suitable, due to its capability to model with great accuracy a wide set of domains. The accuracy of the discretization increases, especially for curvilinear domains, reducing the area of the elements and resulting in an non-linear increase of the computational time. In situations of simple domains (e.g. polygons), however, one can use quadrangular (rectangles, trapezoids, prisms etc.) elements having a better accuracy/computational time ratio. We can distinguish three main type of meshes for triangular elements:

- regular, with equivalent elements;
- irregular, made by a number of fixed zones in which elements are equivalent;
- adaptive, in which the mesh is denser near the regions requiring more resolution (as described in Figure 3.2).

The mesh reliability and consequently the accuracy of the forward solver depends primarily on the mesh density and quality. One commonly used quality measure is the ratio between the radius of the largest inscribed circle and the smallest circumscribed circle in the triangles:

$$q = 2\frac{r_{in}}{r_{out}} = \frac{(b + c - a)(c + a - b)(a + b - c)}{abc}, \tag{3.18}$$

where a, b, c are the side lengths. An equilateral triangle has $q = 1$, and a degenerate triangle (zero area) has $q = 0$. As a rule of thumb, if all triangles have $q > 0.5$ the results rated good [93].

For a single measure of uniformity, we use the standard deviation of the ratio of actual sizes (circumradii of triangles) to desired sizes (an element size function $h(x, y)$). That number is normalized by the mean value of the ratio since h only gives relative sizes.

Note that $h(x, y)$ does not have to equal the actual size; it gives the relative distribution over the domain. This avoids an implicit connection with the number of nodes, which the user is not asked to specify. For example, if $h(x, y) = 1 + x$ in

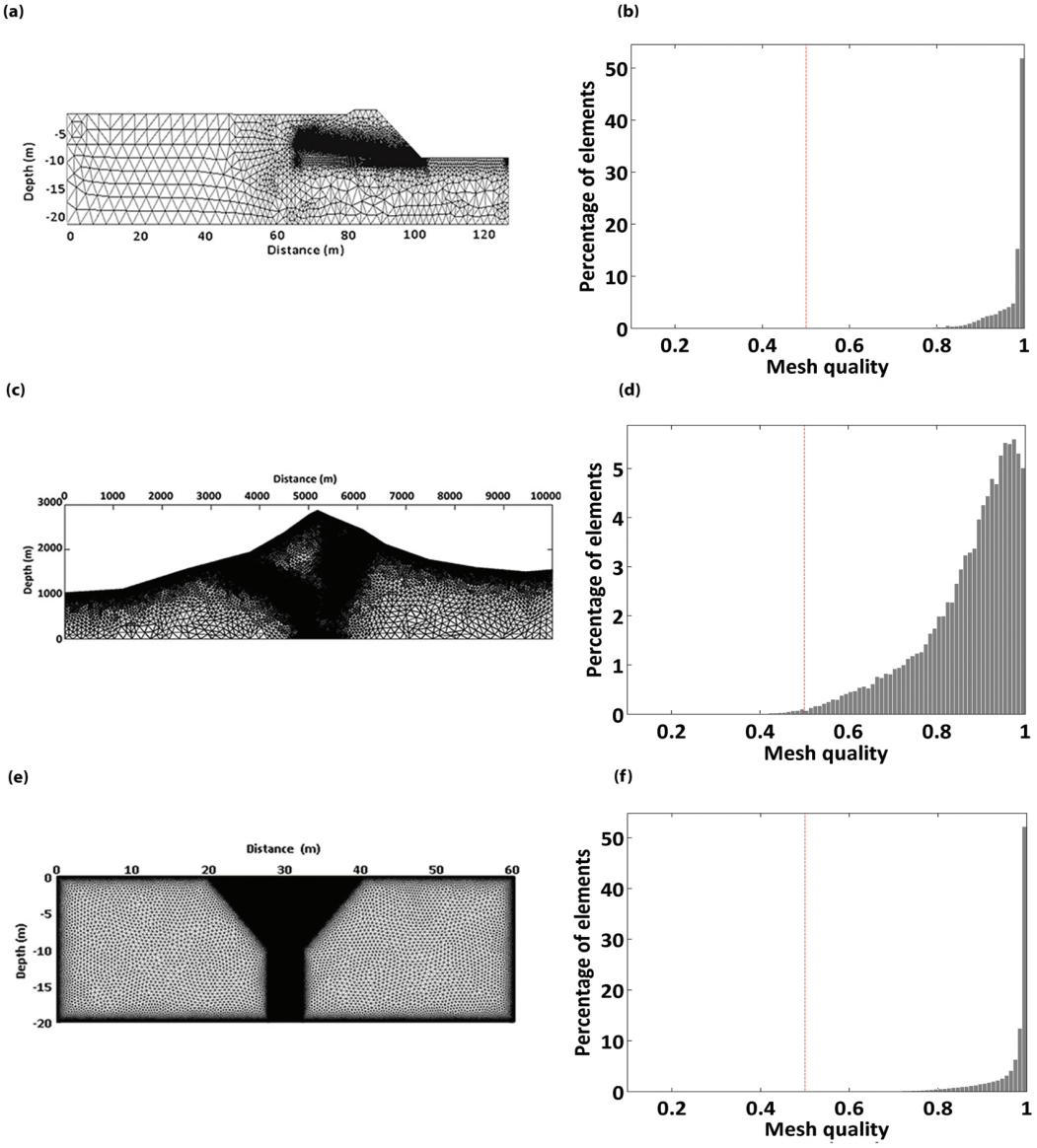

Figure 3.2: Three different 2D adaptive meshes (with their quality histograms) built by Netgen. Triangular meshes are used to discretize the domain for the finite element simulations of the ground water flow problem and the resolution of the semi-coupled SP problem of a dam model with the presence of a leak (a, b), a volcano with permeable conduits (c, d) and a sinkhole (e, f).

the unit square, the edge lengths close to the left boundary ($x = 0$) will be about half the edge lengths close to the right boundary ($x = 1$). This is true regardless of the number of points and the actual element sizes [93].

3.7 Synthetic tests

3.7.1 Pumping test

First, the case of a pumping test in an unconfined aquifer was simulated. The model of the test site and details of the experiment were described by [135]. The electrical and hydraulic parameters were estimated by the authors and illustrated in Figure 3.3 and Table 3.1: the values of electrical conductivity σ were taken from an electrical resistivity tomographic cross-section, while the hydraulic transmissivity T was assumed larger for the first meters from the pumping well than far away and the storativity S was assumed to be constant through the entire aquifer. Taken into account that we used the hydraulic parameters determined by the authors on the basis of the Theis solution [133] and a trial and error procedure to find the best fit between experimental and synthetic data, we considered the aquifer confined in the course of the pumping test (with the initial head at 48 m above the datum).

Hydraulic heads h in the aquifer were calculated analytically using the solution given by [21]. This solution assumes the pumping well is located at the center of a disk with radius R embedded within an infinite matrix. Hydraulic properties are considered uniform within each zone (disk and matrix), but may differ between the two zones such as in this case. For the hydraulic modeling, MAxSym was utilized. In this way, we modeled the pumping phase, keeping fixed the known values of hydraulic parameters. We assessed the consistency of the model by comparing the piezometric levels reconstructed by [135] and our synthetic hydraulic heads (Figure 3.4).

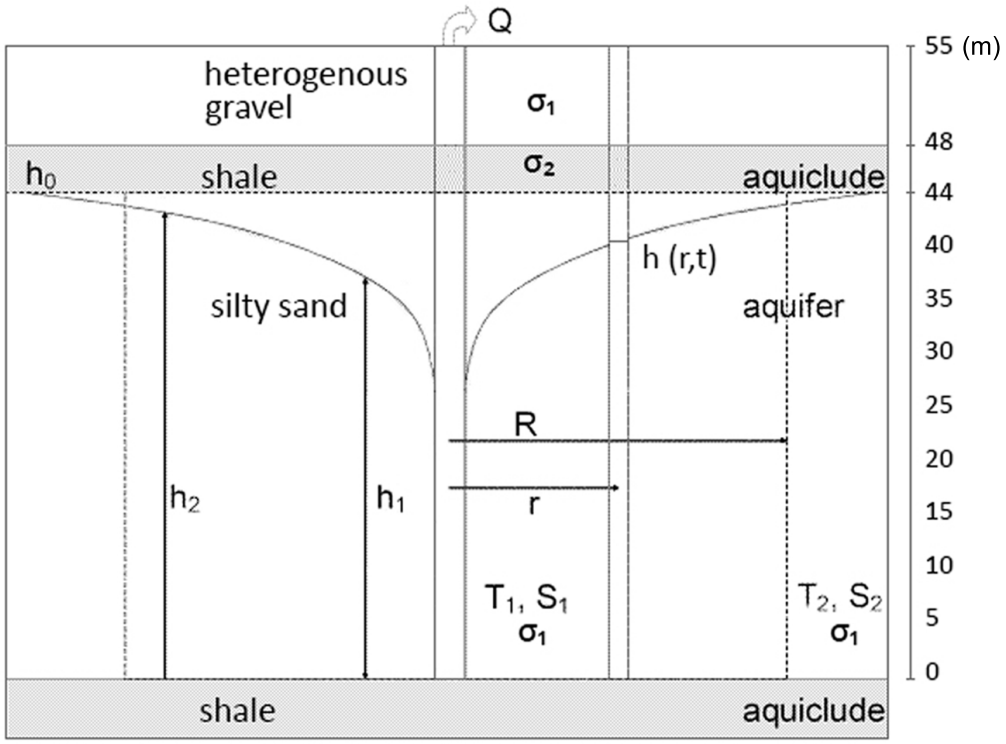

Figure 3.3: Sketch of the pumping test. Petrophysical parameters (T and S are the aquifer transmissivity and storativity, respectively, σ is the electrical conductivity) as well as the initial head distribution $h_o = 48$ m, and the pumping rate $Q = 2.7$ ls^{-1} are involved into the numerical computations.

Table 3.1: Model parameters for the synthetic case study.

Parameters							
T(m^{2}d^{-1})		S(−)		σ(Sm^{-1})		Radius(m)	
T_1	T_2	S_1	S_2	σ_1	σ_2	r	R
50	12	$4.8 \cdot 10^{-4}$	$4.8 \cdot 10^{-4}$	10^{-2}	10^{-1}	r	40

Then, we also determined SP signals on the basis of the calculated distribution of hydraulic head and the known electrical conductivity values. We used the no-flow condition on the ground surface and the condition of zero electrical potential on the other boundaries of the aquifer. The right boundary of the model was located far away from the pumping well in order to ensure that the boundary conditions have no influence on the computation of the SP. The potentials were calculated relative to infinite point in the vicinity of the pumping well at the end of the pumping phase (quasi-state condition), when there is a perfectly linear relationship between the SP signals and the hydraulic heads. As is shown in Figure 3.5, the positive electrical source is centred on the pumping well, while negative sources are located far away under transient regime of the groundwater flow in accordance with the results obtained by the authors.

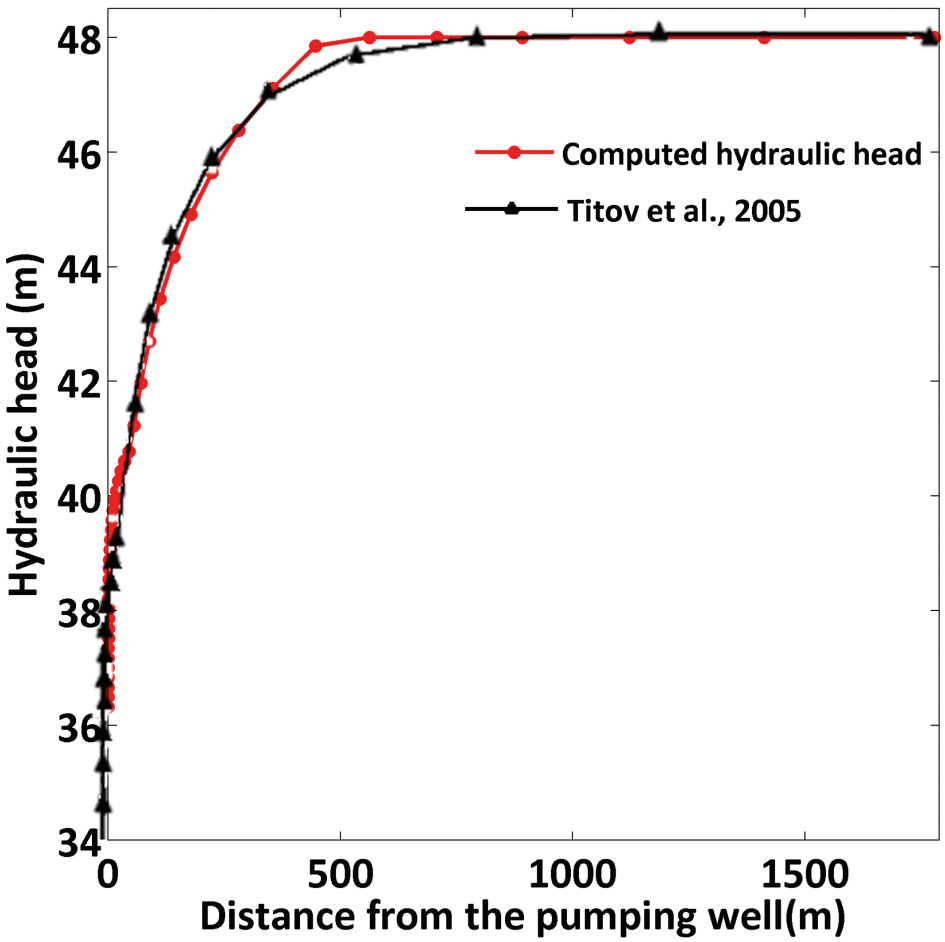

Figure 3.4: Modelled hydraulic head at the end of the pumping phase using MaxSym (red circles) and synthetic data from [135] (black triangles).

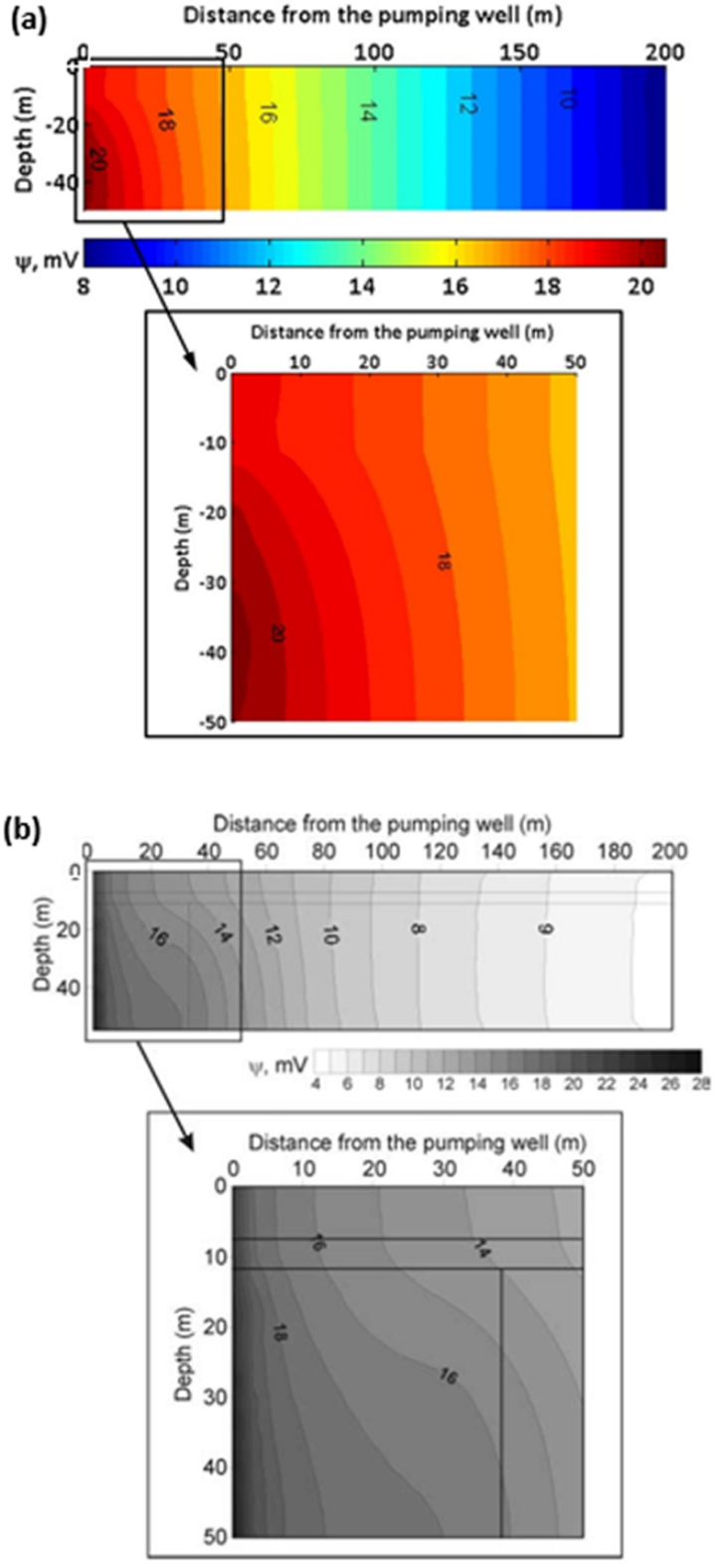

Figure 3.5: Cross-section of the synthetic SP radial distribution around the pumping well (only one side is modeled, because of the symmetry of the problem with an axis of symmetry corresponding to the well). (a) Streaming potentials obtained by adopting the finite element algorithm. (b) Computed SP signal from [135].

3.7.2 Leakages in dams

A second synthetic case is shown in Figure 3.6. We performed the numerical simulation for a synthetic embankment dam reported by [54].

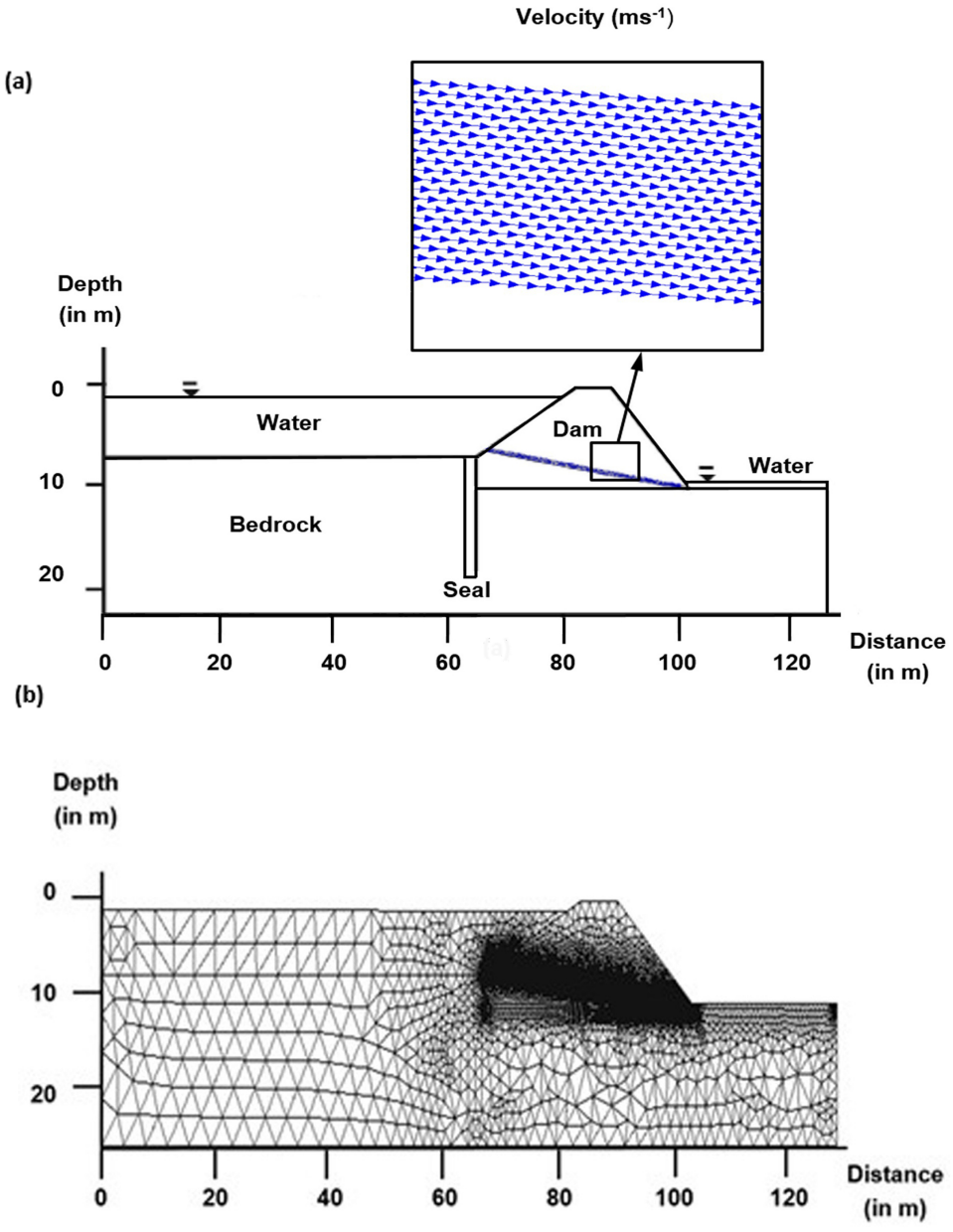

Figure 3.6: Leakage in a dam. (a) 2-D geometry used for the simulation showing a preferential flow pathway crossing the dam and Darcy velocity map obtained by solving the groundwater flow problem. (b) Triangular meshes used to discretize the domain for the finite element simulation.

A leakage was reproduced by adding a permeable pipe located inside the dam core that simulates the existence of a preferential ground water flow pathway with permeability much higher than the permeability of the surrounding area. The material properties, we used to run the numerical model, are provided by the authors (Table 3.2). We chose a high quality triangular mesh denser at the position of the conduit in order to guarantee the accuracy of the forward solver (Figure 3.6b).

Table 3.2: Model parameters for the synthetic case study.

Parameters	$k(\mathrm{m}^2)$	$\sigma(\mathrm{Sm}^{-1})$	$Q_v(\mathrm{Cm}^{-3})$
Water	0	$7 \cdot 10^{-2}$	0
Bedrock	0	$5 \cdot 10^{-4}$	0
Dam	0	$5 \cdot 10^{-4}$	0
Leak	$2 \cdot 10^{-8}$	$7 \cdot 10^{-3}$	$1.2 \cdot 10^{-3}$
Seal	0	$2 \cdot 10^{-3}$	0

The self-potential synthetic data were referenced to a point located at infinity. Boundary conditions were defined as follows: water head pressures were imposed along the lateral boundaries using a Dirichlet condition. At the bottom of the dam and at the ground surface we imposed an insulating boundary condition (($\mathbf{n} \cdot j = 0$) where $\mathbf{n}$ is the unit vector normal to the ground surface). For the electrical problem, the Neumann boundary condition was imposed at the air-ground interface while a Dirichlet boundary condition was applied at the other boundaries. The numerical model was performed for steady-state flow conditions. The groundwater flow due to the hydraulic gradient between the upstream and downstream of the dam is illustrated in Figure 3.6a. The hydraulic gradient and the average velocity in the conduit resulted around of 0.17 and 0.017 ms^{-1}, respectively. The simulated self-potential signals are on the same order of magnitude than those obtained by the authors using a commercial finite element code (COMSOL Multiphysics) (Figure 3.7).

The position of the infiltration inlet is characterized by negative SP signals

while a positive anomaly denotes the outlet of the flow path and is associated to the divergence of the source current density.

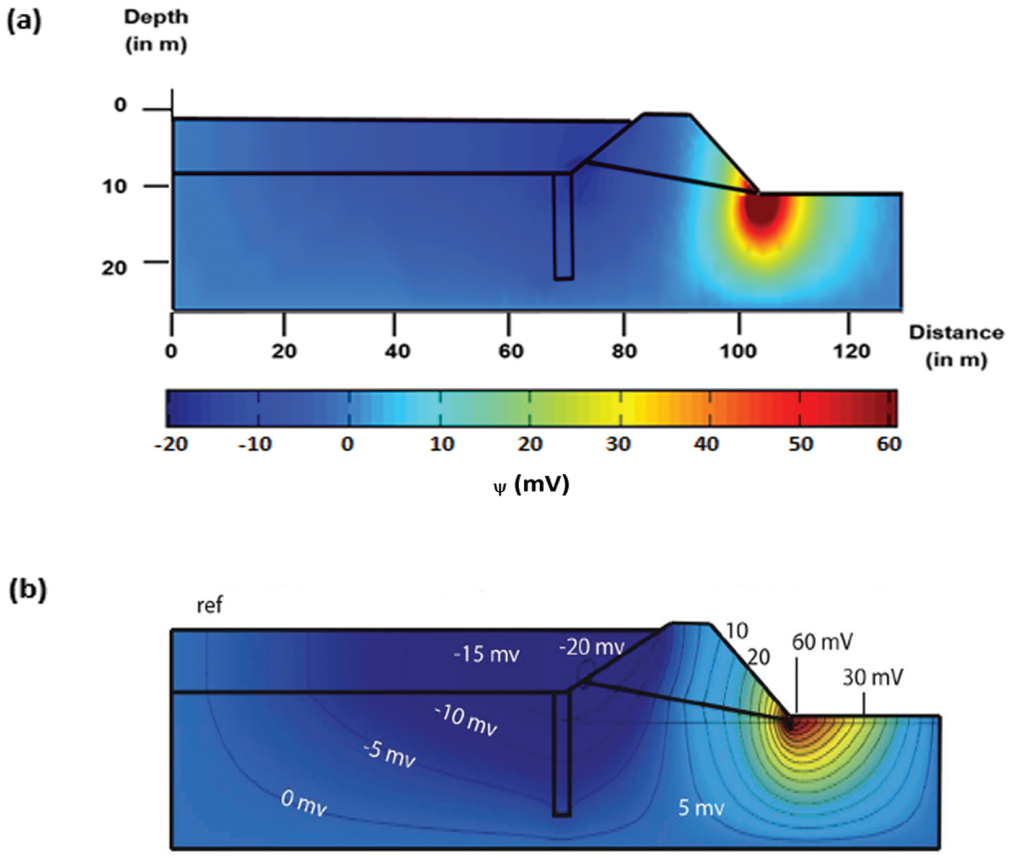

Figure 3.7: Self-potential values from the forward model showing the position of the anomalous flow path through the core of the embankment dam. (a) Simulation of the self-potential signals using the finite element numerical algorithm with reference at infinity. (b) Numerical modeling of the synthetic case reported by [54].

3.7.3 Localization of cavities

Finally, the forward algorithm was used to solve the boundary-value problem for the coupled hydroelectric problem associated with the presence of a cavity

responsible for stress concentrations and the formation of a network of cracks. The proposed field case is that reported by [62]. The geometry of the model is shown in Figure 3.8. The first layer corresponds to a loess cover (from the ground surface to a depth of 2.5 m), the second layer to the clay-with-flint formation (between 2.5 m and 7 m), and the third layer (in which is located the cavity) to the chalk formation. The cavity is surrounded by two vertical conduits. The interfaces between the layers are assumed to be flat.

The distribution of the electrical conductivity and the values of the excess charge density and hydraulic conductivity for each of the three lithological units (loess, clay, chalk and cavity) are reported in Table 3.3. The authors determined the values of these parameters by electrical resistivity tomography and core measurements. In addition, the hydraulic conductivity of the conduits is taken equal to 10^{-3} ms^{-1}, a high value by comparison with the hydraulic conductivity of the background in order to impact on the distribution of groundwater flow.

The side-boundaries Γ_3 and Γ_4 are assumed to be impermeable to force the flow to be vertical. In steady state conditions, the flux at the bottom boundary is equal to the flux of water at the ground surface. For this reason, a fluid pressure of the order of 5 KPa was imposed at the upper boundary Γ_1 and a value of -5 KPa was fixed at the at the lower boundary Γ_2. The amplitude of the source was chosen by trial and error to fit the self-potential data obtained by the authors. This pressure source acts in our model as a "surrogate" force replacing the unknown pressure distribution driving the descent of water from the surface to depth. For the electrical potential, it was considered to be equal to zero at infinity (except at the ground surface where $\mathbf{n} \cdot j = 0$, where $\mathbf{n}$ is the outward unit vector normal to the boundary).

With the characteristics mentioned above, the finite element simulation agrees well with the self-potential data calculated by the authors using the finite-element code Femlab (Figure 3.9).

The numerical simulation pointed out the role of open conduits in electrical charge accumulation near the roof of the cavity and the resistivity contrast between the conduits and the surrounding formation. The self-potential signatures of the conduits are related to the flux of water passing through them. The positive SP anomaly at the conduit outlets indicates clearly the presence of ridges that can channel shallow groundwater flow into the cavity.

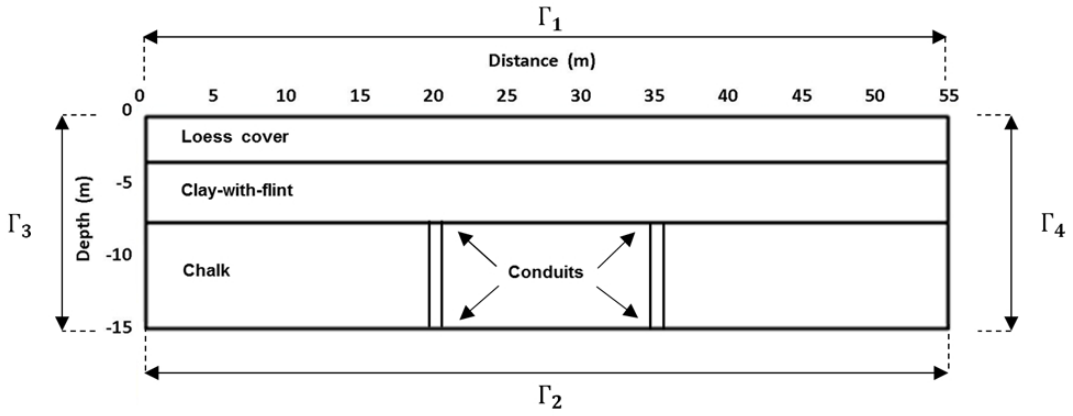

Figure 3.8: Geometrical model used for the finite element calculation. The boundary conditions are discussed in the main text.

Table 3.3: Material properties used in the numerical simulation.

Material	K (ms^{-1})	$\rho(\Omega$ m)	Q_v(Cm^{-3})
Loess	10^{-6}	70	27
Clay-with-flint	10^{-8}	10	$1.2 \cdot 10^3$
Chalk	10^{-10}	100	$5.2 \cdot 10^4$
Conduits	10^{-3}	60	0.1

Instead, the roof of the cavity is characterized by negative charge accumulations that correspond to the entrance of the ground water in the conduits and percolating in the vicinity of the roof of the cavity. Therefore, the conduits are characterized by a negative anomaly close to the inlet with respect to a reference electrode taken at infinite (because located outside the area where the phenomen is present) and a positive one at their outlets [58, 121].

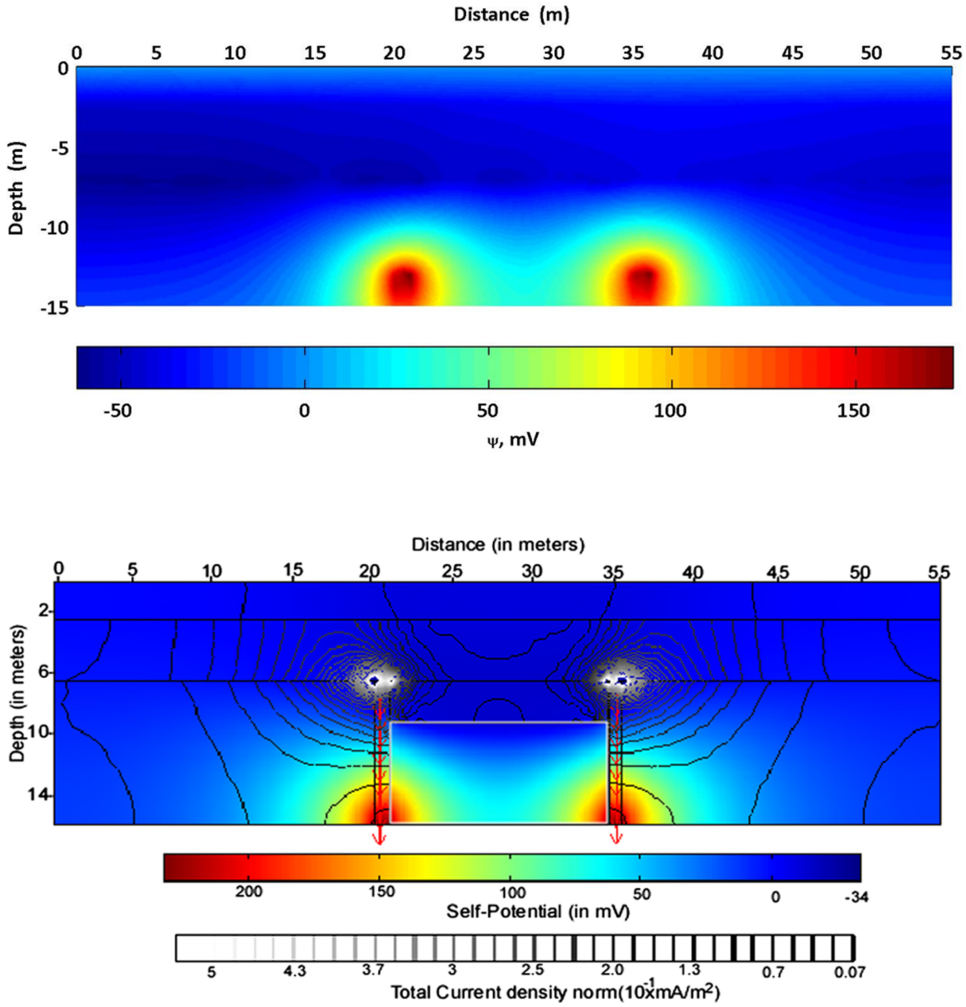

Figure 3.9: Comparison between the self-potential signals calculated by the forward algorithm presented in this thesis (a) and the distribution of the SP determined numerically by [58] using the finite element numerical model Femlab (b).

Chapter 4

Inversion of SP data

One of the most impressive advances made in self-potential interpretation over the past few years has been the inversion of the self-potential signals to locate their source in the ground. This has applications in mapping groundwater flow and redox potential. The inversion of self-potential signals is in itself not new. However, most of the classical methods were based on polarized spheres [143], dipole current lines [87], source and sink pairs [52], or other simple geometries [43, 82, 109]. Such types of methods have also been used to interpret other potential field problems in magnetism and in gravity. Despite the fact that these methods are useful, little information is gained about the source itself, and the physics of the primary flow problem [119] is sometimes missed.

In general, the scope of a geophysical inverse problem is to find an earth model described by a set of physical parameters that is consistent with the observational data. The inverse techniques usually involve the optimization of a certain objective function (e.g the misfit function between predicted and observed data) in order to obtain a good approximation to the desired unknown solution. In particular, the self-potential inversion problem is known to be highly ill-posed with a fundamentally non-unique solution, which is compounded by the limited set of available measurements contaminated by various form of noise. This dilemma is common to nearly all geophysical inverse problems and is solved imposing additional constraints or a priori information to reduce the space of the solution. Regularization is, thus needed, even if there is a large ambiguity in its choice [112]. The purpose of numerical regularization theory is to provide efficient stable methods for including proper side constraints that lead to useful stabilized solutions, and to ensure the choice of the optimal weight given to these side constraints such that the model gives the best fit to the data [50]. We present the deterministic and local approach, which consists of inverting for the source cur-

rent density distribution using the modified singular value decomposition and the linear formulation of the forward problem. This work focuses on a large-scale iterative least-squares QR factorization (LSQR) algorithm for computing solutions to the Tikhonov regularization problem [134]. The method adopted for choosing the regularization parameter is the generalized cross-validation (GCV).

4.1 Methodology

The data and the model parameter vectors are represented respectively by N self-potential observations ψ_i and M elements in which the source current density **Js** is determined (2M represents the number of elementary current sources to consider with one horizontal component and one vertical component):

$$\mathbf{y} = [\psi_1, \psi_2, \psi_3, \ldots, \psi_N]^T, \tag{4.1}$$

$$\mathbf{x} = [\mathbf{J_s^x}, \mathbf{J_s^z}]^T. \tag{4.2}$$

The data and model parameters are related by a linear operator to obtain:

$$\mathbf{y} = \mathbf{K}\mathbf{x}, \tag{4.3}$$

where $\mathbf{K} = (\mathbf{K_{ij}^x}, \mathbf{K_{ij}^z})$ is the $N \times 2M$ Kernel matrix corresponding to the self-potential, which can be measured by each component of the sources coordinates **x**. In our case, the potential at any station P is given by a convolution product between the Kernel **K** and the source current density at each source point (Equation (3.3)). Each element of **K** is a Green function:

$$\mathbf{K} = \begin{bmatrix} K_{11}^x & K_{11}^z & \ldots & K_{1M}^x & K_{1M}^z \\ \vdots & \vdots & \ddots & \vdots & \vdots \\ K_{N1}^x & K_{N1}^z & \ldots & K_{NM}^x & K_{NM}^z \end{bmatrix} \tag{4.4}$$

This matrix depends only on the number of observation stations N, the number of elementary sources M, the distribution of the electrical resistivity and the boundary conditions for the electrical potential or the total current density. When computing the elements of **K**, we consider that the electrical potential is determined relatively to a reference electrode located somewhere in the system. By definition, the electrical potential at the reference station is taken equal to zero and this condition should be fulfilled for all the elements of **K** by removing the potential computed at this location from the self-potential distribution deter-

mined over the field. To determine the elements of the Kernel, we consider that each elementary cell used to discretize the system has a uniform electrical resistivity and each elementary current density can be written as $\mathbf{J_s}(M) = \mathbf{m}\delta(M)$ where $\mathbf{m}$ is the dipole moment, $\delta(\mathbf{r})$ is the Dirac function, and M is the position of the elementary source. For all these elementary dipoles, we solve the Poisson equation.

The matrix $\mathbf{K}$ can be written with simple analytical functions only in the case for which the electrical resistivity is uniform all over an infinite system (or for very simple geometries using for example the image method). In this case, we have [63]:

$$K_{ij}^{x,y} = \frac{1}{4\pi\sigma}\frac{(r_{Pi} - r_{Mj})_{x,y}}{|r_{Pi} - r_{Mj}|^3}, \tag{4.5}$$

with $i \in \{1, ..., N\}$, $j \in \{1, ..., M\}$ and σ is the electrical conductivity of the medium. According to Equation (4.5), it is clear that $K_{ij}^{x,y}$ is large for sources located in the vicinity to the ground surface. In the cases reported in this Thesis, we are dealing with heterogeneous resistivity distributions and the elementary Green functions are computed numerically using the finite element code.

The reconstruction of $\mathbf{J_s}$ requires that the predicted values must agree with the self-potential observations by minimizing the data misfit function defined by:

$$\Phi_d = \|\mathbf{W_d}(\mathbf{Kx} - \mathbf{y})\|_2^2. \tag{4.6}$$

where $\|.\|_2$ denotes the L_2 (Euclidian) norm. It may be desirable to use a weighting matrix $\mathbf{W_d}$ for reducing the impact of data uncertainties or because the elements of the data vector may have different dimensions or ranges of values. It can be given by a square diagonal weighting $(N \times N)$ matrix whose elements are the reciprocal of the standard deviation squared of the data ($\mathbf{W_d} = \{1/\sigma_1^2, \ldots, 1/\sigma_N^2\}$) [61] or it can be formed by the norm of the rows of the matrix $\mathbf{K}$ [144]:

$$\mathbf{W_d} = \mathrm{diag}\left(\sqrt{\sum_j (K_{ij})^2}\right) - \mathrm{diag}(\mathbf{K}\mathbf{K}^T)^{1/2}. \tag{4.7}$$

To reduce the number of solutions that equally reproduce the observed data, also a model objective function must be included:

$$\Phi_m = \|\mathbf{L}(\mathbf{x} - \mathbf{x_0})\|_2^2, \tag{4.8}$$

where $\mathbf{x_0}$ is a prior model while $\mathbf{L}$ is the depth weighting matrix for the model parameters. In the general case, it is identified by the diagonal integrated sensitivity

matrix [144]:

$$\mathbf{L} = \text{diag}\left(\sqrt{\sum_i (K_{ij})^2}\right) = \text{diag}(\mathbf{K}^T\mathbf{K})^{1/2}. \tag{4.9}$$

In other words, it is formed by the norms of the columns of the matrix $\mathbf{K}$.

Alternatively, the lack of depth resolution might be reduced somewhat by introducing a priori information in the form of a depth weighting function. One function could be:

$$L(z) = (h + |z|)^{-\beta/2}, \tag{4.10}$$

where h is the height of data points and the parameter β is referred to Structural Index or Attenuation Rate. The β exponent plays a critical role to correctly estimate the depth to the causative body, because it measures the field decay of the source. Following Euler's theory, different geometric types of sources give rise to different decays of their field, characterized by the quantity β which is given by Table 4.1 according to [65] and [15]. To this end, Cella and Fedi [27] proved that the choice of the exponent of the weighting function is flexible within the allowed interval $0 \leq \beta \leq 3$. In our procedure, the models (see Chapter 5) are obtained by setting $\beta = 3$ and the results confirm that the causative source is recovered at its correct position.

Table 4.1: Structual index of different sources.

	Gravity	Magnetization
Source types	β	β
Point source	2	3
Prism	2	3
Cylinder	1	2
"Sheet" of dipoles	0	1
Contact	-1	0

4.2 Tikhonov regularization

As mentioned above, the best model is one that minimizes the model objective function while fitting the data within an acceptable range of data misfits. For a linear system $\mathbf{y} = \mathbf{Kx}$, where the rank of $\mathbf{K}$ is smaller than the dimension of $\mathbf{x}$, some additional information is needed to find a satisfactory solution because infinitely many solutions exist if there is one at all. In some applications, the acceptable solutions may require the "smoothness" of some function, curve, or surface constraints on m. In this case, the objective function is modified using Tikhonov regularization [134]:

$$\Phi = \|\mathbf{W_d}(\mathbf{Kx} - \mathbf{y})\|_2^2 + \lambda^2 \|\mathbf{L}(\mathbf{x} - \mathbf{x_0})\|_2^2, \tag{4.11}$$

where λ is a regularization parameter under the constraint that $0 < \lambda < \infty$. It controls the weight given to minimization of the side constraint relative to minimization of the residual norm.

The solution of the problem corresponding to the minimum of the global objective function Φ is given by [51]:

$$\mathbf{x}^* = [\mathbf{K}^T(\mathbf{W_d}^T\mathbf{W_d})\mathbf{K} + \lambda(\mathbf{L}^T\mathbf{L})]^{-1} \times (\mathbf{K}^T(\mathbf{W_d}^T\mathbf{W_d})\mathbf{y} + \lambda(\mathbf{L}^T\mathbf{L})\mathbf{x_o}). \tag{4.12}$$

Suppose that it is given the *singular value decomposition* (SVD) of $\mathbf{K}$, i.e., $\mathbf{K} = \mathbf{U\Sigma V}^T = \sum_{i=1}^{n} \mathbf{u}_i \sigma_i \mathbf{v}_i^T$ where $\mathbf{U} = (\mathbf{u}_1, ..., \mathbf{u}_n)$ and $\mathbf{V} = (\mathbf{v}_1, ..., \mathbf{v}_n)$ are orthonormal matrices, $\mathbf{U}^T\mathbf{U} = \mathbf{V}^T\mathbf{V} = \mathbf{I_n}$, and $\mathbf{\Sigma} = diag(\sigma_1, ..., \sigma_n)$ has non-negative diagonal elements appearing in non-increasing order such that $\sigma_1 \geq ... \geq \sigma_n \geq 0$. Then, the Tikhonov regularized solution $\mathbf{x}^*$, can be expressed in the standard form as:

$$\mathbf{x}^* = \frac{\mathbf{V}(\mathbf{\Sigma}(\mathbf{U}^T\mathbf{y})) + \lambda^2\mathbf{V}^T\mathbf{x_0}}{\mathbf{\Sigma}^2 + \lambda^2}. \tag{4.13}$$

In absence of a prior model ($\boldsymbol{x_0} = 0$), we obtain:

$$\mathbf{x}^* = \sum_{i=1}^{n} f_i \frac{\mathbf{u}_i^T\mathbf{y}}{\sigma_i}\mathbf{v}_i, \tag{4.14}$$

where $f_i = \sigma_i^2/(\sigma_i^2 + \lambda^2)$ is the Tikhonov filter factor. The numbers σ_i are the *singular values* of $\mathbf{K}$ while the vectors $\mathbf{u_i}$ and $\mathbf{v_i}$ are the left and right singular vectors of $\mathbf{K}$, respectively. The condition number of $\mathbf{K}$ is equal to the ratio σ_1/σ_n.

In connection with discrete ill-posed problems, two characteristic features of

the SVD of $\mathbf{K}$ are very often found.

- The singular values σ_i decay gradually to zero with no particular gap in the spectrum. An increase of the dimensions of $\mathbf{K}$ will increase the number of small singular values.
- The left and right singular vectors $\mathbf{u_i}$ and $\mathbf{v_i}$ tend to have more sign changes in their elements as the index i increases, i.e., as σ_i decreases.

The SVD also gives important insight into another aspect of discrete ill-posed problems, namely the smoothing effect typically associated with a square integrable Kernel. Notice that as σ_i decreases, the singular vectors $\mathbf{u_i}$ and $\mathbf{v_i}$ become more and more oscillatory.

4.3 LSQR method

This work focuses on an efficient implementation of an iterative algorithm developed by [49], who discussed several 'two-level methods' for the solution of the Tikhonov problem. The algorithm is based on the least squares formulation of the Tikhonov problem:

$$\mathbf{x}^* = \text{argmin}\|\hat{\mathbf{K}}\mathbf{x} - \hat{\mathbf{y}}\|_2^2, \tag{4.15}$$

where the "stacked" matrix and vector are:

$$\hat{\mathbf{K}} = \begin{bmatrix} \mathbf{K} \\ \lambda\mathbf{L} \end{bmatrix} \qquad \hat{\mathbf{y}} = \begin{bmatrix} \mathbf{y} \\ 0 \end{bmatrix}$$

The key idea in the work of Hanke and Vogel is a splitting of the solution space $\mathbb{R}^n$ into two subspaces, one of them with a small dimension and with basis vectors chosen such that this subspace represents approximate regularized solutions. Similarly to multi-level methods, the residual is projected into a small dimensional subspace (the coarse grid) in which the problem is solved with a direct method, while the component of the solution in the remaining subspace is computed by an iterative algorithm. The two levels are created by a splitting of the solution space $\mathbb{R}^n$ into two subspaces $\mathcal{V}$ and $\mathcal{W}$ of dimensions n and $n-k$, respectively. To make the algorithm practical one should choose $k \ll n$. Let the columns of the matrix $\boldsymbol{V} \in \mathbb{R}^{n\times k}$ span the subspace $\mathcal{V}$, and let the columns of the matrix $\boldsymbol{W} \in \mathbb{R}^{n\times(n-k)}$ span the subspace $\mathcal{W}$. The solution is obtained in the form:

$$\boldsymbol{x}^* = \mathbf{V}\mathbf{v} + \mathbf{W}\mathbf{w}. \tag{4.16}$$

This problem can be solved efficiently by means of the LSQR algorithm [86]. There are two advantages in this approach: the implementation is more efficient, and the algorithm is numerically more robust because it avoids the use of the normal equations. It is well known that the LSQR algorithm is algebraically identical to conjugate gradient least-squares (CGLS) and to the conjugate gradient (CG) algorithm on the normal equation system. However, LSQR can be considered as treating the least squares problem in a more direct way, and in finite precision LSQR is often capable of achieving more accurate results than CGLS and in particular CG [57].

We want a solution of the form of Equation (4.16) to the least squares system in Equation (4.15). Thus we need to obtain:

$$\begin{bmatrix}\mathbf{v}\\ \mathbf{w}\end{bmatrix} = \text{argmin}\left\|\hat{\mathbf{K}}\begin{bmatrix}\mathbf{V} & \mathbf{W}\end{bmatrix}\begin{bmatrix}\mathbf{v}\\ \mathbf{w}\end{bmatrix} - \hat{\mathbf{y}}\right\|_2^2. \tag{4.17}$$

Introducing the QR factorization:

$$\hat{\mathbf{K}}\mathbf{V} = \mathbf{Q}\hat{\mathbf{R}} = \begin{bmatrix}\mathbf{Y} & \mathbf{Z}\end{bmatrix}\begin{bmatrix}\mathbf{R}\\ \mathbf{0}\end{bmatrix} = \mathbf{Y}\mathbf{R}, \tag{4.18}$$

with $\mathbf{Q} = \begin{bmatrix}\mathbf{Y} & \mathbf{Z}\end{bmatrix}$ orthogonal and $\mathbf{R}$ upper triangular. Then, $\mathbf{Z}^T\hat{\mathbf{K}}\mathbf{V} = 0$ and $\mathbf{R} = \mathbf{Y}^T\hat{\mathbf{K}}\mathbf{V}$, we get:

$$\begin{aligned}
\begin{bmatrix}\mathbf{v}\\ \mathbf{w}\end{bmatrix} &= \text{argmin}\left\|\begin{bmatrix}\mathbf{Y}^T\\ \mathbf{Z}^T\end{bmatrix}\hat{\mathbf{K}}\begin{bmatrix}\mathbf{V} & \mathbf{W}\end{bmatrix}\begin{bmatrix}\mathbf{v}\\ \mathbf{w}\end{bmatrix} - \begin{bmatrix}\mathbf{Y}^T\\ \mathbf{Z}^T\end{bmatrix}\hat{\mathbf{y}}\right\|_2^2\\
&= \text{argmin}\left\|\begin{bmatrix}\mathbf{Y}^T\hat{\mathbf{K}}\mathbf{V} & \mathbf{Y}^T\hat{\mathbf{K}}\mathbf{W}\\ \boldsymbol{Z}^T\hat{\mathbf{K}}\mathbf{V} & \mathbf{Z}^T\hat{\mathbf{K}}\mathbf{W}\end{bmatrix}\begin{bmatrix}\mathbf{v}\\ \mathbf{w}\end{bmatrix} - \begin{bmatrix}\mathbf{Y}^T\hat{\mathbf{y}}\\ \mathbf{Z}^T\hat{\mathbf{y}}\end{bmatrix}\right\|_2^2\\
&= \text{argmin}\left\|\begin{bmatrix}\mathbf{R} & \mathbf{Y}^T\hat{\mathbf{K}}\mathbf{W}\\ \mathbf{0} & \mathbf{Z}^T\hat{\mathbf{K}}\mathbf{W}\end{bmatrix}\begin{bmatrix}\mathbf{v}\\ \mathbf{w}\end{bmatrix} - \begin{bmatrix}\mathbf{Y}^T\hat{\mathbf{y}}\\ \mathbf{Z}^T\hat{\mathbf{y}}\end{bmatrix}\right\|_2^2
\end{aligned}$$

Thus, the Tikhonov solution is found from:

$$\mathbf{w} = \text{argmin}\|\mathbf{Z}^T\hat{\mathbf{K}}\mathbf{W}\mathbf{w} - \mathbf{Z}^T\hat{\mathbf{y}}\|_2^2, \tag{4.19}$$

$$\mathbf{R}\mathbf{v} = \mathbf{Y}^T(\hat{\mathbf{y}} - \hat{\mathbf{K}}\mathbf{W}\mathbf{w}), \tag{4.20}$$

$$\mathbf{x}^* = \mathbf{V}\mathbf{v} + \mathbf{W}\mathbf{w}. \tag{4.21}$$

The QR factors in Equation (4.18) can be computed conveniently by means of Householder transformations.

Defining $\mathbf{p} = \mathbf{W}\mathbf{w}$, we can proceed in cases where $\mathbf{W}$ is not available. Substituting into Equations (4.19-4.21) gives:

$$\mathbf{p} = \text{argmin}\|\mathbf{Z}^T\hat{\mathbf{K}}\mathbf{p} - \mathbf{Z}^T\hat{\mathbf{y}}\|_2^2, \tag{4.22}$$

$$\mathbf{R}\mathbf{v} = \mathbf{Y}^T(\hat{\mathbf{y}} - \hat{\mathbf{K}}\mathbf{p}), \tag{4.23}$$

$$\mathbf{x}^* = \mathbf{V}\mathbf{v} + \mathbf{p}. \tag{4.24}$$

in which the main computation is solving for $\mathbf{p}$. The resulting algorithm is displayed in Figure 4.1, where for completeness all details of the LSQR iterations are included. The Lanczos vectors are denoted by $\bar{\mathbf{u}}_i$ and $\bar{\mathbf{v}}_i$, and the $\bar{\mathbf{w}}_i$ are work vectors [57].

4.4 Generalized cross-validation

The problem of estimation of the regularization parameter λ for linear problems has been investigated by several researchers. A popular technique is the generalized cross-validation (GCV) [46, 140]. The basic idea for GCV is that a good regularized solution should predict missing data values and the choice of regularized parameter should be independent of an orthogonal transformation of the right hand side. The GCV method intends to balance the data error and the regularization error. Numerator and denominator of generalized cross-validation criteria can be regarded as representing the variance of the estimated observation error, and the bias resulting from the regularization term, respectively, for the practicable reason that the singular value decomposition approach was used to compute the matrix $G(\lambda)$. The optimum λ for the GCV method corresponds to the minimum of the following function $G(\lambda)$:

$$G(\lambda) = \frac{\|\mathbf{K}\mathbf{x}^*(\lambda) - \mathbf{y}\|_2^2}{[Trace(\mathbf{I} - \mathbf{A}(\lambda)\mathbf{K})]^2}, \tag{4.25}$$

SUBSPACE PRECONDITIONED LSQR. Computes the Tikhonov regularized solution $\mathbf{x}_\lambda = \text{argmin}_\mathbf{x} \|\widehat{\mathbf{K}}\mathbf{x} - \hat{\mathbf{y}}\|_2$. There is no restriction on the rank of $\mathbf{L}$.

Compute QR factorization $\widehat{\mathbf{K}}\mathbf{V} = [\mathbf{Y}\ \mathbf{Z}] \begin{bmatrix} \mathbf{R} \\ \mathbf{0} \end{bmatrix}$
$\mathbf{d} = \mathbf{Z}^\mathrm{T}\hat{\mathbf{y}}$
$\beta_1 \bar{\mathbf{u}}_1 = \mathbf{d}$ % So that $\|\bar{\mathbf{u}}_1\|_2 = 1$
$\alpha_1 \bar{\mathbf{v}}_1 = \widehat{\mathbf{K}}^\mathrm{T}\mathbf{Z}\bar{\mathbf{u}}_1$ % So that $\|\bar{\mathbf{v}}_1\|_2 = 1$
$\mathbf{w}_1 = \bar{\mathbf{v}}_1$
$\mathbf{p}_0 = \mathbf{0}$
$\bar{\phi}_1 = \beta_1$
$\bar{\rho}_1 = \alpha_1$
$i = 0$
repeat
  $\beta_{i+1}\bar{\mathbf{u}}_{i+1} = \mathbf{Z}^\mathrm{T}\widehat{\mathbf{K}}\bar{\mathbf{v}}_i - \alpha_i \bar{\mathbf{u}}_i$ % So that $\|\bar{\mathbf{u}}_{i+1}\|_2 = 1$
  $\alpha_{i+1}\bar{\mathbf{v}}_{i+1} = \widehat{\mathbf{K}}^\mathrm{T}\mathbf{Z}\bar{\mathbf{u}}_{i+1} - \beta_{i+1}\bar{\mathbf{v}}_i$ % So that $\|\bar{\mathbf{v}}_{i+1}\|_2 = 1$
  $\rho_i = (\bar{\rho}_i^2 + \beta_{i+1}^2)^{1/2}$
  $c_i = \bar{\rho}_i / \rho_i$
  $s_i = \beta_{i+1} / \rho_i$
  $\theta_{i+1} = s_i \alpha_{i+1}$
  $\bar{\rho}_{i+1} = -c_i \alpha_{i+1}$
  $\phi_i = c_i \bar{\phi}_i$
  $\bar{\phi}_{i+1} = s_i \bar{\phi}_i$
  $\mathbf{p}_i = \mathbf{p}_{i-1} + (\phi_i / \rho_i)\overline{\mathbf{w}}_i$
  $\overline{\mathbf{w}}_{i+1} = \bar{\mathbf{v}}_{i+1} - (\theta_{i+1}/\rho_i)\overline{\mathbf{w}}_i$
  $i \leftarrow i + 1$
until $\bar{\phi}_i \alpha_i |c_{i-1}| < \tau$
Solve $\mathbf{R}\mathbf{v} = \mathbf{Y}^\mathrm{T}(\hat{\mathbf{y}} - \widehat{\mathbf{K}}\mathbf{p}_{i-1})$ for $\mathbf{v}$
$\mathbf{x}_\lambda = \mathbf{V}\mathbf{v} + \mathbf{p}_{i-1}$

Figure 4.1: Scheme of the subspace preconditioned LSQR (after [57]).

where $\mathbf{A}(\lambda) = \mathbf{K}\mathbf{W}_d[\mathbf{K}^T(\mathbf{W}_d^T\mathbf{W}_d)\mathbf{K}+\lambda(\mathbf{L}^T\mathbf{L})]^{-1}\mathbf{K}^T\mathbf{W}_d^T$, $\mathbf{I}$ is the identity matrix, $\mathbf{x}^*(\lambda)$ is the minimum of the cost function and "Trace" denotes the trace of the matrix.

Alternatively, the filter factors (Section 4.2) can be used to evaluate the numerator and denominator (for $m \geq n$) of Equation (4.25) by means of a simple expression in the standard form (Equation (4.29)). First, by replacing $\mathbf{K}$ by its SVD (Section 4.2), the regularized least squares system in the equivalent form $(\mathbf{K}^T\mathbf{K} + \lambda^2\mathbf{I}) = \mathbf{K}^T\mathbf{y}$ can be approximated by:

$$(\mathbf{V}\mathbf{\Sigma}^2\mathbf{V}^T + \lambda^2\mathbf{I})\mathbf{x}^* = \mathbf{V}\mathbf{\Sigma}\mathbf{U}^T\mathbf{y}, \tag{4.26}$$

which gives the approximate regularized solution:

$$\mathbf{x}^* = \mathbf{V}(\mathbf{\Sigma}^2 + \lambda^2\mathbf{I})^{-1}\mathbf{\Sigma}\mathbf{U}^T\mathbf{y}. \tag{4.27}$$

For convenience, $\mathbf{s} = (\sigma_1, ..., \sigma_l)^T$ and $\mathbf{t} = (\mathbf{U}^T\mathbf{y})./\mathbf{s}$ are introduced, where ./ is the componentwise division. $.*$ is the componentwise multiplication, and $\mathbf{f} = (f_1, ..., f_l)^T$ with $f_i = \sigma_i^2/(\sigma_i^2 + \lambda^2)$. Then, the approximate regularized solution in Equation (4.18), its norm η and residual norm ρ can be evaluated respectively by:

$$\begin{aligned}
\mathbf{x}^* &= \mathbf{V}(\mathbf{f}. * \mathbf{t}),\\
\eta &= \|\mathbf{x}^*\|_2 = \|\mathbf{f}. * \mathbf{t}\|_2,\\
\rho &= \|\mathbf{y} - \mathbf{K}\mathbf{x}^*\|_2 = \|\mathbf{y} - \mathbf{U}\Sigma(\mathbf{f}. * \mathbf{t})\|_2\\
&= \sqrt{\|(\mathbf{I} - \mathbf{U}\mathbf{U}^T)\mathbf{y}\|_2^2 + \|\mathbf{U}\mathbf{U}^T\mathbf{y} - \mathbf{U}\mathbf{\Sigma}(\mathbf{f}. * \mathbf{t})\|_2^2}\\
&= \sqrt{\|(\mathbf{I} - \mathbf{U}\mathbf{U}^T)\mathbf{y}\|_2^2 + \|\mathbf{U}\mathbf{U}^T\mathbf{y} - \mathbf{U}(\mathbf{f}. * (\mathbf{U}^T\mathbf{y}))\|_2^2}\\
&= \sqrt{\beta_0^2 + \|(1 - f). * \hat{\mathbf{y}}\|_2^2},
\end{aligned} \tag{4.28}$$

where $\hat{\mathbf{y}} = \mathbf{U}^T\mathbf{y}$ and $\beta_0^2 = \|(\mathbf{I}-\mathbf{U}\mathbf{U}^T)\mathbf{y}\|_2^2 = \|\mathbf{y}\|_2^2 - \|\hat{\mathbf{y}}\|_2^2$. Hence, using the above formulae, the GCV function can be rewritten as:

$$G(\lambda) = \frac{\beta_0^2 + \|(\lambda^2/(\sigma_i^2 + \lambda^2)). * \hat{\mathbf{y}}\|_2^2}{(m - n + \sum_{i=1}^{n} \lambda^2/(\sigma_i^2 + \lambda^2))^2}. \tag{4.29}$$

4.5 Proposed algorithm

The algorithm implemented in Matlab models the medium under investigation using a simplex based finite element representation, and images were reconstructed using regularized inverse techniques. It is a two-dimensional code which allows to solve forward and inverse problems for electrical potential equation. It gives also the possibility to couple groundwater equation with electrical potential equation. Simulations can be run in transient and stationary modes and performed on heterogeneous domains with anomalies included, providing low-error inverted models whereas anomalies are well-detected both for shape and position.
To estimate the goodness of the model, the associated Root Mean Square Error (RMSE) is defined:

$$RMSE = \sqrt{\frac{\sum_{i=1}^{N}(\Psi_i^{calc} - \Psi_i^{obs})^2}{N}}. \tag{4.30}$$

When the solution $\mathbf{x}^*$ is obtained, the forward problem is solved together with the RMSE absolute value. Then, when necessary, the model $\mathbf{x}^*$ is updated to compute new SP distribution until the desired RMSE tolerance criterion, depending on the nature of the problem under investigation, is fulfilled (Figure 4.2). However, it is worth to underline that the recover of the shape and the position of the principal anomalies is given higher priority than reconstructing their amplitude.

The algorithm consists of four primary subfolders:

- **Meshing**: contains functions for generating geometry and meshes.
- **Finite Element Formulation**: contains all functions necessary for implementing the finite elements method.
- **Inversion**: contains inversion and regularization functions.
- **Graphical output**: contains post-processing functions which permit to visualize results.

Separating all the functions in different folders depending on their functionality makes the code cleaner and easier to understand and modify.
The main of the algorithm is divided in sections, where the operator can act to change:

- **Creating Geometry and Mesh**: this step is performed by Netgen code. Read a mesh file or Make a new mesh for 2D geometries:

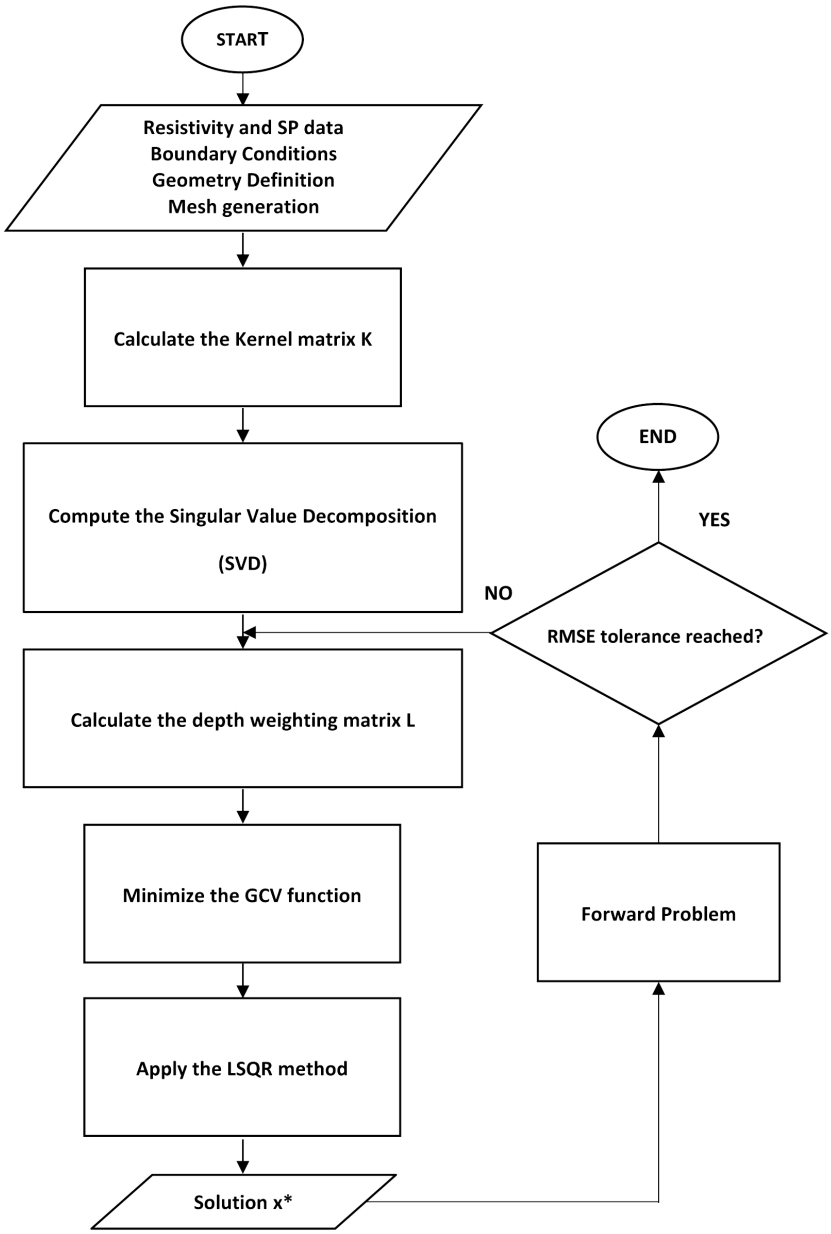

Figure 4.2: Flowchart of the inverse algorithm for searching the best source current density model.

MakeMesh permits to build an adaptive mesh by Netgen.
ReadMesh is able to read a .mat file generated by *MakeMesh* or a .vol file generated by Netgen.

- **Fixing boundary conditions**: the algorithm uses *SetBoundary* for defining boundary conditions.
  Suppose you want to solve your problem and apply non homogeneous Dirichlet boundary conditions on top and bottom boundaries and non homogeneous Neuman boundary conditions on remaining borders.
  You can define your borders as follows :

  bdFlag = SetBoundary (node,elem,'Dirichlet','(y==ymax) | (y==ymin)',...
  'Neumann','(x==xmin) | (x==xmax)')

  where *node* is a 2 column vector containing all nodes coordinates and *elem* is a 3 column vector containing for each triangle the node numbers of the vertices.
  After defining your boundaries you create vectors containing values you want to affect to those boundaries. For example, if we want to impose Dirichlet boundary conditions with values zero, we do as follows :

  function DirichletBoundaryValue = dc(x)
  DirichletBoundaryValue = zeros(size(x,1),1)

  where *dc* denotes the data on the Dirichlet boundary and $y = dc(x)$ returns function values at N discrete points on the Dirichlet boundary. This input data has to be choosen by the user. x has dimension $N \times 2$ and y has dimension $N \times 1$.

- **Assembling Stiffness, Mass matrices, right hand side and Solving linear system of the problem**: Local, global Stiffness and Mass matrices and right-hand side (see Sections 3.3, 3.4, 3.5) are all computed by *FEMstatic* function whether we use stationary simulations. This function returns the solution of the problem and the Stiffness/Mass matrices. Code syntax is used as follows:

  [A,b,u] = FEMstatic(Q,node,elem,Dirichlet,Neumann,S)

  Inputs:

  - *Q: sink source;*
  - *node: node coordinates;*
  - *elem: mesh connectivities;*
  - *Dirichlet, Neumann: boundary edges;*
  - *S: material properties*
    - *in the case of ground water flow, it is the hydraulic conductivity,*
    - *in the case of electrical potential, it is the electrical conductivity;*

  Outputs:

  - *u: solution of the problem;*
  - *A: Stiffness matrix;*
  - *b: right-hand side;*

- **Inverse Problem**: The inverse problem consists to recover the horizontal and vertical components of the source current density. It can be done with the function:

  x=invlsqr(K,L,y,lambda,V,max,stop);

  Inputs:

  - *K: Kernel matrix;*
  - *L: depth weighting matrix;*
  - *y: vector of observed data;*
  - *lambda: regularization parameter;*
  - *V: principal right singular vectors of K;*

  Output:

  - *x: solution of the problem;*

  The function *invlsqr* implements the subspace preconditioned LSQR algorithm to compute (an approximation to) the standard-form Tikhonov solution x for a fixed value of the regularization parameter λ. The preconditioner is based on the subspace defined by the columns of the matrix V

whose columns should be "smooth" and preferably chosen such that a significant component of the exact solution lies in the range of V. The parameter *max* is the maximum allowed number of iterations (default value is maxit = 300). The parameter *stop* is used a stopping criterion for the norm of the least squares residual relative to the norm of the right-hand side (default value is tol = $1e^{-12}$). The output holds all the solution iterates as columns, and the last iterate *x(:,end)* is the best approximation.

Another important step in the inversion process is the choice of the regularization parameter. It is calculated using the function named *RegularizationParameter* adopting the GCV method.
For example, suppose we want to computes the regularization parameter with the GCV method, we do like this:

lambda=RegularizationParameter('GCV','TIKHONOV');

200 logarithmically distributed regularization parameters are generated, and G in Equation (4.29) is plotted for these values. Then the minimizer of the GCV function is computed via *fmin*, using the minimizer of G as initial guess and the filter factors.

Chapter 5

Application to laboratory and field investigations

5.1 Laboratory experiment

A controlled experiment, inspired by the work of Castermant [26], was designed to apply the inversion algorithm presented in this work in an effort to recover the 2D vector distribution of source current throughout a tank for two purposes:

- testing the concept of geobattery at an intermediate scale, between the core sample and field scales;
- localizing the major causative sources of observed electrical disturbances.

An electrochemical system was developed to facilitate corrosion of an iron bar inserted in a Plexiglas cylinder filled with a calibrated sand infiltrated by water. The iron bar served to transmit electrons between the electron donor and oxygen used as the terminal electron acceptor. The self-potential signals were measured at the surface (at different time lapses) and inside the tank on a regular grid at the end of the experiment. Also electrical conductivity distribution within the tank was determined because it is required in the formulation of the kernel matrix used for localization, so as to represent a more realistic scenario in application. This type of experiment is extremely complementary to field measurements, allowing to test the physics of these problems, and providing relative orders of magnitude for the material properties. In this sense, the occurrence of a self-potential dipolar anomaly and the role of the electrical resistivity distribution are the major issues to be addressed.

Preliminary tests were performed to:

- choose an appropriate sand type through a performance comparison among different grain size distributions and permeabilities;
- evaluate approaches to remove electrode effects during self-potential experiment and provide adequate corrections.

5.1.1 Material and methods

The laboratory experiment was conducted in the Plexiglas cylinder adopted by [35] for acquisition of frequency-domain electrical tomography data. The tank having a height of 25 cm and a diameter of 50 cm was filled with sand to depth of 20 cm by taking care to avoid air entrapment (Figure 5.1). The sand was added in uniform, submerged layers to a standing water column. Each newly added layer was sprinkled over the surface of the standing water and allowed to settle out of suspension before it was combed and tamped to remove cavities and air bubbles and mixed uniformly with the underlying sand. The preliminary test was performed over several weeks using river sand, while the main experiment was carried out with the same setup and procedure, where silica sand was introduced within the tank. A metallic body consisting of a rectangular piece of iron with a thickness of 2.5 cm and a height of 11 cm was centered at the phreatic surface. The phreatic surface was maintained constant by adding small amounts of water to the base of the tank through a vertical plastic tube installed prior to filling with sand (Figure 5.2). A hood filter-paper was inserted inside the tank upon the phreatic surface for reducing evaporation.

A total of 49 holes were drilled through a Plexiglas plate every 5 cm in an 7×7 grid and used as a template for electrode placement and manual insertion at five elevations. Because the SP electrodes were not permanently installed throughout the tank, this plate was fitted to the tank to allow for accurate repopulation of the data collection grid for the duration of the study.

Experiment began by first taking measurements at the surface of the tank at the 49 positions indicated in Figure 5.1b and then collecting data along the cross section shown in Figure 5.1a to further explore the nature of the SP signals, once significant surface anomalies were observed to develop. These data were manually collected throughout the tank at 4-cm-depth intervals from 0- to 20-cm depth, resulting in a total of 53 measurements at the end of experiment. These latter were performed with Ag/AgCl non-polarizing electrodes (pellet electrodes with a diameter of 2 mm, a length of 4 mm and a exposed wire of 70 mm) and a calibrated voltmeter (ABEM Terrameter SAS300 resistivity meter with a sensitivity of 1μV and an internal impedance of 10 MΩ). These micro Ag/AgCl electrodes were

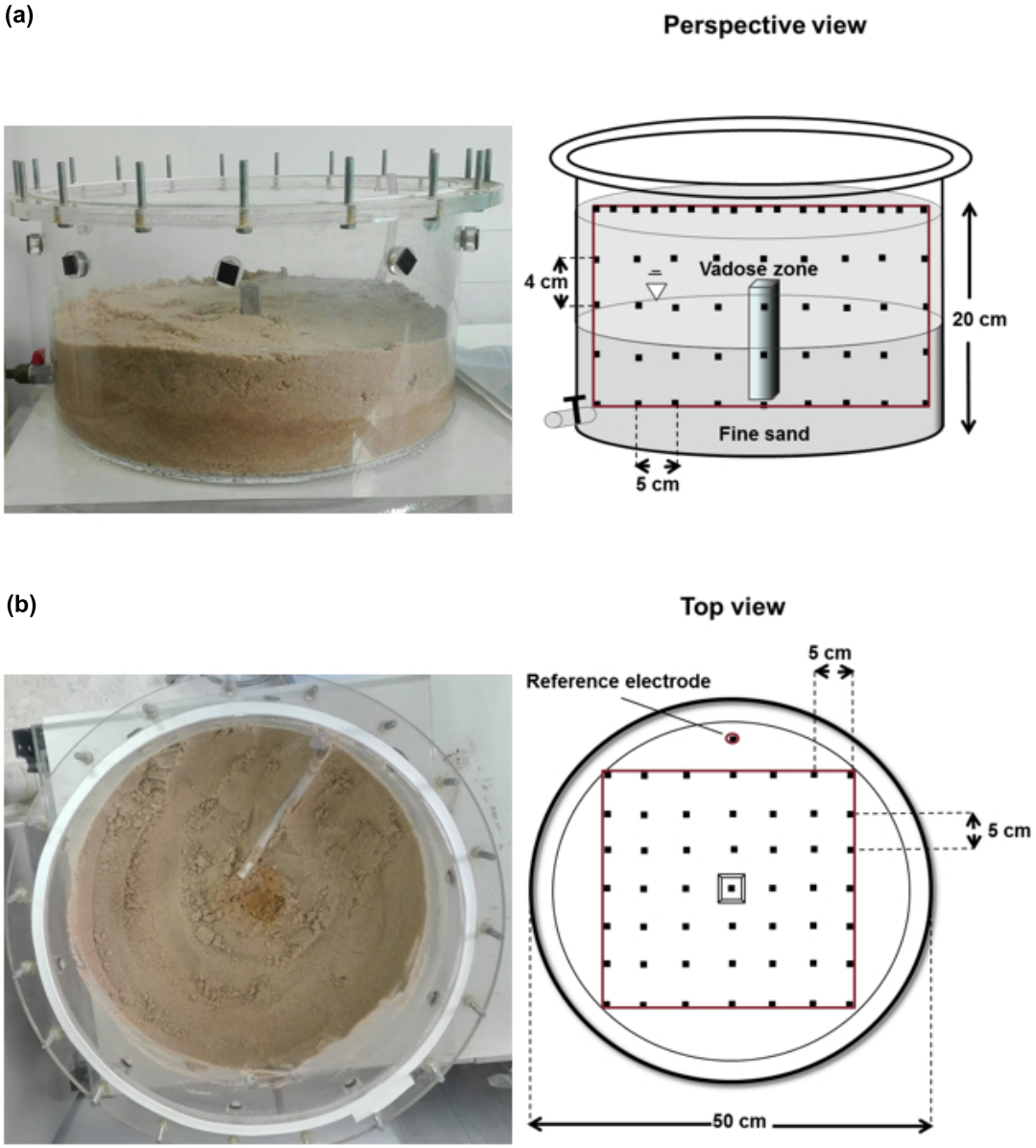

Figure 5.1: Sketch of the experimental setup showing the location of depth SP data points (upper right) and the position of surface data points (lower right) for the actual experiment, the iron bar installed during placement of sand (upper left) and patterns of ferric staining of pore fluid and sand below the phreatic surface at the conclusion of the study (lower left).

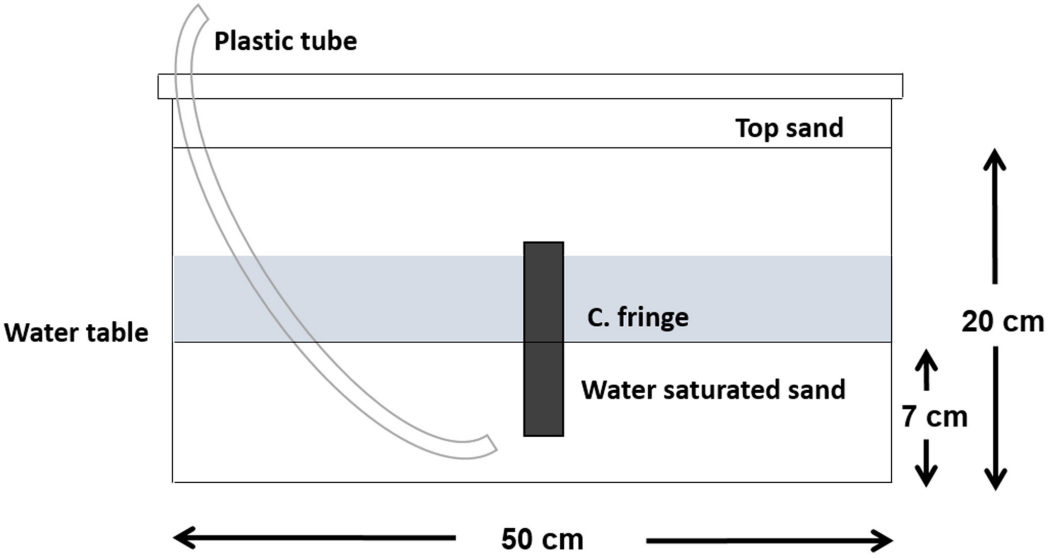

Figure 5.2: Cross section of the cylinder showing the elevation of the established phreatic surface and the metallic body buried in the capillary fringe.

adopted by inserting their wires into a 1-cm-diameter flexible plastic tube (to minimize the invasiveness of the depth measurements) and threading them with banana plugs. To avoid damage and insertion trauma, electrodes were placed into a thin plastic cover and then used to manually probe the sand at depth throughout the tank with minimal introduction of oxygen to the system (Figure 5.3).

Figure 5.3: Photos showing the Ag/AgCl nonpolarizing electrodes and the high-impedance voltmeter during the SP data acquisition along the cross section.

The reference electrode for the self-potential measurements should be ideally placed at infinity, where by definition the electrical potential falls to zero. The reference electrode was collocated at the upper side of the tank to be far from the perturbed zone, approximately 2 cm below the surface of the sand (Figure 5.1b).

Bulk electrical-conductivity distribution in the tank was determined by performing a 2D resistivity tomography using Syscal-Pro resistivimeter (IRIS Instruments) with 10 channels and a dipole-dipole array. The maximum "a" and “n” value used are 5 and 2, respectively. Data were collected utilizing 17 gold electrodes along a profile and 2.5-cm spacing between electrodes (Figure 5.4).

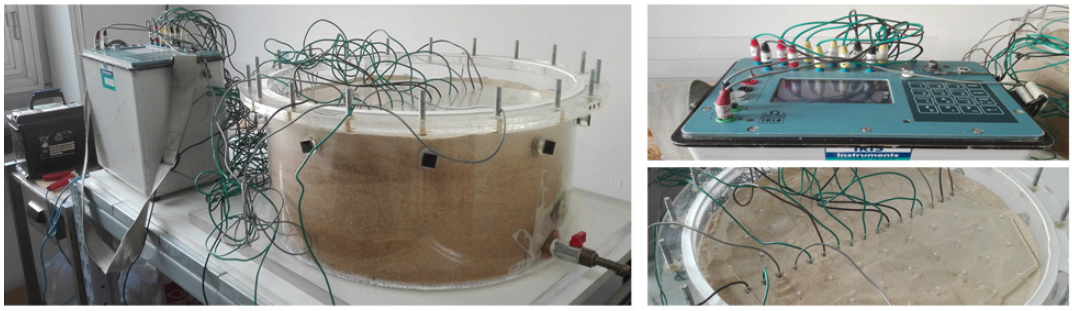

Figure 5.4: Photos showing the gold electrodes and the Syscal-Pro resistivimeter during the resistivity data acquisition along the central profile of the measuring grid.

5.1.2 Preliminary tests

Effects of the sand type

Firstly, two different types of sand were tested in order to choose the best material capable to make the streaming potential contribution of the recorded self-potential signals insignificant. The material properties of the two sands are described in Table 5.1.

The 2D surface SP distribution was monitored for the development of any SP anomalies associated with the metal body buried in the river sand first, then in the silica sand. Self-potential measurements were taken only at 20 stations using a total of 21 electrodes to reduce acquisition time and temporal drift. The reference electrode was placed approximately 2 cm below the surface of the sand in the left upper corner of the measuring grid.

Sequence of 2D SP data (plan-view) collected on the surface of the river sand is shown in Figure 5.5. The time-lapse monitoring of SP data denotes the development of anomalies (yellow-red) due to the rapid movement of water towards the surface. It is worth noting that the use of river sand likely resulted in a faster water upwelling and therefore a stronger pressure gradient. This gradient, in combination with a lower water saturation in the upper region of the tank, resulted in more spatially extensive and larger amplitude SP anomalies compared to experiment conducted with the silica sand (Figures 5.6a and b).

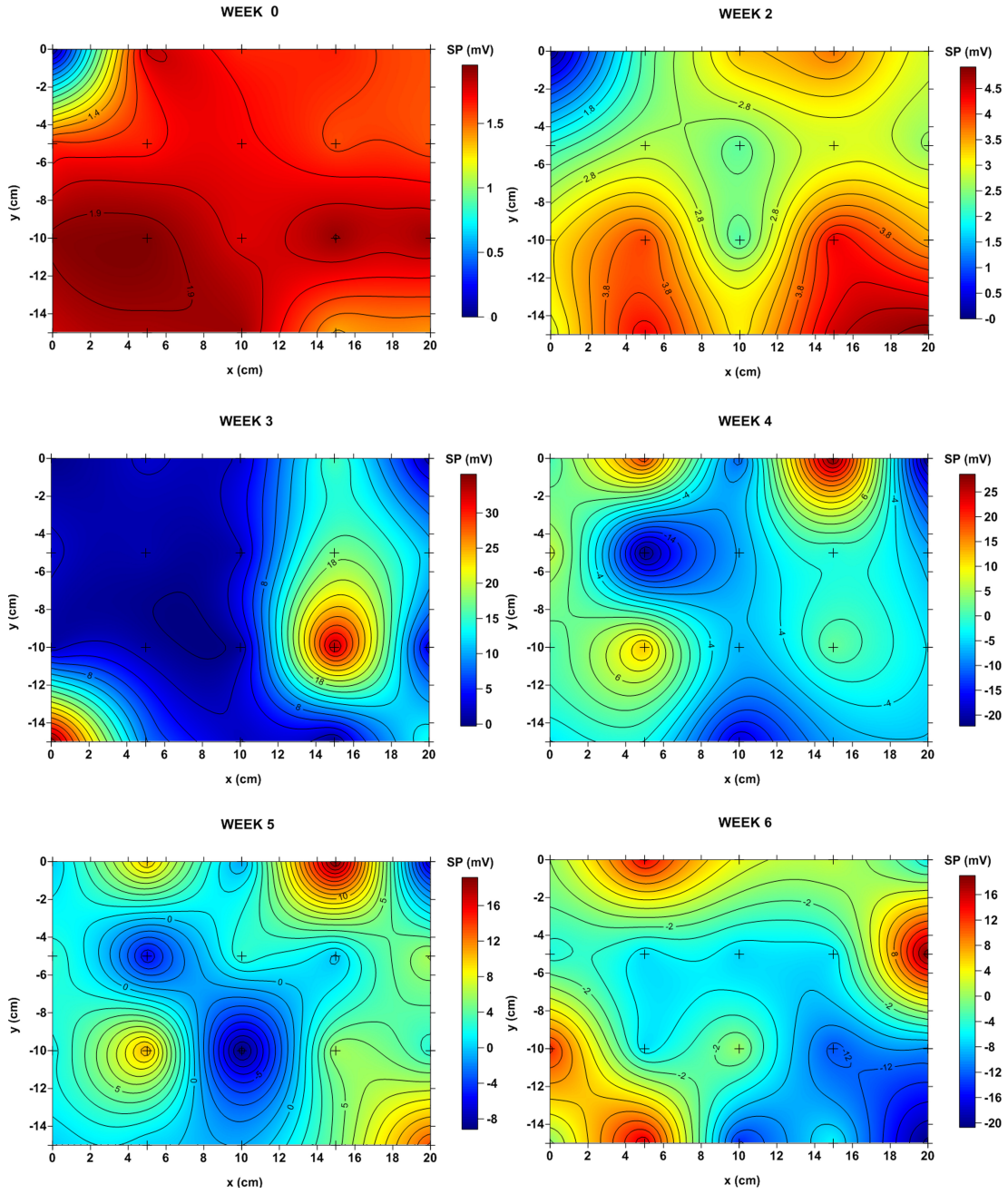

Figure 5.5: Evolution of self-potential data at the surface of the tank in presence of river sand. Black crosses indicate positions of the self-potential stations.

Table 5.1: Properties of the two sands used in the experiment.

Properties	River sand	Silica sand
Physical characteristics		
Unit weight γ (Kgm^{-3})	1600	$1300 \div 2500$
Mohs hardness	6	7
Granulometry (mm)	$0 \div 4$	$0.1 \div 0.63$
Particle shape	rounded	polyhedral
Chemical analysis		
Silica oxide - $S_iO_2(\%)$	79.8	$90 \div 96$
Iron oxide - $Fe_2O_3(\%)$	2.42	0.13
Aluminum oxide - $Al_2O_3(\%)$	3.28	1.35
Calcium oxide - $CaO(\%)$	4.60	–
Magnesium oxide -$MgO(\%)$	2.18	–
Sodium oxide - $Na_2O(\%)$	2	–
Potassium oxide - $K_2O(\%)$	1.96	1.1
pH	7	$7 \div 8$

On the contrary, the finer-grained silica sand and decreased water saturation above the phreatic surface likely caused a higher bulk conductivity and a more spatially compact negative pole due to the E_H gradient across the metallic object. Figure 5.7 shows the initial stages of the generation of this negative SP anomaly located above the vertical pipe. This indicates that the silica sand allowed to reduce the capillarity, avoiding the ascent of water to surface and the development of the electrokinetic SP component. Due to the results obtained, silica sand was adopted for the laboratory campaign, as described in the following section.

Effects of the electrodes

The second purpose of the preliminary study was to provide a quantitative evaluation of electrode effects. Based on their study, Petiau and Dupis [95] found Ag-AgCl electrodes to be among the best non-polarizable electrodes for geophysical applications, given their low noise and short stabilization time, but other works mention important electrode effects. Self-potential data are usually interpreted after some sort of simplistic removal of electrode effects such as removing linear drifts of the electrodes between two points in time when the true SP signals are assumed to be known [71, 131] or by shifting the raw data to zero after a monitored hydrologic event [66].

Against this background, before introducing the metallic object into the tank, monitoring was conducted with two Ag/AgCl electrodes inserted into the silica sand at 49 locations. The calculated SP average value was assumed as back-

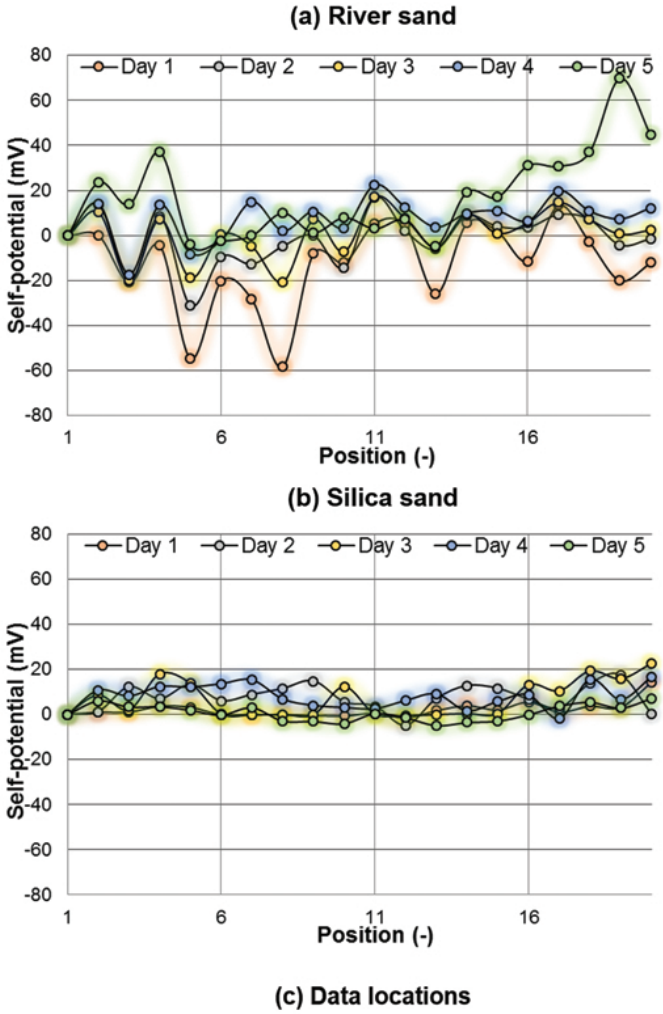

(c) Data locations

Figure 5.6: Comparison between the self-potential profiles at four different times. Raw data collected over 5 days on (a) river sand and (b) silica sand. (c) Configuration of the tank used in the preliminary test with the position of the electrodes.

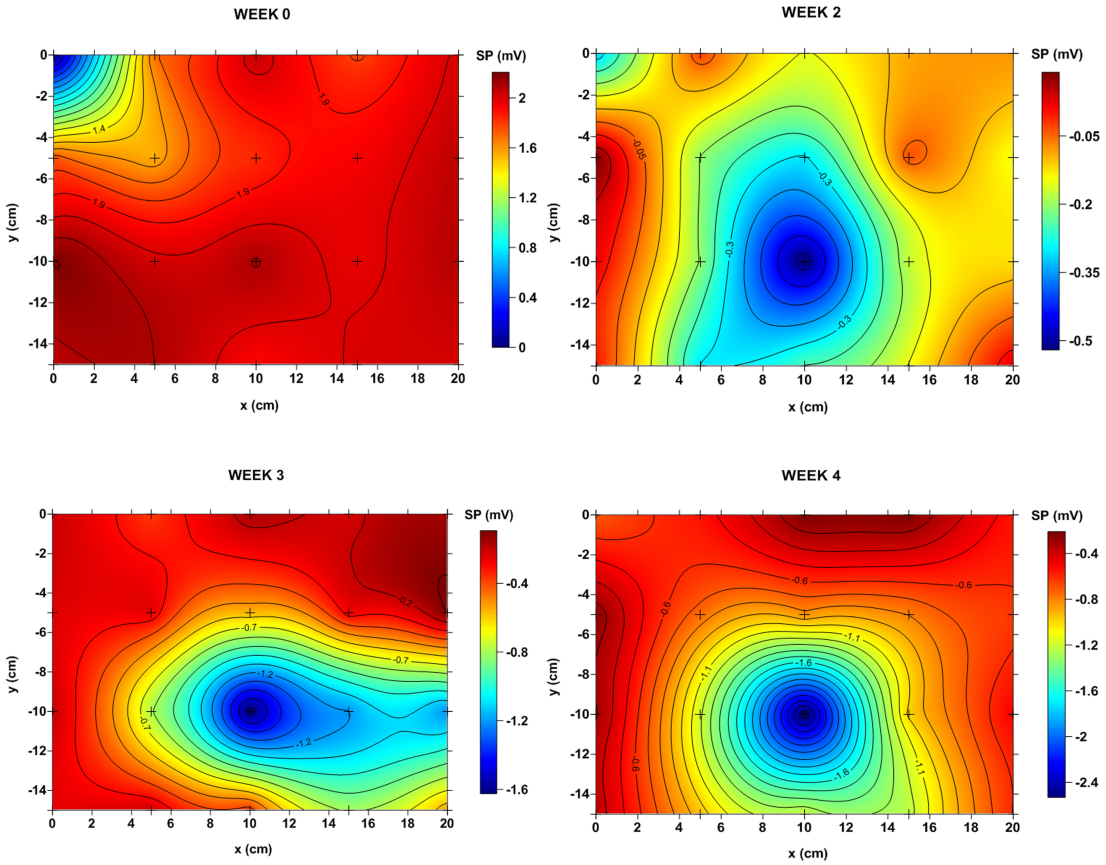

Figure 5.7: Surface self-potential maps after replacing the river sand with the finer particles of the silica sand.

ground noise and subtracted from all the actual SP measurements. In addition, during the actual experiment the electrode drift was checked after each survey and removed from the raw data. The drift was determined by subtracting the SP signal between the reference electrode and a working one recorded at the beginning of the experiment and those measured after the investigation. Then, it was divided by the total number of measurements.

After these steps, the first measurement was subtracted from all the data to reallocate the first data to zero (reference point). An example of the different corrections applied to self- potential data is shown in Figure 5.8. The first electrode is used as a common reference for each profile and over time.

5.1.3 Synthetic example

Before performing the data inversion, to test the efficiency of the inversion algoritm based on LSQR approach, a simple synthetic model was created. It helped to control the inversion algorithm and to ensure accuracy and reliability. In particular it was important to verify if the algorithm was able to reconstruct some amplitude anomalies embedded within a background medium. The proposed model is subdivided in several blocks (9×9 cells). Based on measurements, the spatial distribution of the source current density and the electrical conductivity were assigned as shown, respectively, in Figure 5.9a and Figure 5.9c. Self-potential signals were obtained by solving the forward problem and sampled at the surface of the model (see Figure 5.10). This SP profile was then inverted to retrieve the source current density **Js**. The data were first contaminated by a zero-mean Gaussian noise having a standard deviation of 2 %.

The inverse problem consists, in the first place, in computing the kernel matrix connecting the distribution of the source current density vectors and electric potential data and then optimizing the objective function using LSQR algorithm. The inverse solution is shown in Figure 5.9b. It recovers reasonably well the shape and the position of the principal anomalies as well as their amplitudes.

5.1.4 Data acquisition and inversion

Self-potential measurements were monitored for eight weeks, and self-potential anomalies due to the corrosion of the iron bar were observed during that period at the top surface of the tank. The collected self-potential data were corrected as explained in Section 5.1.2, gridded by kriging with a linear variogram model and contoured using the software Surfer9 (Golden Software, Inc). Figure 5.11

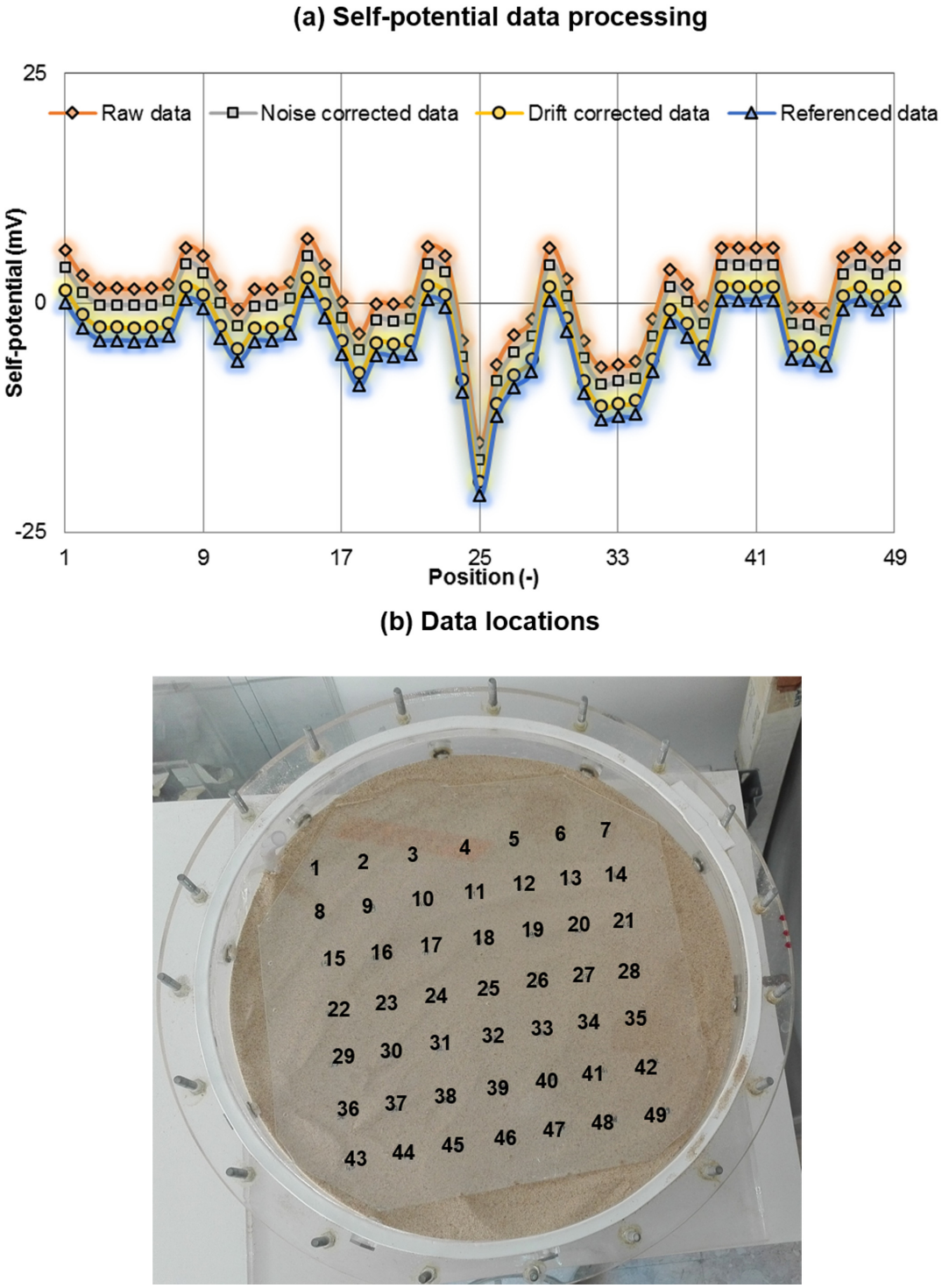

Figure 5.8: Self-potential data processing. (a) Three steps to obtain correction of raw SP data. (b) Configuration of the sandbox used in the preliminary test with the position of the electrodes.

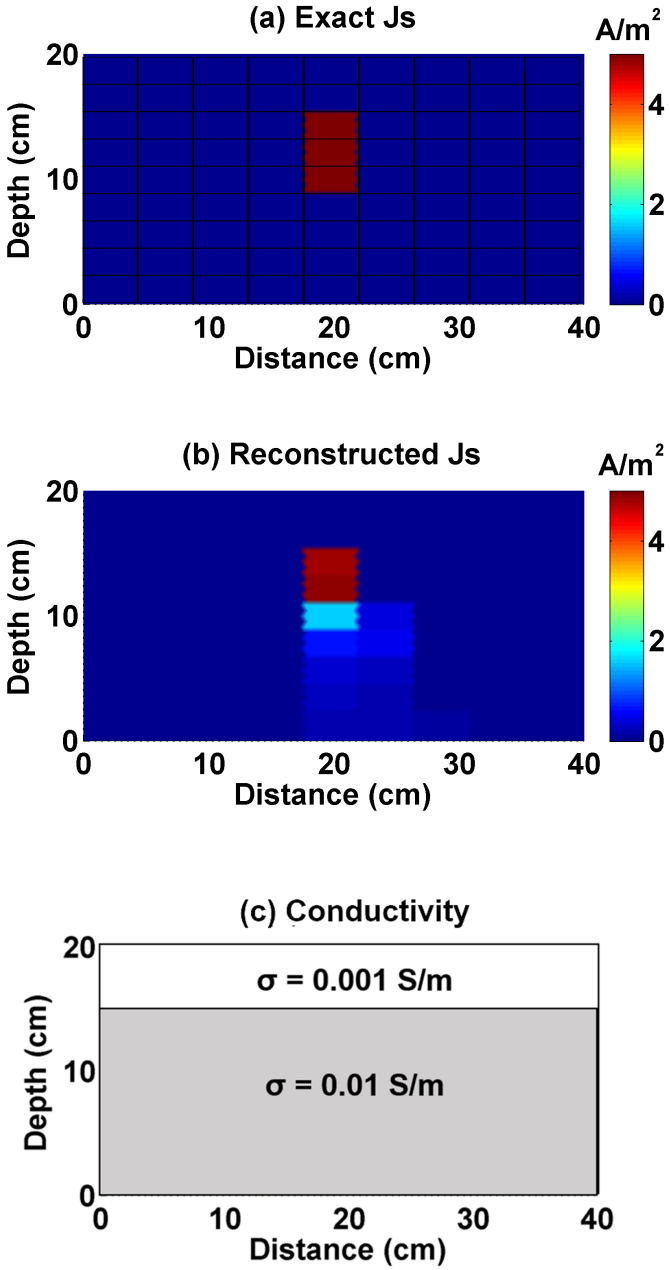

Figure 5.9: Synthetic example.(a) True source current density.(b) Result of the inversion using LSQR algorithm.(c) Distribution of the electrical conductivity.

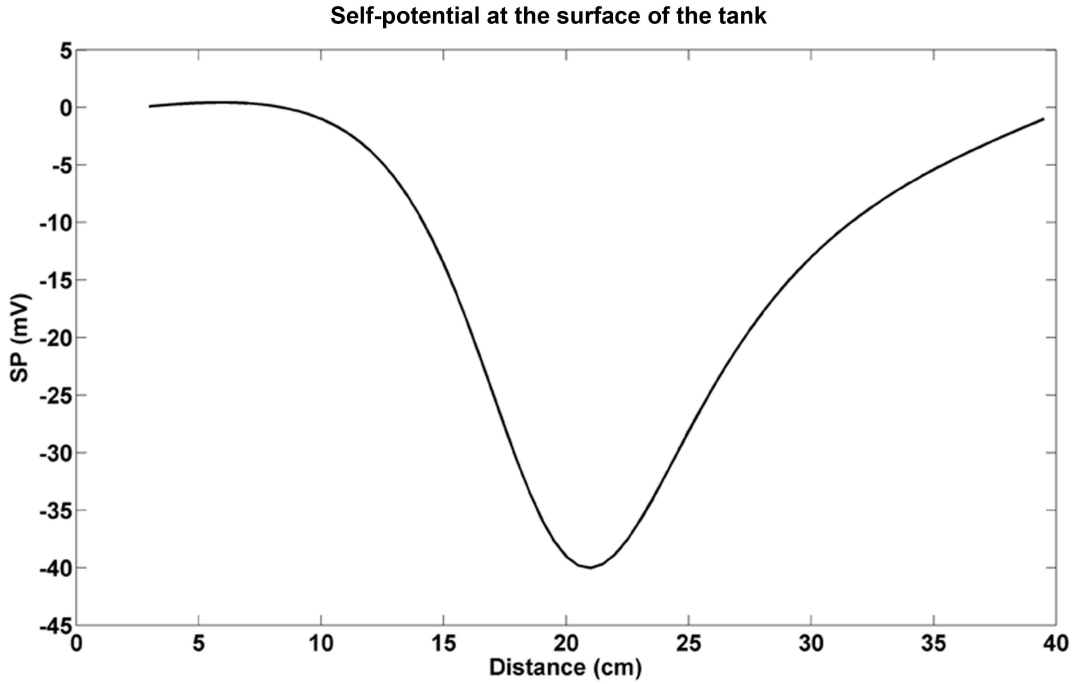

Figure 5.10: The self-potential signal calculated at the surface of the model (z=20 cm).

shows the progressive development of the negative SP anomaly located above the vertical bar during experiment.

On the 8th week of experiment, the negative surface anomaly, indicating a flux of electrons through the metallic bar, was deemed to have reached a steady-state condition, and the SP depth data collection was conducted throughout the tank. Figure 5.12 shows the 2D vertical cross section of the self-potential. The polarity of the anomaly agrees with field observations [111] and the amplitude is similar to those reported in the laboratory by [108]. The self-potential distribution has a dipolar character, with a positive anomaly located in the bottom part of the iron bar and a negative anomaly located in the vicinity of the top part of the metallic object.

After 8 weeks, the iron bar was removed from the tank and evidence of corrosion was observed on its surface (Figure 5.13). It was possible to notice that the colour of the sand in the vicinity of the iron bar turns into a blue-greenish colour over time. If the sand is exposed to air, this colour turns to ochre.

This behaviour is typical of the formation of fougerite (the green rust is transformed into lepidocrocite when exposed to air, see [136].

Figure 5.14 illustrates the results of 2D inversion of surface electrical-resistivity measurements. ERT dataset were inverted with the VEMI algorithm - Versatile interface for Electrical Modelling and Inversion-, built within the EIDORS en-

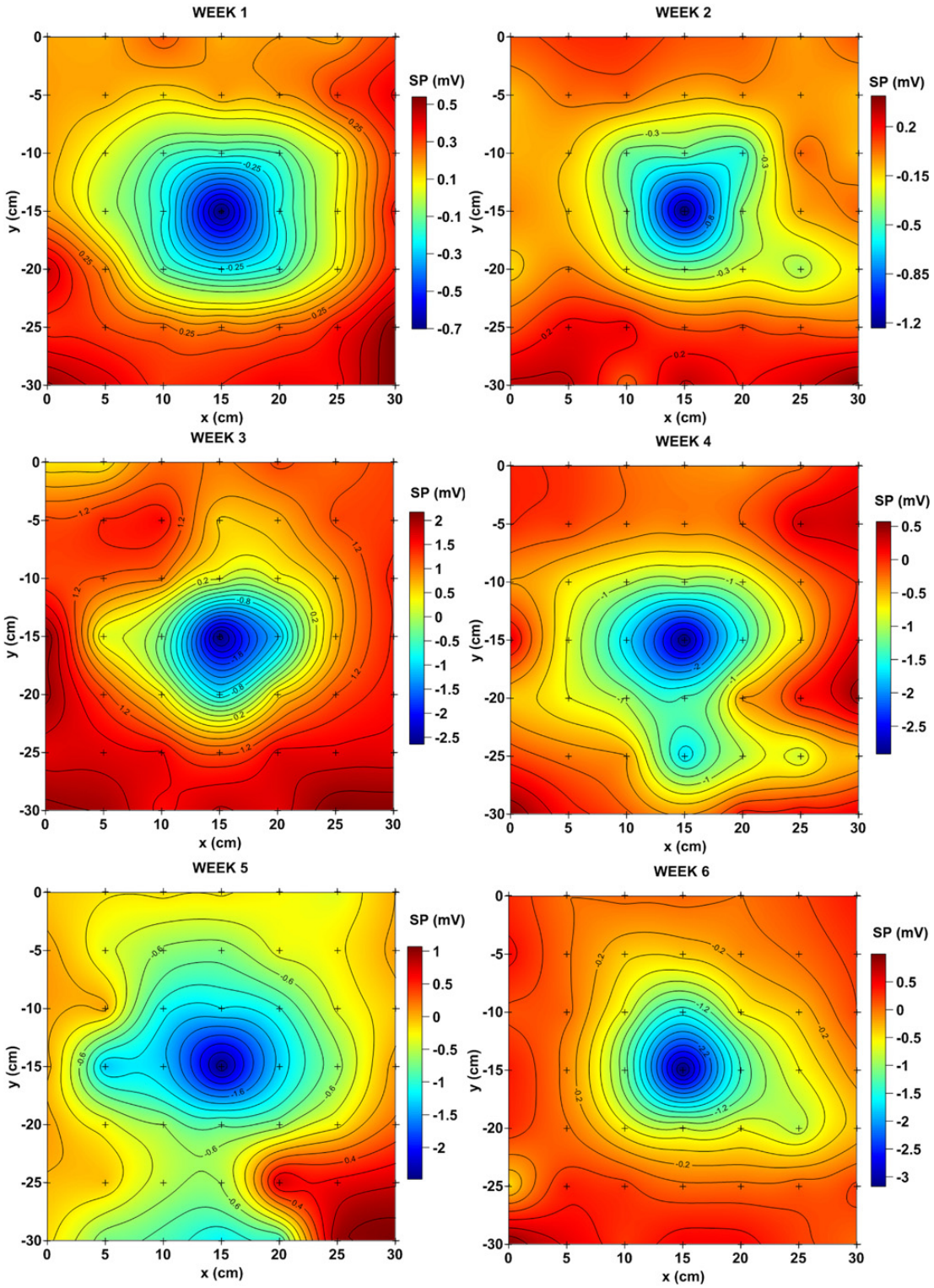

Figure 5.11: Sequence of 2D SP data (plan-view) collected on the surface of the sand in experiment. Redox processes resulted in the development of a -45 mV anomaly in two months (*Figure continues on page 81*).

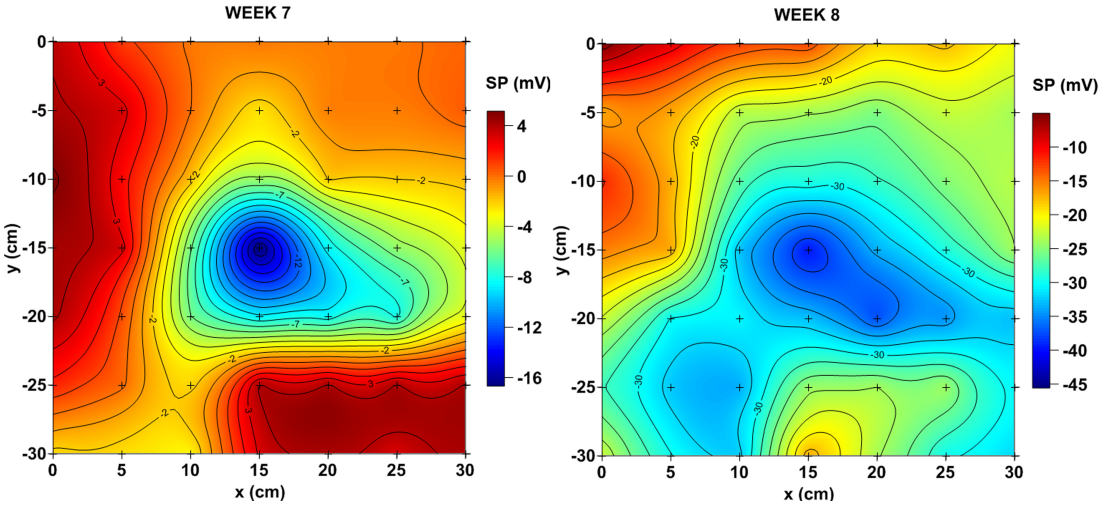

Figure 5.11: -*Continued.*

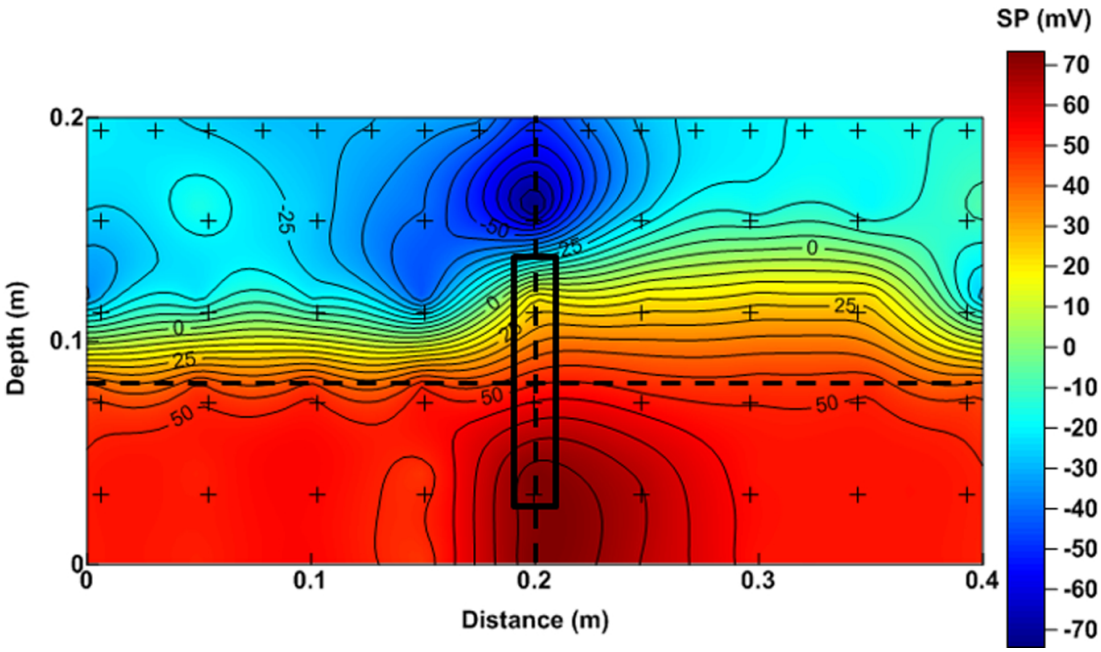

Figure 5.12: 2D vertical cross section of SP data collected on day 60 of experiment. A relatively large dipolar perturbation in the electrical potential field can be seen to have developed along the vertical iron bar.

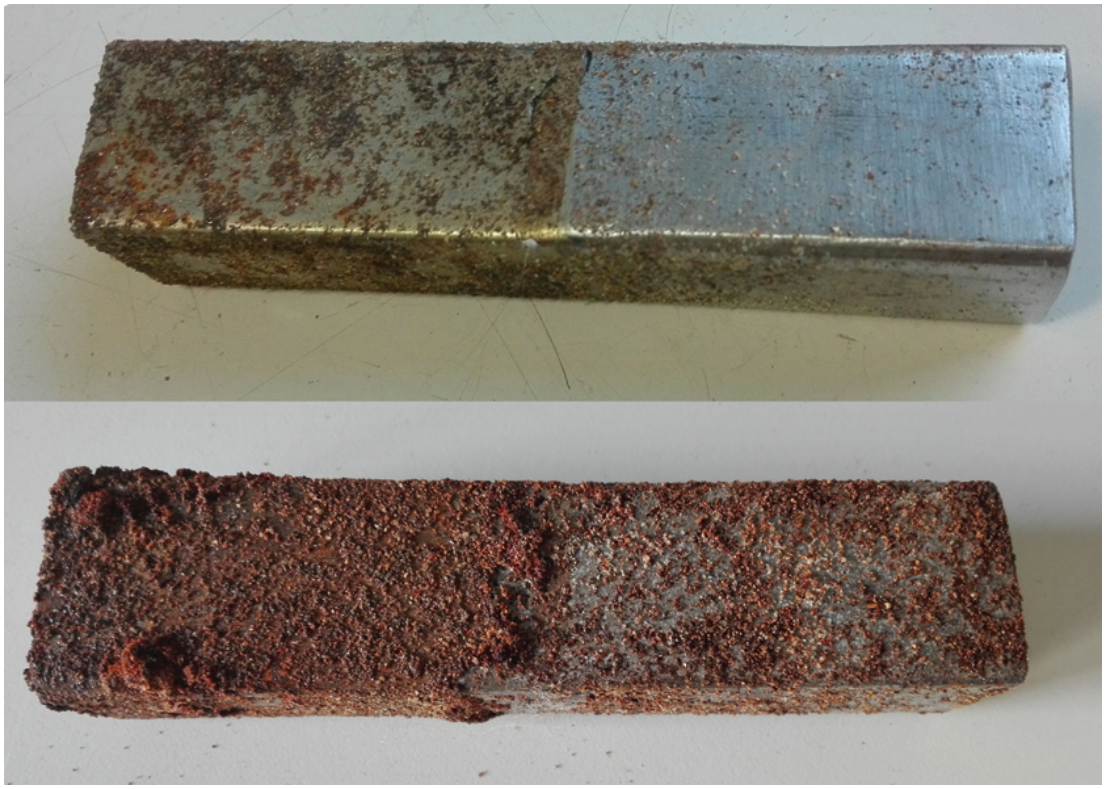

Figure 5.13: Picture showing the almost totally clean surface of the bar after a week (upper) and the presence of lepidocrocite at the end of the experiment (lower).

vironment [3]. This algorithm is able to perform both 2D and 3D inversion, by solving the forward problem with a finite-element approximation of the Poisson equation governing the physical problem while inversion is carried out using a Gauss-Newton formulation [35, 36, 37]. The code incorporates the electrode size (penetration depth for rods and plate length for surface electrodes) within the forward modelling. It is also possible to add a priori information to the inversion process. In this particular case, for all the boundaries, Neumann-type boundary conditions were assumed. Resistivity varies from 200 Ωm in the saturated portion of the tank to 3500 Ωm close to the surface of the tank.

Once the algorithm was tested, experimental resistivity and depth SP data were used as input for the inversion to localize the causative source body. In the first step, the kernel computation accounted for the electrical resistivity distribution (Figure 5.14) and for the insulating boundary conditions applied to the system and governed by the tank walls. In the second one, the reconstruction of the electric source current density required self-potential data along the cross-section perpendicular to the tank (Figure 5.12). Figure 5.15 illustrates 2D inversion results, where from top to bottom shows the observed SP data, the magnitude of the recovered source current density distribution calculated using the

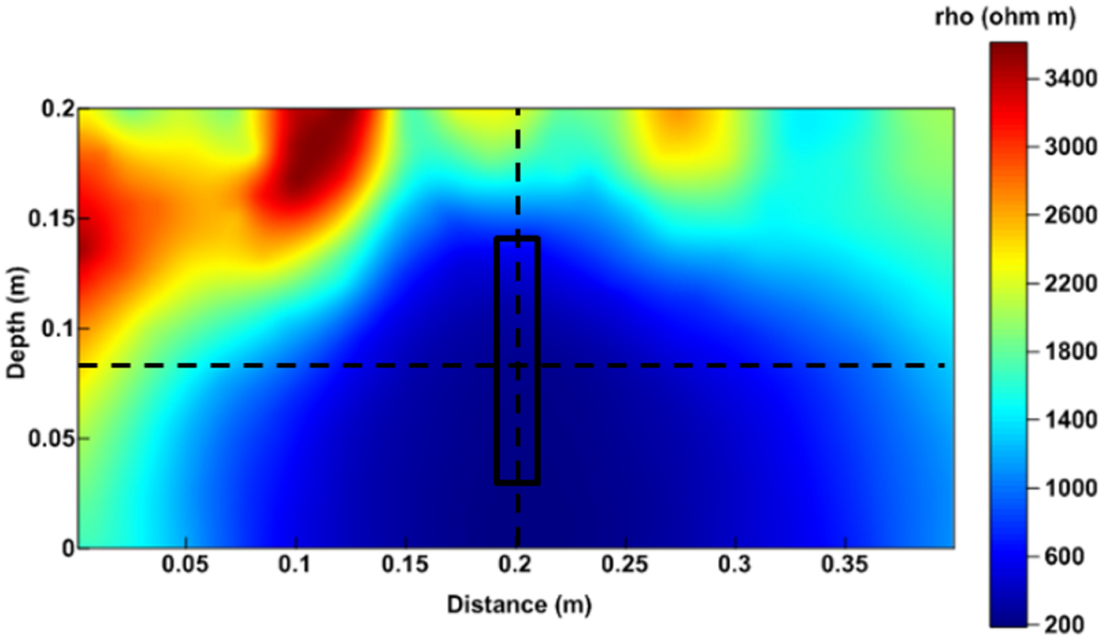

Figure 5.14: 2D resistivity tomography. The resistivity ranges from 200 ohm-m in the saturated portion of the tank (and in the capillary fringe) to nearly 3500 ohm m close to the top surface of the tank.

recovered 2D vector field of source current density distribution and the recovered SP data, respectively.

The development of an SP anomaly associated with the corrosion rate of the vertical metallic bar is clear. Using the GCV approach to selecting an appropriate regularization term and imposing weighted smoothness constraints on depth as described in Chapter 4, the inversion returns a predominantly vertical current density that is elongated in the z-direction, which means a single dominant vertical dipole extending from top to bottom of the bar. Although the anomaly is not perfectly centered on the coordinates of the metallic body, reveals indication of the vertical length with relative high-amplitude source current distributions in the upper part of the bar. The coordinate discrepancy could mainly due to the spatial refinement of the kernel matrix and resultant model parameterization spacing used for this study. Added constraints such as object's location, size, and orientation would help to ensure that source currents in the recovered model were predominantly in the exact position but they were not applied to the inversion procedure so as to represent a more realistic scenario in which target object's dimensions are unknown.

There is very good agreement between the measured and recovered SP distribution (Figures 5.15a and c) in terms of trend with a negligible change in values (RMSE=10 mV), demonstrating that this inversion process is useful in recon-

struction of source current density distribution at depth whereas the recover of the shape and the position of the principal anomalies is given higher priority than reconstructing their amplitude.

5.2 Field survey: the San Vittorino Sinkhole Plain

The inversion algorithm was then applied to a field data set collected in the San Vittorino Plain, located in Central Italy [23] in order to investigate the effects of different resistivity structure assumptions on the SP inversion results. The spatial distribution of sources provides useful information that can subsequently be interpreted in terms of physical processes that generate the SP data. In particular, it is shown how the SP signals can help to identify the location of sinkholes.

5.2.1 Hydrogeological background

The San Vittorino Plain lies on the Velino River Valley floor at an elevation of 425-400 m above sea level (a.s.l.) and is bordered by the Terminillo and Reatini mountain chains on the right bank of the Velino River and by the Giano-Nuria mountain chain towards East on its left bank. The area is at the meeting point between the Latium-Abruzzi carbonate Apennines (Mt. Nuria-Mt. Giano ridge) and the Umbria- Marches-Sabina domain (Mt. Terminillo ridge).

The lithology of the geological units is substantially calcareous even if some of them also show a variable alternation of marly-calcareous-cherty layers. The plain, in particular, is characterized by a karst affected carbonate bedrock, arranged in a set of splays with clayey-marly or siliciclastic footwall (whose thickness is estimated to be more than 150 m along the plain) and filled by fluvial and lacustrine deposits of the upper Pleistocene–Holocene; gravel lenses and travertine (mostly sandy) are found locally (Figure 5.16).

The middle valley of the Velino River and the S. Vittorino Plain are the areas of discharge of important fractured carbonate aquifers belonging to the carbonate platform domain. The key factors controlling the points of discharge of groundwater are: i) the fractured carbonate aquifers supplying the regional groundwater of the Giano-Nuria- Velino Mts. hydrogeological system; ii) the Mt. Paterno-Canetra hydrogeological unit, through which a substantial portion of groundwater flows and, above all, iii) the multi-layered aquifer of the Quaternary intramontane plain of S.Vittorino, where carbonate groundwater mixes with dominantly gaseous deep fluids rising from the main discontinuities. The spring

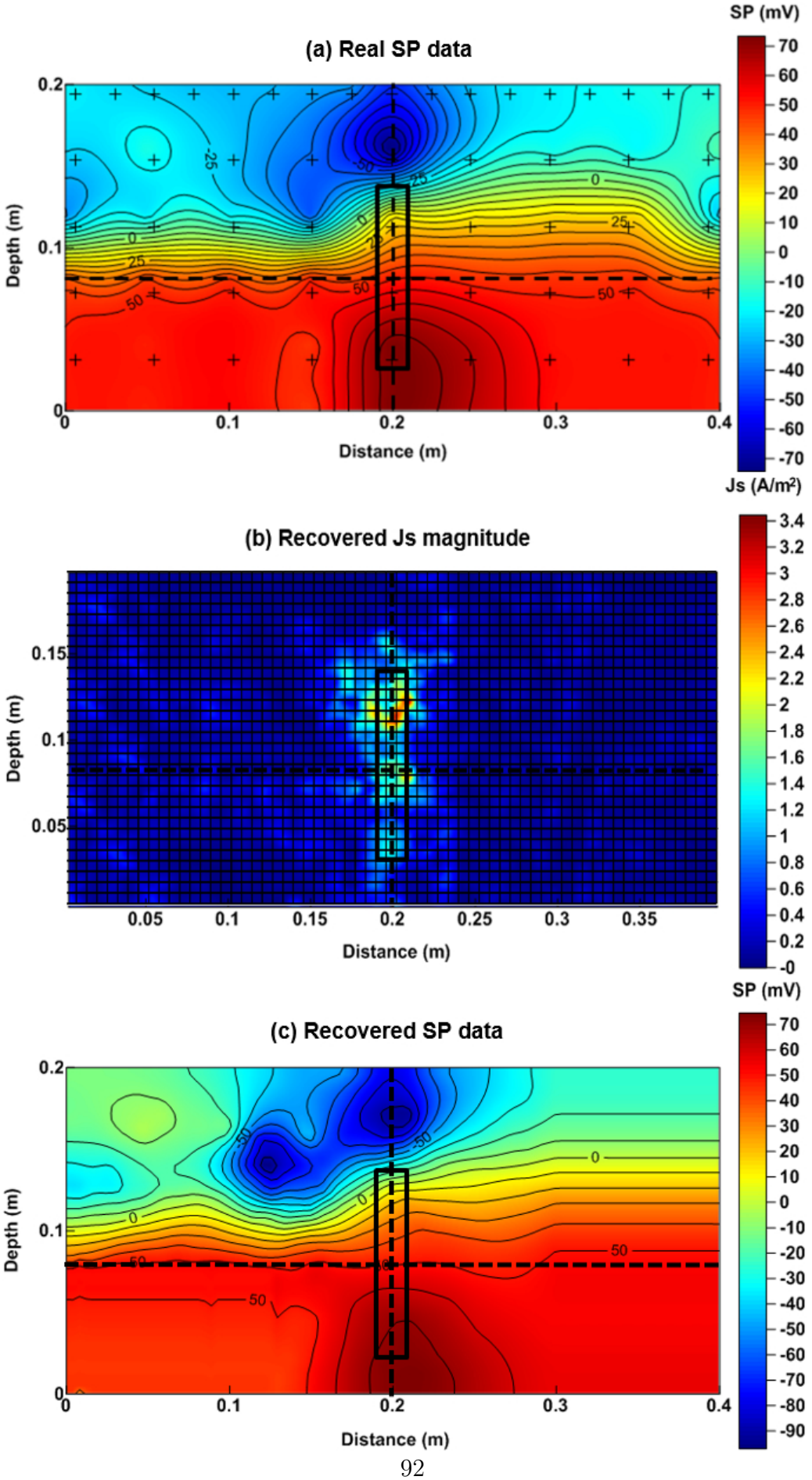

Figure 5.15: Inversion results showing color contour plots of the (a) observed and (c) recovered SP depth data, and (b) magnitude of the current density distribution $\mathbf{J_s}$.

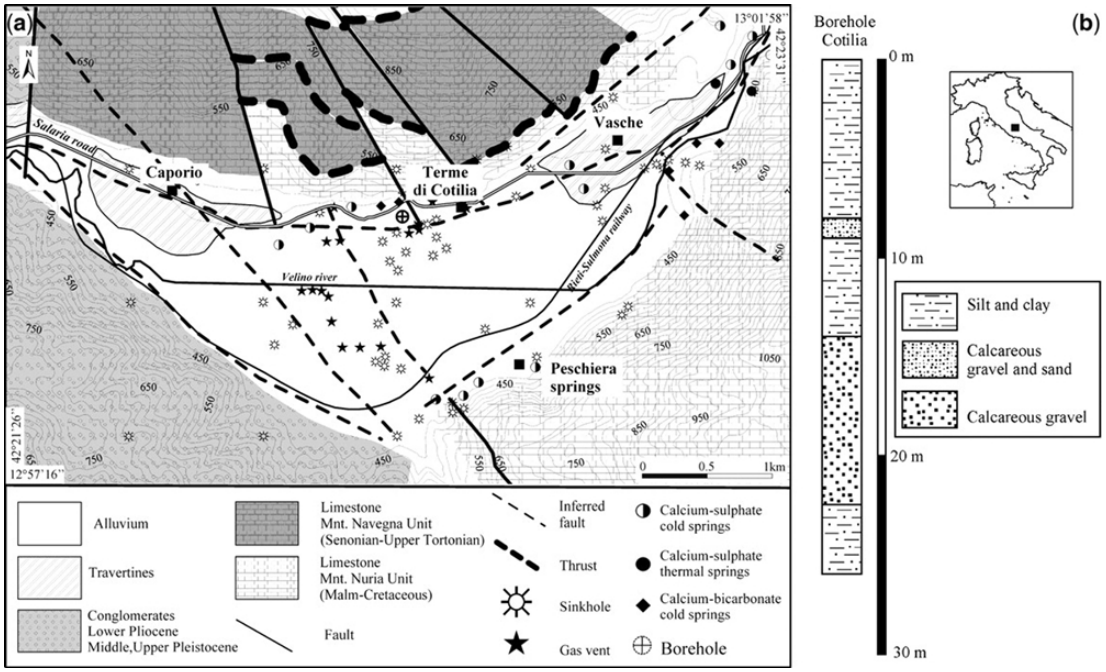

Figure 5.16: Simplified geological map of the sinkhole-prone area in the S. Vittorino Valley (Latium) with a borehole data stratigraphic column (after [81]).

water intake structures and the Velino River flood control works complicate the natural situation [96].

This plain, extensively studied in the past through geological, hydrogeological, geophysical and geochemical surveys, is also characterized by the presence of numerous sinkholes, often filled with mineralized spring waters. The development of sinkholes in the study area is mainly due to deep suffusion and deep piping processes, linked to fluid upwelling along fracture-fault systems and to dissolution (by H_2S and CO_2) in the continental deposits [28]. The wide circulation of waters in this area, which includes the presence of the Peschiera Spring system with a relevant discharge rate of about 18 m^3s^{-1}, emphasized the action of karst processes. In addition, the minimum depth to the water table in the alluvial-detrital deposits, the complex hydrodynamics of subsurface water discharge and the aggressiveness of waters in some sectors play a crucial role, in developing sinkholes.

The sinkholes, although generally of subcircular shape, exhibit a wide range of diameters (a few to several tens of metres) and persistence over time. Some of them are now inactive, others are seasonally recharged and others constitute permanent ponds and lakes. This different behaviour is probably due to the different nature and flow-rate of the water discharge at each spring, although a detailed understanding of the occurrence of the sinkholes, triggering factors and development is still incomplete. They are mainly located in the norther sector of

the plain and are aligned along the NE-SE path of the Fiamigiano-Micciani fault. The most recently formed sinkhole lies in the northern sector of the plain close to the Cotilia thermal bath. It is a small circular pond with springs and gas vents.

5.2.2 Data acquistion

Cardarelli et al. [23] employed self-potential method in combination with electrical and seismic tomography for detection of piping sinkholes in the San Vittorino Plain, located in Central Italy, along the Velino River Valley.

We focused only on the results of the ERT and SP surveys performed on the line illustrated in Figure 5.17, where surface evidence of a piping sinkhole appeared with the formation of a small water pond (around 2.0 m diameter) after about one year from the geophysical measurements. The goal was to verify that negative SP signals are associated with the position of this known sinkhole (this is marked as "A" in Figure 5.17).

ERT line was carried out using Iris Syscal Pro resistivity meter equipped with 48 electrodes (stainless steel stakes) spaced 2 m apart, depending on the target depth and the required resolution. ERT 2D pseudosection was inverted using the VERDI algorithm [24]. The pole-dipole array was employed, as it combines consistent signal strength with good resolution and depth of investigation.

SP measurements were collected with Pb/PbCl2 non-polarizable electrodes and ABEM Terrameter SAS300 resistivity meter using a simple scheme for data acquisition with a reference (fixed) electrode and a moving one. The SP contribution of the main groundwater flow in the SW-NE direction towards the Velino River [96], which can be considered as linear on first approximation, was removed from the raw data in the x and y-directions, by a linear interpolation along both directions.

5.2.3 Inversion of field data

Because sinkholes are associated both with self-potential and electrical conductivity anomalies, an inversion of self-potential data using the LSQR approach is proposed as a way of delineating the location of the known sinkhole. Both field SP data and ERT results are necessary inputs to the inversion algorithm: the self-potential method is the only geophysical method that is sensitive to the flow of groundwater while the inversion of the resistivity data provides the distribution of electrical conductivity, which is sensitive to the water and clay contents of the shallow cover.

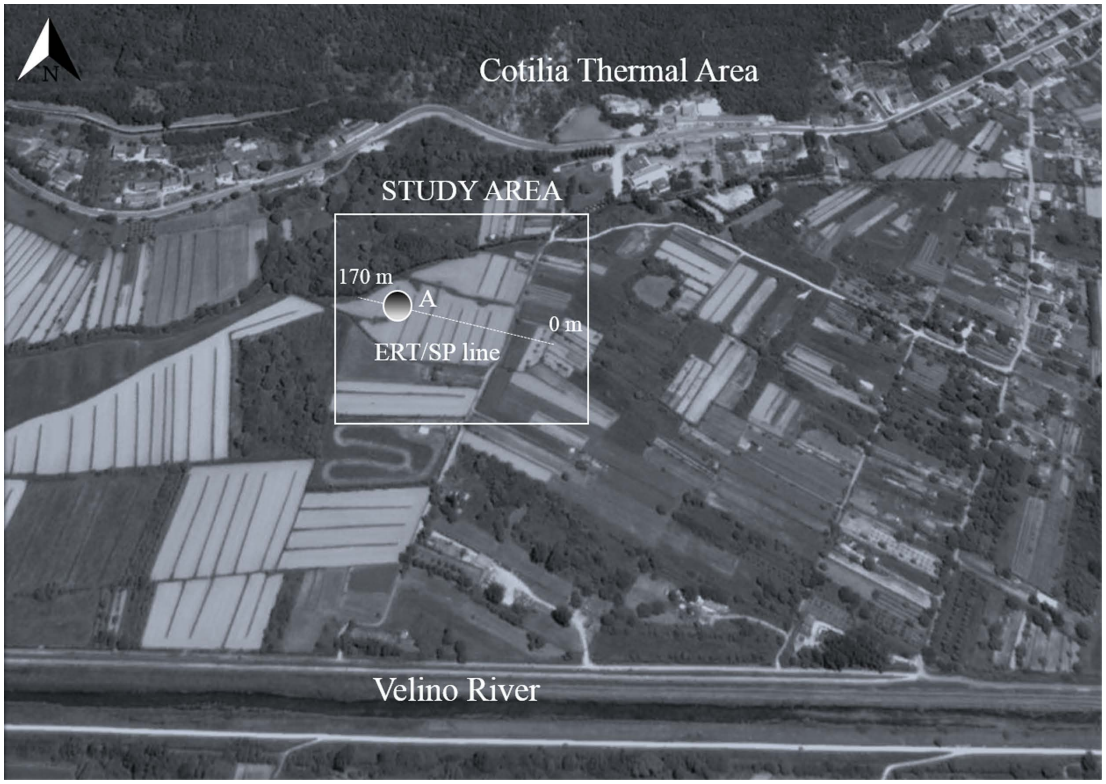

Figure 5.17: Aerial plan of the surveyed area and position of the ERT and SP line.

The results of the ERT investigation is reported in Figure 5.18a. The anomaly (marked by a black dashed line) corresponding to the conductive geometry is not perfectly U-shaped, probably because of the effect of the water table, which is supposed to be at about 3–5 m depth, as indicated by seismic velocities above 1500 ms^{-1} in the seismic section (Figure 5.18b). Anyway, the ERT anomalous area confirms the geometrical reconstruction and identifies morphologies that suggest the presence of an incipient sinkhole.

The result of the application of the inversion algorithm to the self-potential anomaly observed at the top surface is shown in Figure 5.19.

The positions of the insulating boundary conditions and the reference electrode were used to determine the kernel. The solution depends on the value of the regularization parameter λ and a prior model. To determine the value of λ the GCV method was used (Figure 5.20) while no a prior model was adopted. A depth-weighting matrix (see Chapter 4) was introduced to counteract the sensitivity of the kernel matrix to near-surface model parameters and to force the source to depth within the model space.

The source (Figure 5.19a) and the negative anomaly (Figure 5.19b) are located in correspondence of the incipient sinkhole markes as A. Although the inversion of surface self-potential data tends to generate a shallower source current density

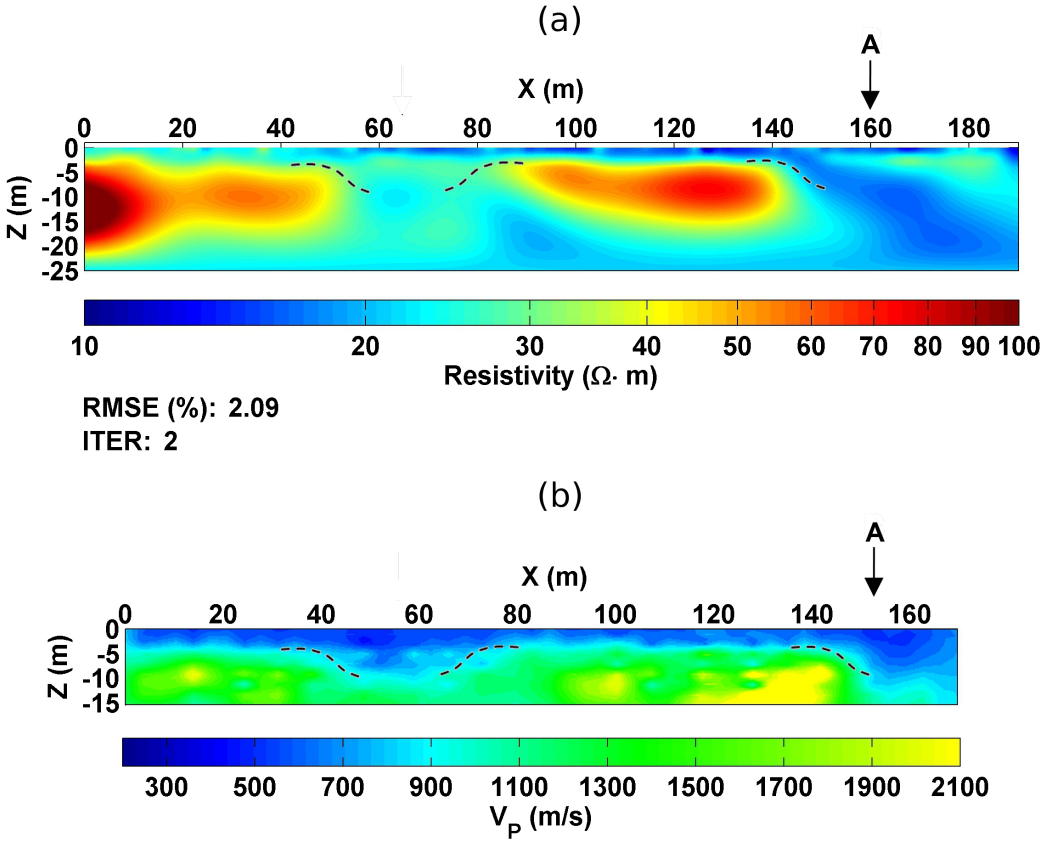

Figure 5.18: (a) Inverted model of ERT line. (b) Inverted model of STR line (after[23], modified). Black arrow indicates the sinkhole marked as A. Black dashed lines indicate the shape of the anomalous zones.

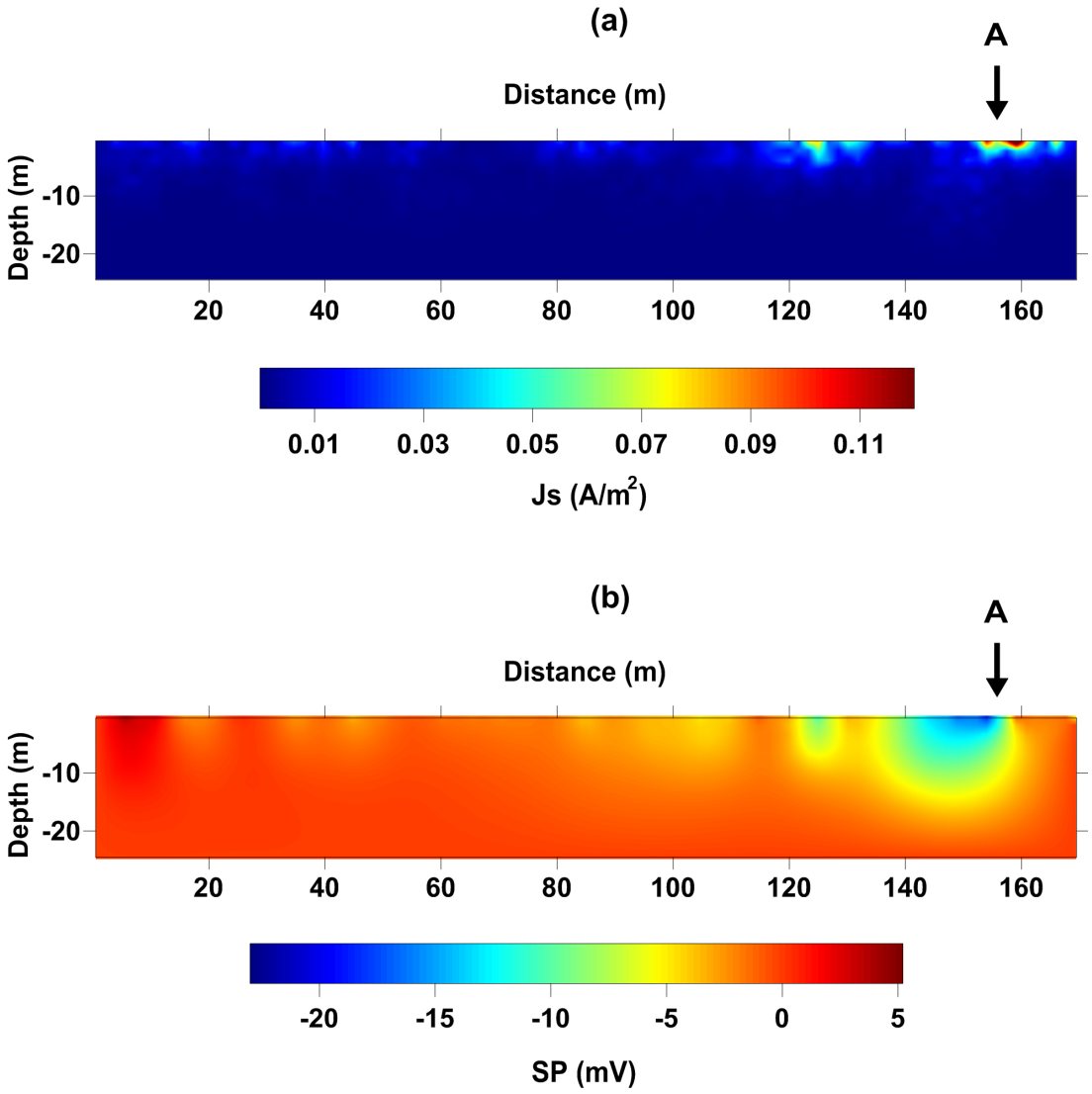

Figure 5.19: Inversion results. (a) Magnitude of the inverted two-dimensional streaming current source density accounting for the resistivity distribution shown on Figure 5.18. (b) Distribution of the reconstructed self-potential signals.

distribution (Figure 5.19a) because the sensibility of the self-potential field decays quickly with the depht, the proposed approach permits however highly precise localization of the sinkhole.

Negative anomalies, associated with the percolation of water in the sinkhole, are of a few tens of millivolts as showed by [58]. It is worth noting that there is also a minor anomaly likely associated with a shallow smaller sinkhole at x=125 m.

A comparison between the self-potential profile measured at the ground surface and the self-potential profile determined from the inversion process along the same profile is shown in Figure 5.21. It is possibile to see a good agreement between the model and the data (RMSE = 2 mV). This indicates clearly that

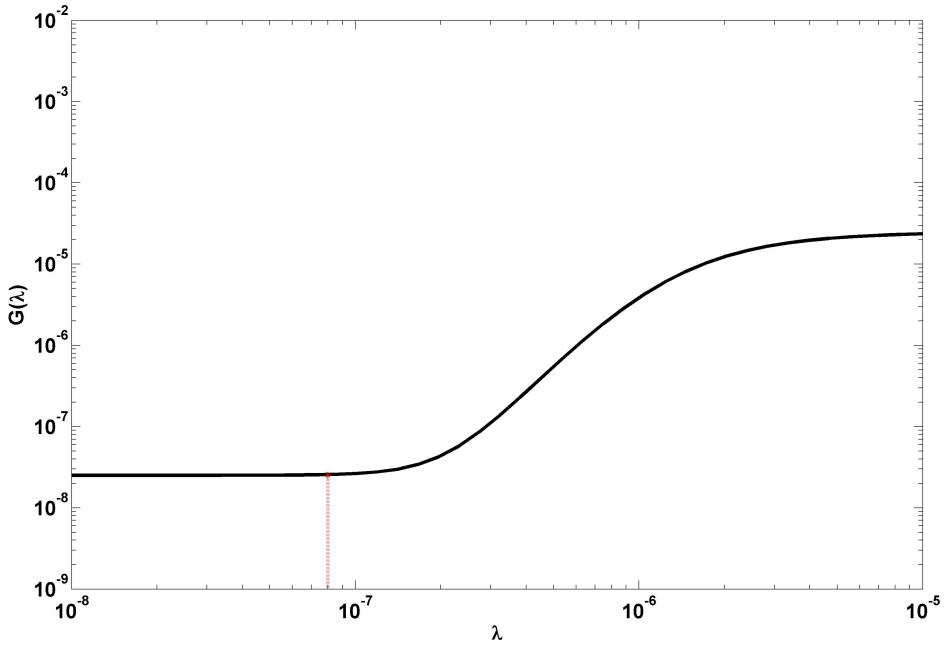

Figure 5.20: Determination of the regularization parameter using the GCV method.

self-potential signals can be used to observe remotely the pattern of groundwater flow (or changes in this pattern) and to detect the occurrence of sinkholes when the support volume of the source is small with respect to the distance between the position of the center of the source and the reference point.

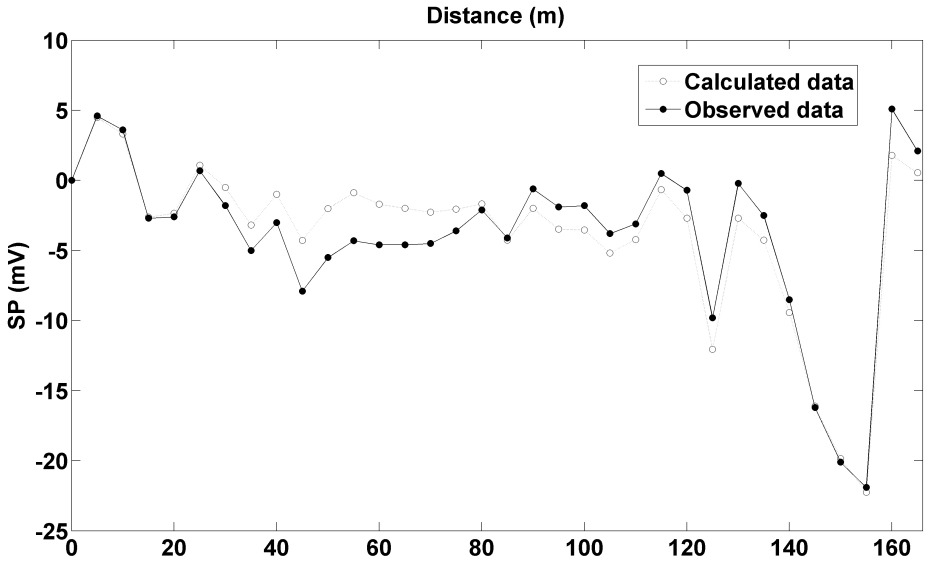

Figure 5.21: Comparison between the self-potential signals determined at the ground surface using the inversion algorithm (empty circles) and the self-potential measurements performed along profile (filled circles).

Chapter 6

Conclusions

The aim of this dissertation has been to explore thoroughly potential and limits of quantitative reconstruction of self-potential distribution for environmental and engineering applications, starting from the controlled laboratory conditions and ending with field investigations. The main objectives presented in Section 1.3, has provided the following conclusions:

1. The solution of the 2-D forward problem for the self-potential is achieved by computing the Green functions entering the Kernel and the Poisson equation numerically for elementary dipoles through the Galerkin method. The finite element algorithm, implemented in Matlab to solve numerically these equations, has proven to be accurate and stable through a comparison with synthetic simulations. The modeling method is a three-step process. First, the Poisson equation is solved with piecewise (Neuman or Dirichlet) boundary conditions for the pressure or groundwater flow. Then, the current source density is calculated on the basis of previously obtained hydraulic and/or redox gradient distribution. Finally, the SP signals are computed by solving the Poisson equation with appropriate boundary conditions on the electrical potential. This approach has been used to produce 2D reconstruction of steady state flow models in anisotropic, heterogeneous and water-saturated porous materials such as the model of a leak in a dam, the case of a pumping test in an unconfined aquifer and the problem of coupled hydroelectric problem associated with the presence of a cavity. The use of an adaptive mesh, denser near the regions requiring more resolution and having an high quality factor, can help to reduce errors in forward computations without increase exponentially the allocated memory. There are two significant benefits of this code: (1) the flexibility for incorporating complicated model geometries and (2) the multiphysics approach that allows the

physics of the source mechanism to be coupled directly into the problem;

2. Thanks to the experimental apparatus which was developed, it has been possible to simulate SP anomalies observed in the vicinity of buried metallic objects and ore bodies or over groundwater plumes associated with organic contaminants. Preliminary tests have highlighted the main problems due to saturation, electrode effects and sand performance. These preliminary measurements seem to be essential to ensure the generation of a large-amplitude SP response and to remove potential errors into recovered datasets. The physical model built up in the laboratory have demonstrated that, to produce SP signals associated with a redox potential gradient, an electronic conductor localized in the capillary fringe has to intercept an area of strong redox potential gradient. The generation of an electrical current in the metallic material is associated with the corrosion of the metallic material and the formation of a dipolar SP anomaly. The far field contribution varied with depth and ranged from 70 mV at the top surface of the tank to -70 mV at the bottom. This feature implies an abrupt change from oxidizing to reducing conditions. It is likely that the chemical reactions at the surface of the iron bar consumed the dissolved oxygen of the pore solution and make its diffusion slower. The corrosion modifies the conductivity distribution (by forming a resistive crust on the surface of the metallic object) and the distribution of the redox potential in the vicinity of the metallic object;

3. A deterministic and local approach, which consists of inverting for the source current density distribution using the linear formulation of the forward problem and the modified singular value decomposition, is presented. When the solution is obtained, the forward problem is solved together with the RMSE absolute value. Then, when necessary, the calculated model is updated to compute new SP distribution until the desired RMSE tolerance criterion, depending on the nature of the problem under investigation, is fulfilled. The inversion algorithm is based on the subspace preconditioned LSQR algorithm to compute (an approximation to) the standard-form Tikhonov solution for a fixed value of the regularization parameter. The preconditioner is based on the subspace defined by the columns of the Kernel matrix whose columns should be "smooth" and preferably chosen such that a significant component of the exact solution lies in the range of the matrix. The method adopted for choosing the regularization parameter is the generalized cross-validation (GCV). Simulations with Gaussian noise, performed on heterogeneous models with synthetic anomalies included, pro-

vide low-error inverted models whereas anomalies are well-detected both for shape and position. The decrease of resolution, due to the fact that the self-potential field decays quickly with the distance, is controlled by the numerical procedure even though the amplitude response is not completely satisfactory whereas there is not an adaptive mesh. However, it is worth to underline that the recover of the shape and the position of the principal anomalies is given higher priority than reconstructing their amplitude.

4. Laboratory and field investigations results have confirmed the reliability of the algorithm proposed. There is a good agreement between the measured and recovered SP signals, demonstrating that the inversion process is useful in quantitatively reconstruction of source current density distribution in terms of location and shape. This indicates clearly that self-potential can be used to observe remotely the pattern of groundwater flow (or changes in this pattern) and to detect the occurrence of sinkholes, as well as the buried SP sources at depth in regions where electronic conductors exist. In light of this the goal to develop an accurate and stable finite element algorithm to solve forward and inverse problems for the self-potential has been achieved. Future work should concern further developments on the optimization of the inversion approach, looking also at the 3-D formulation and new engineering and environmental applications. In this sense the Matlab algorithm developed in this work including the whole geophysical data processing, can be improved through the insertion of new functions in order to extend the basic approach to allow for more complicated scenarios where anomalies are due to deeper sources responsible for both the streaming potential and the electrochemical potential.

Bibliography

[1] Abbas M. A. and Fedi M., 2014: Automatic DEXP imaging of potential fields independent of the structural index. Geophysical Journal International, 199(3), 1625-1632.

[2] Abdelazeem M. and Gobashy M., 2006: Self-potential inversion using genetic algorithm. J. King Abdulaziz Univ., Earth Sci. 17, 83-101.

[3] Adler A. and Lionheart W., 2005: Uses and abuses of EIDORS: an extensible software base for EIT. Physiological Measurement 27, 25-42.

[4] Agarwal B.N.P.and Srivastava S., 2009: Analyses of self-potential anomalies by conventional and extended Euler deconvolution techniques. Comput. Geosci. 35, 2231-2238.

[5] Alberty J., Carstensen C. and Funken S., 1999: Remarks around 50 lines of Matlab: short finite element implementation. Numer Algorithms 20(2–3), 117-137.

[6] Arora T., Linde N., Revil A. and Castermant J., 2007: Non-intrusive determination of the redox potential of contaminant plumes by using the self-potential method. Journal of Contaminant Hydrology, 92, 274-292.

[7] Atekwana E.A.and Slater Lee D., 2009. Biogeophysics: A new frontier in Earth science research. Reviews of Geophysics, 47, RG4004.

[8] Barde-Cabusson S. and Finizola A., Version: 10 April 2012: Tutorial for Self Potential data processing.

[9] Bastos J.P.A and Sadowski N., 2004: Electromagnetic modeling by finite element methods. Marcel Dekker. New York.

[10] Bear J., 1988: Dynamics of fluids in porous media. Dover Publication, New York.

[11] Bhattacharya B.B. and Roy N., 1981: A note on the use of nomograms for self-potential anomalies. Geophysical Prospect., 29, 102-107.

[12] Bigalke J. and Grabner E.W., 1997: The geobattery model: A contribution to large-scale electrochemistry. Electrochimica Acta 42, 3443-3452.

[13] Birch F. S., 1998: Imaging the water table by filtering self-potential profiles, Ground Water, 36(5), 779-782.

[14] Biswas A.and Sharma S. P.,2014: Optimization of Self-Potential interpretation of 2-D inclined sheet-type structures based on Very Fast Simulated Annealing and analysis of ambiguity. Journal of Applied Geophysics, 105, 235-247.

[15] Blakely R. J., 1996: Potential Theory in Gravity and Magnetic Applications. Cambridge University Press. Cambridge.

[16] Bockris J.O'M. and Reddy A.K.N., 1970: Modern Electrochemistry, Vol. 2. Plenum Press, New York.

[17] Bogoslovsky V. A. and Ogilvy A. A., 1973: Deformation of natural electric fields near drainage structures. Geophysical Prospecting, 21, 716-723.

[18] Bolève A., Revil A., Janod F., Mattiuzzo J. L., and Jardani A., 2007: Forward modeling and validation of a new formulation to compute self-potential signals associated with ground water flow: Hydrology and Earth System Sciences, 11, 1661-1671.

[19] Bolève A., Revil A., Janod F., Mattiuzzo J. L., and Fry J., 2009: Preferential fluid flow pathways in embankment dams imaged by self-potential tomography: Near Surface Geophysics, 7, 447-462.

[20] Brown S.R., Lesmes D., Fourkas G. and Sorenson J.R., 2003: Complex Electrical Resistivity for Monitoring DNAPL Contamination. Final Technical Report, U.S. Department of Energy.

[21] Butler J.J., 1988: Pumping tests in nonuniform aquifers -the radially symmetric case. Journal of Hydrology, 101, 15-30.

[22] Cardarelli E. and Di Filippo G, 2009: Electrical resistivity and induced polarization tomography in identifying the plume of chlorinated hydrocarbons in sedimentary formation: a case study in Rho (Milan - Italy). Waste Management and Research 27, 595-602.

[23] Cardarelli E., Cercato M., De Donno G. and Di Filippo G., 2014: Detection and imaging of piping sinkholes by integrated geophysical methods. Near Surf. Geophys., 12, 439-450.

[24] Cardarelli E. and Fischanger F., 2006: 2D data modeling by electrical resistivity tomography for complex subsurface geology. Geophysical Prospecting 54, 121-133.

[25] Cassiani G., Kemna A., Villa A. and Zimmermann E., 2009: Spectral induced polarization for the characterization of free-phase hydrocarbon contamination of sediments with low clay content. Near Surface Geophysics 7, 547-562.

[26] Castermant, J., Mendonça C. A., Revil A., Trolard F., Bourrié G. and Linde N., 2008: Redox potential distribution inferred from self-potential measurements associated with the corrosion of a burden metallic body. Geophysical Prospecting, 56, 269-282.

[27] Cella F., Fedi M., 2012: Inversion of potential field data using the structural index as weighting function rate decay. Geophysical Prospecting, 60, 313-336.

[28] Centamore E., Nisio S. and Rossi D., 2009: The San Vittorino Sinkhole Plain: relationships between bedrock structure, sinking processes, seismic events and hydrothermal springs. Italian Journal of Geosciences, 128, 629-639.

[29] Cerepi A., Cherubini A., Garcia B., Deschamps H. and Revil A., 2017: Streaming potential coupling coefficient in unsaturated carbonate rocks. Geophysical Journal International. 210. 291-302.

[30] Chambers J.E., Wilkinson P.B., Wealthall G.P., Loke M.H., Dearden R., Wilson R., Allen D. and Ogilvy R.D, 2010: Hydrogeophysical imaging of deposit heterogeneity and groundwater chemistry changes during DNAPL source zone bioremediation. Journal of Contaminant Hydrology 118, 43-61.

[31] Corry, E., 1985: Spontaneous polarization associated with porphyry sulphide mineralization, Geophysics, 50, 1020-1034.

[32] Corwin R.F., 1990: The self-potential for environmental and engineering applications. In Geotechnicaland Environmental Geophysics, Ward SH(ed.).Society of Exploration Geophysicists, Tulsa, USA, Investigations in Geophysics, 5, 127-145.

[33] Corwin R.F. and Hoover D.B.,1979: The self-potential method in geothermal exploration. Geophysics 44, 226-245.

[34] Dahlin T., 2001: The development of DC resistivity imaging techniques.Computers and Geosciences, 27(9), 1019-1029.

[35] De Donno G., 2013: 2D tomographic inversion of complex resistivity data on cylindrical models. Geophysical Prospecting 61 (Suppl.1), 586-601.

[36] De Donno G. and Cardarelli E., 2014: 3D complex resistivity tomography on cylindrical models using EIDORS. Near Surface Geophysics 12(5), 587-598.

[37] De Donno G. and Cardarelli E., 2017: VEMI: a flexible interface for 3D tomographic inversion of time-and frequency-domain electrical data in EIDORS. Near Surface Geophysics 15(1), 43-58.

[38] de Groot S.R., 1951: Thermodynamics of irreversible processes. North-Holland, Pub. Co., Amsterdam, New York, 242.

[39] De Witte L., 1948: A new method of interpretation of self potential field data. Geophysics, 13(4).

[40] Di Maio R. and Patella D., 1994: Self-potential anomaly generation in volcanic areas. The Mont Etna case history, Acta Vulcanol., 4, 124 -199.

[41] Fedi M., Cella F., Quarta T. and Villani A.V., 2010: 2D Continuous wavelet transform of potential fields due to extended source distributions. Applied and Computational Harmonic Analysis, 28, 320-337.

[42] Fitterman D.V., 1978: Electrokinetic and magnetic anomalies associated with dilatant regions in a layered earth. Journal of Geophysical Research, 83(B12): 5923-5928.

[43] Fitterman D.V., Corwin R.F., 1982: Inversion of self-potential data from the Cerro Prieto geothermal field, Mexico. Geophysics 47, 938-945.

[44] Fox, R. W.,1830: On the electromagnetic properties of metalliferous veins in the mines of Cornwall. Philosophical Transactions of the Royal Society, 120, 399-414.

[45] Fournier C., 1989: Spontaneous potentials and resistivity surveys applied to hydrogeology in a volcanic area: Case history of the Chaîne des Puys (Puy-de-Dôme, France), Geophysical Prospecting, 37, 647- 668.

[46] Golub G., Heath M. and Wahba G.,1979: Generalized cross validation as a method for choosing a good ridge parameter, Technometrics 21, 215-224.

[47] Greenhouse J., Brewster M., Schneider G., Redman D., Annan P., Olhoeft G., Lucius J., Sander K., Mazzella A., 1993. Geophysics and Solvents: The Borden Experiment. The Leading Edge,1993, 261-267.

[48] Haas A. K., Revil A., Karaoulis M., Frash L., Hampton J., Gutierrez M., and Mooney M., 2013: Electrical potential source localization reveal a borehole leak during hydraulic fracturing: Geophysics, 78, 2, D93-D113.

[49] Hanke M. and Vogel C.R., 1999: Two-level preconditioners for regularized inverse problems I: Theory, Numerische Mathematik, 83, 385-402.

[50] Hansen P. C., 2008: Regularization Tools, A Matlab Package for Analysis and Solution of Discrete Ill-Posed Problems.

[51] Hansen, P. C., 1998. Rank-Deficient and Discrete Ill-Posed Problems: Numerical Aspects of Linear Inversion. SIAM, Philadelphia.

[52] Hase H., Hashimoto T., Sakanaka S., Kanda W. and Tanaka Y., 2005: Hydrothermal system beneath Aso volcano as inferred from self-potential mapping and resistivity structure. J Volcanol Geotherm Res 14, :259-277.

[53] Heinson G., White A., Lilley F.E.M., 2005: Rifting of a passive margin and development of a lower-crustal detachment zone: evidence from marine magnetotellurics. Geophysical Research Letters 32.

[54] Ikard S. J., Revil A., Jardani A., Woodruff W. F., Parekh M. and Mooney M., 2012: Saline pulse test monitoring with the self-potential method to non-intrusively determine the velocity of the pore water in leaking areas of earth dams and embankments: Water Resources Research, 48, W04201.

[55] Ishido, T. and Mizutani, H., 1981: Experimental and Theoretical Basis of Electrokinetic Phenomena in Rock-water Systems and its Applications to Geophysics, Journal of Geophysical Research, 86, 1763-1775.

[56] Iuliano T., Mauriello P. and Patella D., 2002: Looking inside Mount Vesuvius by potential fields integrated probability tomographies. Journal of Volcanology and Geothermal Research, 113, 363-378.

[57] Jacobsen M, Hansen P. C. and Saunders M. A., 2003: Subspace preconditioned LSQR for discrete ill-posed problems BIT Numer. Math. 43, 975-989.

[58] Jardani A., Dupont J. P. and Revil A., 2006: Self-potential signals associated with preferential groundwater flow pathways in sinkholes. Journal of Geophysical Research, 111, B09204.

[59] Jardani, A., Revil A., Barrash W., Crespy A., Rizzo E., Straface S., Cardiff M., Malama B., Miller C., and Johnson T., 2009: Reconstruction of the water table from self-potential data: A Bayesian approach: Ground Water, 47, 213-227.

[60] Jardani, A., Revil A., Santos F., Fauchard C. and Dupont J. P., 2007: Detection of preferential infiltration pathways in sinkholes using joint inversion of self-potential and EM-34 conductivity data: Geophysical Prospecting, 55, 749-760.

[61] Jardani A., Revil A., Bolève A., Crespy A., Dupont J.P., Barrash W. and Malama B., 2007: Tomography of the Darcy velocity from selfpotential measurements, Geophys. Res. Lett., 34, L24403.

[62] Jardani A., Revil A. and Dupont, J. P., 2006: Self-potential Tomography applied to the determination of cavities. Geophysical Research Letters, 33, L13401.

[63] Jardani A., Revil A., Bolève A. and Dupont J.P., 2008: 3D inversion of self-potential data used to constrain the pattern of ground water flow in geothermal fields. Journalof Geophysical Research113, B09204.

[64] Knight RJ, 2001: Ground penetrating radar for environmental applications. Annual Review of Earth and Planetary Sciences, 34, 229-255.

[65] Li Y. and Oldenburg D.W.,1998:3-Dinversionofgravitydata.Geophysics 63(1), 109-119.

[66] Linde N. and Revil A., 2007: Inverting residual self-potential data for redox potentials of contaminant plumes. Geophysical Research Letters, 34, L14302.

[67] Loke M. H., 1999: Electrical Imaging Surveys for Environmental and Engineering Studies.

[68] Maineult A., Bernabe Y. and Ackerer P., 2005: Detection of advected concentration and pH fronts from self-potential measurements. Journal of Geophysical Research, 110, B11205.

[69] Marshall D.J. and Madden T.K., 1959: Induced polarization, a study of its causes. Geophysics, 24(1), 790-816.

[70] Martínez-Pagán P., Jardani A., Revil A., and Haas A., 2010: Self-potential monitoring of a salt plume: Geophysics, 75, 4, WA17-WA25.

[71] Mboh C. M., Huisman J. A., Zimmermann E., Vereecken H., 2012: Coupled hydrogeophysical inversion of streaming potential signals for unsaturated soil hydraulic jproperties. Vadose Zone J. 11(2).

[72] Meiser P, 1962: A method of quantitative interpretation of self potential measurements. Geophys. Prosp., 10, 203-218.

[73] Mendonca C. A., 2008: Forward and inverse self-potential modeling in mineral exploration. Geophysics, 73(1), F33-F43.

[74] Minsley, B. J., Sogade J.and Morgan F. D., 2007a: Three-dimensional source inversion of self-potential data. Journal of Geophysical Research, 112, B02202.

[75] Minsley B. J., Sogade J. and Morgan F. D., 2007b: Three-dimensional self-potential inversion for subsurface DNAPL contaminant detection at the Savannah River Site, South Carolina. Water Resources Research, 43, W04429.

[76] Mitchell J. K., 1991: Conduction phenomena: from theory to geotechnical practice. Geotechnique, 43(3): 299-340.

[77] Moore J. K., Doney S. C. and Lindsay K., 2004: Upper ocean ecosystem dynamics and iron cycling in a global three-dimensional model. Global Biogeochem. Cycles, 18.

[78] Moreau F., Gibert D., Holshcneider M. and Saracco, G., 1997: Wavelet analysis of potential fields. Inverse Problems, 13, 165-178.

[79] Naudet V., Revil A., Rizzo E., Bottero J.-Y. and Bégassat P., 2004: Groundwater redox conditions and conductivity in a contaminant plume from geoelectrical investigations, Hydrology and Earth System Sciences, 8, 1, 8–22.

[80] Naudet V.and Revil A., 2005: A sandbox experiment to investigate bacteria-mediated redox processes on self-potential signals, Geophysical Research Letters, 32(11), L11405.

[81] Nisio S., Caramanna G. and Ciotoli G., 2007: Sinkholes in Italy: first results on the inventory and Analysis. Geological Society, London, Special Publications 279, 23-45.

[82] Nourbehecht B.,1963: Irreversible Thermodynamic Effects in Inhomogeneous Media and their Applications in Certain Geoelectric boblems, Ph.D. thesis, M.I.T.

[83] Onsager, L., 1931: Physical Review, 37, 405.

[84] Onuma, K., Muto J., Nagahama H. and Otsuki K., 2011, Electric potential changes associated with nucleation of stick-slip of simulated gouges: Tectonophysics, 502, 308-314.

[85] Orlando and Marchesi, 2001: Georadar as a tool to identify and characterise solid waste dump deposits. Journal of Applied Geophysics, 48, 163-174.

[86] Paige C.C. and Saunders M. A., 1982: LSQR: An algorithm for sparse linear equations and sparse least squares, ACM Trans. Math. Software, 8, 43-71.

[87] Paul M. K., 1965: Direct interpretation of self-potential anomalies caused by inclined sheets of infinite horizontal extensions. Geophysics, 30, 418-423.

[88] Patella D., 1997: Self-potential global tomography including topographic effects. Geophysical Prospecting, 45, 843-863.

[89] Peksen E., Yas T., Kayman A.Y. and Ozkan C., 2011: Application of particle swarm optimization on self-potential data. Journal of Applied Geophysics, 75, 305-318.

[90] Pellerin L., Holliger K., Slater L. and Yaramanci U., 2009: Methods and processes, foreword. Near Surface Geophysics. Special Issue on Hydrogeophysics, 7, 303-305.

[91] Perrier F., Petiau G., Clerc G. et al., 1997: A one-year systematic study of electrodes for long period measurements of the electric field in geophysical environments. Journal of Geomagnetism and Geoelectricity, 49, 1677-1696.

[92] Perrier F. and Raj Pant S., 2005: Noise reduction in long term self-potential monitoring with traveling 20 electrode referencing, Pure Appl. Geophys., 162, 165–179.

[93] Persson P. and Strang G., 2004: A simple mesh generator in MATLAB. Siam Rev 46(2), 329-345.

[94] Petiau G., 2000: Second generation of lead-lead chloride electrodes for geophysical applications. Pure and Applied Geophysics, 157, 357-382.

[95] Petiau G. and Dupis A, 1980: Noise, temperature coefficient and long-time stability of electrodes for telluric observations, Geophysical Prospecting, 28, 792-804.

[96] Petitta M., 2009: Hydrogeology of the middle valley of the Velino river and of the S. Vittorino plain (Rieti, Central Italy). Italian Journal of Engineering Geology and Environment 1, 157-181.

[97] Porsani J. L., Filho W. M., Elis V. R., Shbimeles F., Dourado J. C. and Mour, H. P., 2004: The use of GPR and VES in delineating a jcontamination plume in a landfill site: A case study in SE Brazil. Journal of Applied Geophysics, 55, 199-209.

[98] Reppert P.M., 2000: Electrokinetics in the Earth, Ph.D. thesis, Massachusetts Institute of Technology, Cambridge, Massachusetts.

[99] Revil A., 1999: Ionic diffusivity, electrical conductivity, membrane and thermoelectrical potentials in colloids and granular porous media: a unified model. Journal of Colloid and Interface Science, 212, 503-522.

[100] Revil A., Ehouarne L. and Thyreault E., 2001: Tomography of self-potential anomalies of electrochemical nature. Geophysical Research Letters, 28(23), 4363-4366.

[101] Revil A., Mendonca C.A., Atekwana E.A., Kulessa B., Hubbard S.S. and Bohlen K.J., 2010: Understanding biogeobatteries: Where geophysics meets microbiology. Journal of Geophysical Research, 115, G00G02.

[102] Revil A., Pezard P. A. and Glover P. W. J.: 1999. Streaming potential in porous media. 1. Theory of the zeta-potential. Journal of Geophysical Research, 104(B9), 20 021-20 031.

[103] Revil A. and Linde N., 2006: Chemico-electromechanical coupling in microporous media. Journal of Colloid and Interface Science, 302, 682-694.

[104] Revil A. and Jardani A., 2013: The Self-Potential Method: Theory and Applications in Environmental Geosciences, Cambridge University Press.

[105] Revil A. and Jardani A., 2010: Stochastic inversion of permeability and dispersivities from time lapse self-potential measurements: a controlled sandbox study. Geophysical Research Letters, 37.

[106] Reynolds J.M., 2011: An Introduction to applied and environmental geophysics. 2nd edition. John Wiley and Sons.

[107] Richards K., Revil A., Jardani A., Henderson F., Batzle M., and Haas A., 2010: Pattern of shallow ground water flow at Mount Princeton Hot Springs, Colorado, using geoelectrical methods: Journal of Volcanology and Geothermal Research, 198, 217-232.

[108] Rittgers J. B., Revil A., Karaoulis M., Mooney M. A., Slater L. D.and Atekwana E. A., 2013: Self-Potential Signals Generated by the Corrosion of Buried Metallic Objects with Application to Contaminant Plumes. Geophysics 78 (5), EN65-EN82.

[109] Rozycki A., Fonticiella J.M.R., Cuadra A., 2006: Detection and evaluation of horizontal fractures in Earth dams using self-potential method. Eng Geol 82(3, 145-153.

[110] Rubin Y. and Hubbard S.S., 2005: Hydrogeophysics, Springer, Netherlands, Water and Science Technology Library 50, 523.

[111] Sato M. and Mooney H. M., 1960: The electrochemical mechanism of sulfide self-potentials. Geophysics, 25, 226-249.

[112] Scales, J.and Snieder R., 1997: To Bayes or not to Bayes?, Geophysics, 62, 1045-1046.

[113] Shanahan P., Binley A., Whalley R. and Watts C., 2015: The use of electromagnetic induction (EMI) to monitor changes in soil moisture profiles beneath different wheat cultivars, Soil Sci. Soc. Am. J., 79, 459-466.

[114] Sharma P.V., 1997: Environmental and Engineering Geophysics. Cambridge University Press.

[115] Sheffer M.R., 2002: Response of the self potential method to changing conditions in embankment dams, M.Sc. Thesis, University of British Columbia, Dept. of Civil Eng.

[116] Sheffer M. R. and Oldenburg D. W., 2007: Three-dimensional modelling of streaming potential. Geophysical Journal International, 109(3), 839-848.

[117] Shi W., 1998: Advanced modeling and inversion techniques for three dimensional geoelectrical surveys, Ph.D. thesis, Mass. Inst. of Technol., Cambridge, Mass.

[118] Shtivelman V., 2003: Application of shallow seismic methods to engineering, environmental and groundwater investigations. Bollettino di Geofisica Teorica e Applicata, 44, 209-222.

[119] Sill W.R., 1983: Self-potential modeling of primary flows, Geophysics 48 , 76-86.

[120] Sivenas P. and Beales F.W, 1982: Natural geobatteries associated with sulphide ore deposits. I. Theoretical studies.Journal of Geochemical Exploration 17, 123-143.

[121] Soueid Ahmed A., Jardani A., Revil A. and Dupont J. P., 2013: SP2DINV: A 2D forward and inverse code for streaming potential problems. Computers and Geosciences, 59, 9-16.

[122] Soueid Ahmed A., Jardani A., Revil A. and Dupont J.P., 2014: Hydraulic conductivity field characterization from the joint inversion of hydraulic heads and self-potential data, Water Resour. Res., 50.

[123] Spinelli L., 1999: Analyse Spatiale de l'Activité Electrique Cérébrale: Nouveaux Développements, PhD Thesis (in French), Université Joseph Fourier-Grenoble I.

[124] Srivastava A, Ahamad J., Ray A.K., Kaur D., Bhattacharya A. amd Bhattacharya S., 2014: Analysis of U3 snoRNA and small subunit processome components in the parasitic protist Entamoeba histolytica. Mol Biochem Parasitol 193(2):82-92.

[125] Steeples, D.W., 2001: Engineering and environmental geophysics at the millenium, Geophysics, 66 (1), 31-35.

[126] Steeples D.W. and Miller R.D., 1990: Seismic-reflection methods applied to engineering, environmental, and ground-water problems, in Ward, S., ed., Geotechnical and Environmental Geophysics, V. 1, Review and Tutorial, Society of Exploration Geophysicists, Investigations in Geophysics 5, 1-30.

[127] Stern, O., 1924: Zur Theorie der elektrolytischen Doppelschicht (The theory of the electrolytic double shift). Zeitschrift Fur Elektrochemie Und Angewandte Physikalische Chemie, 30, 508-516.

[128] Stoll J., Bigalke J. and Grabner E. W., 1995: Electrochemical modeling of self-potential anomalies. Surveys in Geophysics, 16(1), 107-120

[129] Stumm W., 1992: Chemistry of the solid-water interface. New York: John Wiley and Sons, 428.

[130] Suski B., Revil A., Titov K., Konosavsky P., Voltz M., Dages C. and Huttel O., 2006: Monitoring of an infiltration experiment using the self-potential method, Water Resour. Res., 42, W08418.

[131] Suski, B., Rizzo E. and Revil A., 2004: A Sandbox Experiment of Self-Potential Signals Associated with a Pumping Test. Vadose Zone J. 3:1193–1199.

[132] Tezkan B., 1999: A review of environmental application of quasistationary electromagnetic techniques: Surv. in Geophys., 20, 279-308.

[133] Theis C.V., 1935: The relation between the lowering of the piezometric surface and the rate and duration of discharge of a well using ground-water storage. American Geophysical Union Transactions, 16, 519-524.

[134] Tikhonov A. N. and Arsenin V. Y., 1977: Solutions of Ill-Posed Problems. John Wiley and Sons, Washington.

[135] Titov K., Revil A., Konosavsky P., Straface S. and Troisi S., 2005: Numerical modelling of self potential signals associated with a pumping test experiment. Geophysical Journal International, 162, 641-650.

[136] Trolard F., Bourrie G., Abdelmoula M., Refait P. and Feder F., 2007: Fougerite, a new mineral of the pyroaurite-Iowaite group: Description and crystal structure. Clays and Clay Minerals 55, 324-335.

[137] Trujillo-Barreto N. J., Aubert-Vàsquez E. and Valdès-Sosa P.A., 2004: Bayesian model averaging in EEG-MEG imaging, NeuroImage, 21, 1300-1319.

[138] Vereecken H., Binley A.M., Cassiani G., Revil A., Titov K., 2006: Applied Hydrogeophysics. Applied Hydrogeophysics. Dordrecht : Springer 1-8.

[139] Vogelsang D., 2012: Environmental Geophysics – A practical guide. Springer Science and Business Media.

[140] Wahba G.,1990: Splines models for observational data (Society for Applied and Industrial Mathematics, Philadelphia.

[141] Weller A., Frangos W. and Seichter M., 1999: Three-dimensional inversion of induced polarization data from simulated waste. Journal of Applied Geophysics 41, 31-47.

[142] Wurmstich B., Morgan F. D., Merkler G.P.and Lytton R., 1991: Finite element modelling of streaming potential due to see page: study of a dam. Soc. Explor. Geophysicists Technical Program Expanded Abstracts, 10, 542-544.

[143] Yungul S.H., 1950): Interpretation of spontaneous polarization anomalies caused by spheroidal ore bodies. Geophysics 15, 237-246.

[144] Zhdanov M.S., 2002: Geophysical inverse theory and regularization problems in Methods in Geochemistry and Geophysics, The Netherlands, Amsterdam: Elsevier, vol. 36, 2002.

[145] Zonge K., Wynn J. and Urquhart S., 2005: Resistivity, Induced Polarization, and Complex Resistivity. Near Surface Geophysics, Society of Exploration Geophysics, Tulsa, OK, 265-300.